

LOW TEMPERATURE LATTICE INSTABILITY IN SINGLE  
AND POLYCRYSTALLINE  $ZrV_2$

by

MARK LEVINSON

S.B. Massachusetts Institute of Technology  
1972

Submitted in partial fulfillment of the requirements  
for the degree of  
DOCTOR OF SCIENCE  
at the  
Massachusetts Institute of Technology  
February, 1978

Signature of Author ..... **Signature redacted** .....  
Department of Materials Science and Engineering  
January 13, 1978  
Certified by ..... **Signature redacted** .....  
Thesis Supervisor  
Accepted by ..... **Signature redacted** .....  
Chairman, Departmental Committee on Graduate Students



## ABSTRACT

## LOW TEMPERATURE LATTICE INSTABILITY IN SINGLE

AND POLYCRYSTALLINE  $ZrV_2$ 

by

MARK LEVINSON

Submitted to the Department of Materials Science and Engineering on January 13, 1978 in partial fulfillment of the requirements for the degree of Doctor of Science.

A study has been made of the low temperature lattice instability and structural phase transformation in the cubic Laves phase (C-15 structure) superconductor,  $ZrV_2$ . A traveling heater solvent zone technique has been used with electron beam heating in high vacuum ( $10^{-7}$  torr) to obtain pure, homogeneous  $ZrV_2$ , including two single crystals. Four types of sample were examined to determine the relation between the lattice instability and microstructural perfection. These were, a single crystal, a single crystal containing several twin planes, polycrystalline material, and polycrystalline material containing approximately 1 vol. % Zr rich second phase inclusions. The behavior of this latter material was similar to that reported in the literature for  $ZrV_2$  produced by arc-melting.

Neutron diffraction was used to confirm the rhombohedral nature of the structural transformation, and it was found that the transformation temperature  $T_m$  decreased with increasing microstructural perfection, with no transformation occurring at all in the untwinned single crystal. The superconducting critical temperature  $T_c$  was observed to increase with increasing perfection, and microstructure was also found to affect the critical field,  $H_c$ . Resistivities were measured as a function of temperature, and showed anomalous increases near  $T_m$  for the transforming samples, and also showed generally similar behavior in the non-transforming single crystal. Hysteresis in the resistivities of the transforming samples clearly indicate that the transformation is first order.

It was concluded that a change in the electronic band structure most likely provides the driving force for the lattice instability, and that a structural transformation will take place in the presence of enough localized microscopic strain to overcome an apparent activation barrier.

Thesis Supervisor: Robert M. Rose

Title: Professor of Materials Science and Engineering

TABLE OF CONTENTS

	<u>Page</u>
ABSTRACT	2
TABLE OF CONTENTS	3
LIST OF FIGURES	5
LIST OF TABLES	8
ACKNOWLEDGEMENTS	9
I. INTRODUCTION	10
A. Background	10
B. Materials Preparation and Experimental Work	14
II. CRYSTAL GROWTH	16
A. Introduction	16
B. Traveling Heater Solvent Zone Technique	18
C. Procedures and Practical Difficulties	19
D. Apparatus	31
III. CHARACTERIZATION	36
A. Introduction	36
B. Crystal Structure Characterization	36
C. Microstructure	39
D. Spark Erosion Damage	45
E. Hardness	47

TABLE OF CONTENTS (Cont'd.)

	<u>Page</u>
IV. LATTICE TRANSFORMATION AND SOFT MODES	49
A. Introduction	49
B. Crystal Structures	50
C. Soft Mode Analysis	52
D. Experimental Apparatus and Procedures	53
E. Results and Data Analysis	57
V. LOW TEMPERATURE ELECTRICAL PROPERTIES	68
A. Introduction	68
B. Apparatus	69
C. Superconducting Properties	70
D. Resistivity	75
VI. DISCUSSION	85
A. Summary	85
B. Conclusions	86
C. Suggestions for Further Work	90
APPENDIX I - Phonon Symmetries	91
APPENDIX II - Lattice Strain Data Analysis	97
APPENDIX III - Structure Factors	104
APPENDIX IV - Ultrasonic Measurements	106
REFERENCES	112
BIOGRAPHICAL NOTE	

LIST OF FIGURES

<u>Figure</u>		<u>Page</u>
1	The Zr-V phase diagram. After Ref. 31.	17
2	A scanning electron micrograph of a V rich band caused by improper zone composition. Zone movement upwards. Mag. X85.	20
3	A polished and etched longitudinal cross-section showing, from left to right, Zr-rich solid, $ZrV_2$ and the solidified zone. Mag. X12.	22
4	A polished and etched longitudinal cross-section showing Zr rich inclusions and etch pits. Also visible are three horizontal twin boundaries. Zone movement was to the right. Mag. X470.	24
5	A scanning electron micrograph of a Zr rich inclusion in a polished and etched surface. Zone movement was upwards. Mag. X5,800.	25
6	A metallographic section showing the formation of Zr rich phase as the rate of zone movement (from right to left) was suddenly increased from 5mm/day to 12.5 mm/day. Mag. X250.	28
7	A metallographic section showing twins and grain boundaries, as well as some Zr rich inclusions. Mag. X155.	29
8	A polished and etched cross section of the twinned single crystal showing the band of twin planes. Mag. X21.	30
9	The electron beam floating zone apparatus.	32
10	A diagram of the electron gun power supply and feedback system.	35
11	A $ZrV_2$ single crystal with a portion of solidified zone remaining on the left. The long triangular reflection is from a (111) facet. Grid divisions = 1.27 mm.	37

LIST OF FIGURES (Cont'd.)

<u>Figure</u>		<u>Page</u>
12	A section of polycrystal with grain boundaries visible on the surface. Grid divisions = 1.27 mm.	38
13	A Laue back-reflection photograph taken on the longitudinal growth axis of the small single crystal.	40
14	A scanning electron micrograph of a Zr stringer in the same sample as in Fig. 5, but which has been etched with a different solution. Mag. X2000.	42
15	A scanning electron micrograph of a ZrV <sub>2</sub> fracture surface. Mag. X9,000.	43
16	A transmission electron micrograph of single phase ZrV <sub>2</sub> , showing no structure. Mag. X54,000.	44
17	A transmission electron micrograph of a spark-cut sample showing second phase particles and stacking faults. Mag. X60,000.	46
18	ZrV <sub>2</sub> atom positions in the C-15 structure.	51
19	Diagram of the neutron spectrometer and beam path.	55
20	The Ewald sphere construction for the neutron spectrometer.	56
21	(111) peak height vs. temperature for one grain of an inclusion filled polycrystal.	58
22	(111) peak height vs. temperature for the twinned single crystal. Also shown is the height of a (11.0) peak descended from the (220).	60
23	Double scattered intensity at the reciprocal space position (0,0,1.995) as a function of rotation around that vector.	64

LIST OF FIGURES (Cont'd.)

<u>Figure</u>		<u>Page</u>
24	Four point probe sample holder	71
25	Inductive $T_c$ curves for the twinned single crystal, a clean polycrystal, and an inclusion filled polycrystal.	72
26	Inductive $T_c$ measured before and after removal of endpieces from a clean polycrystal.	74
27	Resistive $H_c$ for the twinned single crystal, clean polycrystal, and inclusion-filled polycrystal.	76
28	Resistance vs. temperature for the twinned single crystal.	78
29	Resistance vs. temperature for a clean polycrystalline sample.	79
30	Resistance vs. temperature for an inclusion-filled polycrystalline sample.	80
31	A more detailed plot of the range $70^\circ$ to $140^\circ\text{K}$ based on the data in Figs. 28, 29, and 30.	81
32	Resistivity vs. temperature for the small, non-transforming single crystal.	82
33	Shifts in reciprocal lattice positions of the (220) and the (004) reflections occurring with a rhombohedral transformation in relation to the (hkh) reciprocal lattice plane	100
34	Velocity of sound vs. temperature for the twinned single crystal.	107
35	Velocity of sound vs. temperature for a clean polycrystal.	108
36	Velocity of sound vs. temperature for an inclusion-filled polycrystal.	109
37	Ultrasonic attenuation vs. temperature for the twinned single crystal.	111

LIST OF TABLES

<u>Table</u>		<u>Page</u>
1	Hardness values and penetration depths for different applied loads on clean polycrystalline material.	48
2	Characters for the Zr and V atom position transformations. The number preceding each operation indicates the number of those operations present.	94
3	Reciprocal space positions of reflections descended from the (004) and (220) as a function of lattice strains $\delta_a$ and $\delta_c$ .	98
4	Neutron intensity at points in the (hkk) reciprocal lattice plane surrounding (0,0,4). Temperature = 79°K.	101
5	Neutron intensity at points in the (hkk) reciprocal lattice plane surrounding (2,2,0). Temperature = 79°K.	102



ACKNOWLEDGEMENTS

The author is indebted to his advisors Professors Robert M. Rose and Judith L. Bostock for their very generous help and encouragement. It has been a privilege to learn by their example of intellectual and professional integrity. He is also grateful to Mr. Irvin M. Puffer for his very valuable and able technical assistance and instruction, as well as for his friendship.

Many thanks are also due to Professor Margaret L.A. MacVicar for her assistance and advice, to Dr. Gen Shirane for his very generous help with the neutron diffraction work, and to Professor John Vander Sande for his assistance with the transmission microscopy. Thanks also to Professors A.F. Witt and Frank Cocks, and Dr. David Moncton for their helpful discussions and suggestions, and to Mr. John Mara for his excellent drawings and figures.

This work was supported by the National Science Foundation.

## I. INTRODUCTION

### A. Background

A good deal of effort in the field of superconductivity research has, in recent years, focused on understanding the behavior of materials which retain their superconducting properties at relatively high temperatures and magnetic fields. This work has been motivated both by a desire for basic knowledge, and for possible technological applications. Notable among these materials are the A-15 structure intermetallic compounds which, as a group, exhibit the highest known values of critical temperature  $T_c$  and critical field  $H_c$ . One interesting feature of these is that several have been observed to undergo structural phase transformations and exhibit anomalous transport properties near the transformation temperature. Two in particular,  $V_3Si$  and  $Nb_3Sn$ , have exhibited cubic to tetragonal transitions upon cooling through 21°K and 45°K respectively<sup>1,2</sup>.

Another group of superconducting intermetallics with relatively high critical temperatures and fields are those with the C-15 or cubic Laves phase structure, in particular  $ZrV_2$  and  $HfV_2$ <sup>4,5,6</sup>. These compounds, like the A-15's, appear to undergo lattice transformations and exhibit anomalies in lattice dependent properties. For  $ZrV_2$  in particular, anomalies have been observed in the neighborhood of 120°K in the electrical resistivity<sup>7</sup>, specific heat<sup>8</sup>, magnetic susceptibility<sup>9</sup>, internal friction<sup>9</sup>, and velocity of sound<sup>11</sup>. Several investigators were unable to detect any lattice transformation in  $ZrV_2$  with X-rays, but Moncton<sup>12</sup>, using neutron diffraction, found a cubic to rhombohedral

transition at 117°K.

These phenomena would be expected to involve changes in the materials' phonon spectra, and, since the advent of the BCS theory of superconductivity, it has been recognized that these materials must have a strong electron-phonon interaction. Therefore, the theoretical work with the A-15's has concentrated on changes in the electronic configuration as a basis for the transformation, and some success has been achieved in accounting for the observed properties.<sup>3</sup>

Although these Laves phase compounds show behavior which is strikingly similar to that of the A-15's, the microscopic theories proposed to explain this behavior in the latter materials cannot be extended to include the C-15's. These theories rely on the existence of a singularity in the electron density of states which is peculiar to the A-15 structure and which simply does not exist in that of the C-15's. Therefore, by studying the structural phase transformation and associated phenomena in the C-15 compounds, some insight may be gained into a more general mechanism which may be at work here, and indeed may involve an inherent property of high  $T_c$  superconductors.

Phase changes in general constitute one of the more intriguing aspects of the physics of solids. Although these phenomena are adequately described by thermodynamic and sometimes kinetic approaches, they are still not well understood from a microscopic, or first principles point of view. However, displacive or structural phase transformations seem to be more susceptible than others to studies which may

lead to an understanding of the microscopic mechanisms at work. This is because, in principle at least, these transformations may be characterized by some order parameter which is zero at and above the transition temperature, and grows continuously below that temperature. An example of this parameter would be the spontaneous electric field appearing at a ferroelectric transition. One would hope that the study and characterization of the order parameter in a given transformation would lead to an understanding of the microscopic mechanisms involved. It may be noted that some transformations may exhibit more than one order parameter, such as the distortion of the crystal lattice which may accompany a ferroelectric transition. It is important in this situation to determine the primary order parameter; that is, the one which is the direct manifestation of the microscopic mechanism.

There have been, in general, two approaches to the study of these transformations. First are the microscopic descriptions, which are fairly straightforward in the case of ferroelectric or ferromagnetic ordering. Second are the thermodynamic and kinetic approaches which are generally based on Landau's expansion of the free energy as a function of the order parameter in a power series about the transition temperature<sup>13</sup>, or on solid state kinetics.<sup>14</sup>

In recent years a third approach has been explored which may in some cases serve as a sort of bridge between the two others. This is the idea of soft phonon modes. The various lattice vibrations of a solid may be described in terms of discrete phonon modes which have well

defined frequencies, wavelengths, and crystallographic polarizations and directions. They also require definite atomic displacements which may be analyzed in terms of strain energy contributions to the free energy of the system. Therefore, the study of any anomalous behavior of phonon modes in the vicinity of a displacive transformation will give information as to vibrational and strain energies, interatomic forces, and the symmetry and crystallographic features of the mechanism responsible for the transition.

This anomalous behavior has been observed in many systems,<sup>15</sup> and generally takes the form of a particular mode whose frequency decreases, and therefore its displacement amplitude increases, as the transition temperature  $T_m$  is approached. This can be thought of as due to a softening of the interatomic force constants in the appropriate direction, hence the name soft modes. At and below  $T_m$  the atomic displacements become static, resulting in the transformed crystal structure. The phonon is said to have condensed into the lattice.

The detection of a particular soft-phonon mode in a given system will not only provide the kinds of information noted above, but will also indicate directions for further theoretical and experimental work.

One problem that has clouded the issue as far as  $ZrV_2$  is concerned, is that often different investigators have reported different results for the same properties, and even found differing results for the same samples at different times. These disparities are in all probability due to the fact that invariably the materials were prepared by

arc-melting powders. Experience with this type of process indicates that, especially with Zr, these samples most likely contained oxide or carbide contaminants, as well as segregated second or third phase regions. Furthermore, it is probable that the  $ZrV_2$  itself contained numerous crystal structure defects, and local residual stresses. Because the displacive transition may be very sensitive to local stresses and crystal defects, it is apparent that any definitive investigation will require material where the extent of these factors is known.

Therefore, the aims of this work were fivefold: first, to produce clean, homogeneous  $ZrV_2$ , and especially single crystals which are vitally important for a variety of interesting experiments involving lattice dynamics and electronic band structure. Second, to characterize the material as completely as possible with regard to microstructure and defect structure. Third, to make a preliminary study of the lattice instability by measuring electronic properties and crystal structure as a function of temperature. Fourth, to look for evidence of a soft phonon mechanism by searching for the remnants of such a phonon in the low temperature phase in the form of a sublattice distortion. And fifth, to try and find some correlation between the lattice instability and superconducting properties.

#### B. Materials Preparation and Experimental Work

In light of the motivations stated above, this work has progressed as follows: First, a method was devised to grow clean, homogeneous  $ZrV_2$

including single crystals. This consisted of the adaptation of a traveling solvent zone technique for use with a high vacuum electron beam floating zone apparatus. Further modifications were required to overcome various difficulties which are described in Chapter II. A large amount of homogeneous, large grain polycrystalline  $ZrV_2$  was obtained as well as two single crystals. Also, in the course of perfecting the growth process, a large amount of non-homogeneous  $ZrV_2$  containing approximately 1 vol. % Zr rich second phase inclusions was obtained. This material proved useful in that its properties differ markedly from those of the clean material, but are similar to those reported in the literature for arc-cast material.

Secondly, the materials were intensively investigated as to their microstructure and defect structure. The lattice transformation and electrical properties could then be correlated with these results. Also, an examination of microhardness and fracture surface appearance was made to give some idea of the mechanical properties.

Third, crystal structure was determined as a function of temperature and a search was made for a sublattice distortion as evidence of the role of a soft phonon mechanism in the lattice transformation. The search was based on a group theoretical analysis of the modes consistent with the observed lattice distortion.

And finally, superconducting parameters and resistivity as a function of temperature were examined. In addition, ultrasonic measurements were made on several samples by Mr. Ralph Bergh. This work is described in Appendix IV.

## II. CRYSTAL GROWTH

### A. Introduction

To our knowledge, there had been no previous attempt to grow  $ZrV_2$  crystals, and in fact no methods other than arc-melting had been used to prepare this material. Therefore, it was necessary to choose a crystal growth method which offered the greatest chance of success in light of several obvious difficulties. It was felt that growth from the melt is perhaps the easiest way to obtain large metal or alloy crystals, but to use such a method for  $ZrV_2$ , two problems must be resolved at the outset. First, Zr is a pyrophoric element which reacts easily to form very stable oxides, carbides, etc. Therefore measures would have to be taken to avoid contamination of the melt during the growth process. Second, as shown in the Zr-V phase diagram (Fig. 1),  $ZrV_2$  forms peritectically so that simple solidification from the melt will not produce single phase material, except possibly with the addition of prohibitively long anneals.

Both these problems may be avoided by the use of a solvent zone technique, to produce single phase material, in a high vacuum electron beam floating zone apparatus, which requires no crucible and therefore eliminates the largest possible source of contamination. There were also a number of practical difficulties encountered, and their solution, described in Section C, led to the modification and construction of the apparatus described in Section D.



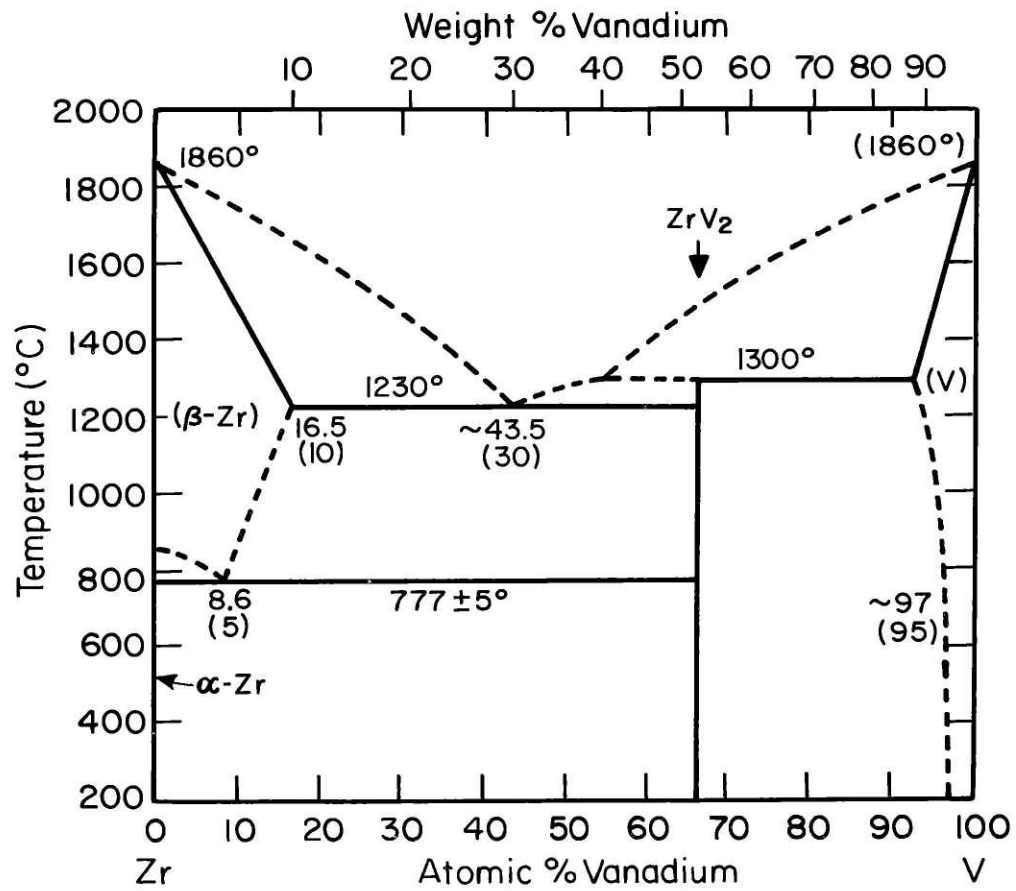


Figure 1 - The Zr-V phase diagram. After Ref. 31.

### B. Traveling Heater Solvent Zone Technique

There are two variations on the solvent zone technique which may be used without a crucible. One, first described by Pfann<sup>16</sup> is called the Temperature Gradient Zone Melting or Traveling Solvent Method, and has been used to grow several semiconductor compounds, including GaAs and SiC<sup>17,18,19</sup>. This technique uses a temperature gradient across the zone to cause diffusion of material from the hotter to the cooler liquid-solid interface, because of different solubilities at the two temperatures. The liquid thus moves toward the hotter end, solidifying the desired material behind.

This technique was explored using the floating zone apparatus, but it became apparent that the very narrow range of allowable temperatures (between 1230° and 1300°C) made it difficult to achieve a large gradient along a suitably long section of crystal. Therefore, further work was done using a Traveling Heater Solvent Zone Method,<sup>17</sup> which has been used to grow GaP and ZnO among others. This technique relies on the mechanical motion of a heater to move the zone rather than a temperature gradient.

The success of this method rests upon finding a set of conditions whereby both a Zr-V liquid and solid  $ZrV_2$  are in thermodynamic equilibrium. Reference to the Zr-V phase diagram (Fig. 1) shows that this is possible where the liquid has a composition and temperature lying on that portion of the liquidus between the eutectic and peritectic points. A molten zone of this type, when moved into a Zr-V feed mixture, will form single

phase  $ZrV_2$  at its trailing end. If the feed mixture is of the exact  $ZrV_2$  composition, then a mass balance is achieved because the same composition material is being both dissolved from the feed material and solidified in the crystal. The major constraint is that the zone move slowly enough to dissolve the elemental Zr and V in the feed material and to permit the excess V to diffuse across the zone.

### C. Procedures and Practical Difficulties

To avoid oxide contamination associated with powders, feed material was prepared by inserting Zr rod (99.2% purity) into V tube (99.5% purity) and swaging to form a composite rod 3.6mm in diameter. Because of the different rates of work hardening of the two components, it was difficult to predict exactly what the initial rod and tube dimensions should be to result in a composite of the correct 66.7 at. % V composition. In addition, because of the very narrow range of allowable zone composition (between 43.5 at.% and about 53 at.% V), if the composite rod were even slightly off stoichiometry, the zone would gain more of one component than it lost to the  $ZrV_2$  solid, and before too long the liquid composition would exceed the above limits. The excess constituent would then precipitate out. Thus relieved of the excess, the liquid composition would revert to the nominal range and the formation of single phase  $ZrV_2$  would continue. This process resulted in periodic bands of Zr or V rich second phase in a  $ZrV_2$  matrix, separated by regions of pure  $ZrV_2$ . A typical V rich band is shown in Fig. 2. The distance between these bands was governed by the degree of deviation from stoichiometry in the

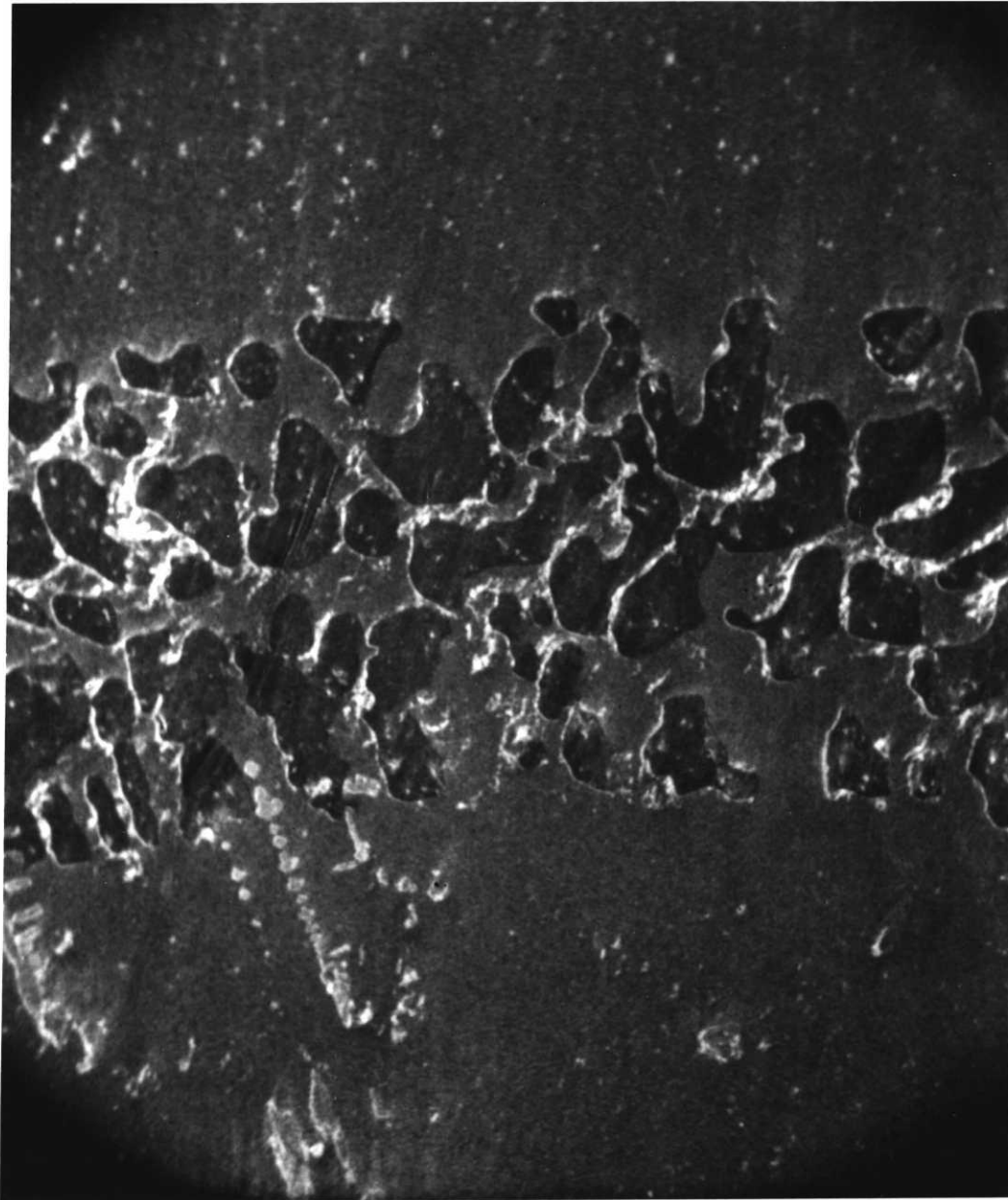


Figure 2 - A scanning electron micrograph of a V rich band caused by improper zone composition. Zone movement upwards. Mag.X85.

composite. Therefore, to obtain a good composite, a good deal of trial and error was required. Ten different composites were tried before an average distance of 3 cm. between bands was achieved. Metallographic examination of a cross-section of this composite revealed an overall composition of 66.2 at.% V.

The correct zone composition was produced at the start of the growth process by placing a section of composite in the crystal growth apparatus end to end with an equal diameter piece of Zr rod. The electron gun was initially positioned at the intersection of the two rods so that a molten zone would be formed from the ends of both. In this way, the initial zone was enriched in Zr before being moved into the composite feed rod. If it was too rich in Zr, the first solid to form from the moving zone would be Zr rich phase, so that the zone would lose more Zr than it gained from the feed material until its composition passed the eutectic point and stabilized in the correct region. Similarly, if the zone was too V rich, V solid would form until the desired composition was achieved in the liquid, and henceforth  $ZrV_2$  would be produced.

This sequence of events is shown in Fig. 3. The zone started at the Zr rod visible at the far left, and initially produced a region of Zr rich solid, followed by the first fine-grained  $ZrV_2$ . Subsequent growth produced progressively larger grain material, until growth was stopped, leaving the solidified zone at the right.

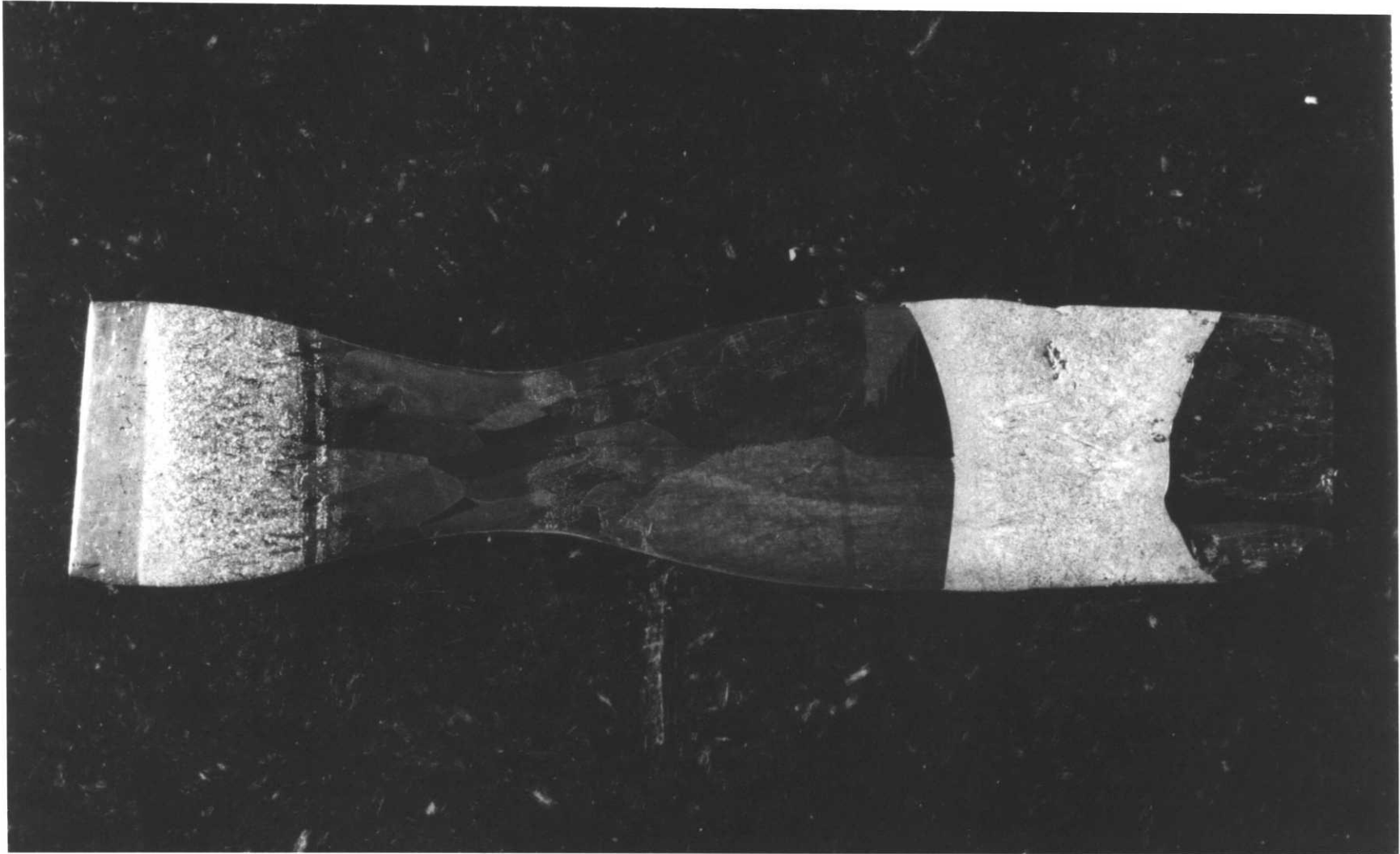


Figure 3 - A polished and etched longitudinal cross-section showing, from left to right, Zr-rich solid,  $ZrV_2$ , and the solidified zone. Mag. X12.

It was found that the rate of zone movement must be 2 mm/hr or less to allow the liquid to dissolve the elemental Zr and V in the feed rod. However, material grown at this speed exhibited dendritic inclusions of Zr rich phase within the  $ZrV_2$ . (They were so identified by etching characteristics and SEM X-ray analysis). Typical inclusions are shown in a metallographic section shown in Fig. 4, where the direction of zone movement was to the right, and in the scanning electron micrograph in Fig. 5. Surrounding the inclusions are etch pits which are discussed in Chapter III.

An attempt was made to determine if these inclusions were the result of a non-equilibrium effect and could be removed by annealing. Several samples were annealed in a ZrO crucible in a vacuum furnace at  $10^{-5}$  torr and temperatures ranging from 1200°C to 1280°C. This process was found to have no effect on the inclusions.

It was therefore apparent that the Zr inclusions were the result of some instability at the growth interface similar to the kind caused by constitutional supercooling, although the interface breakdown seen in normal constitutional supercooling did not occur here. Constitutional supercooling can be avoided by either decreasing the growth rate, increasing the temperature gradient at the liquid-solid interface, or increasing the rate of diffusion of Zr in the liquid away from the interface. The last alternative was not considered feasible, so efforts were concentrated on the first two.

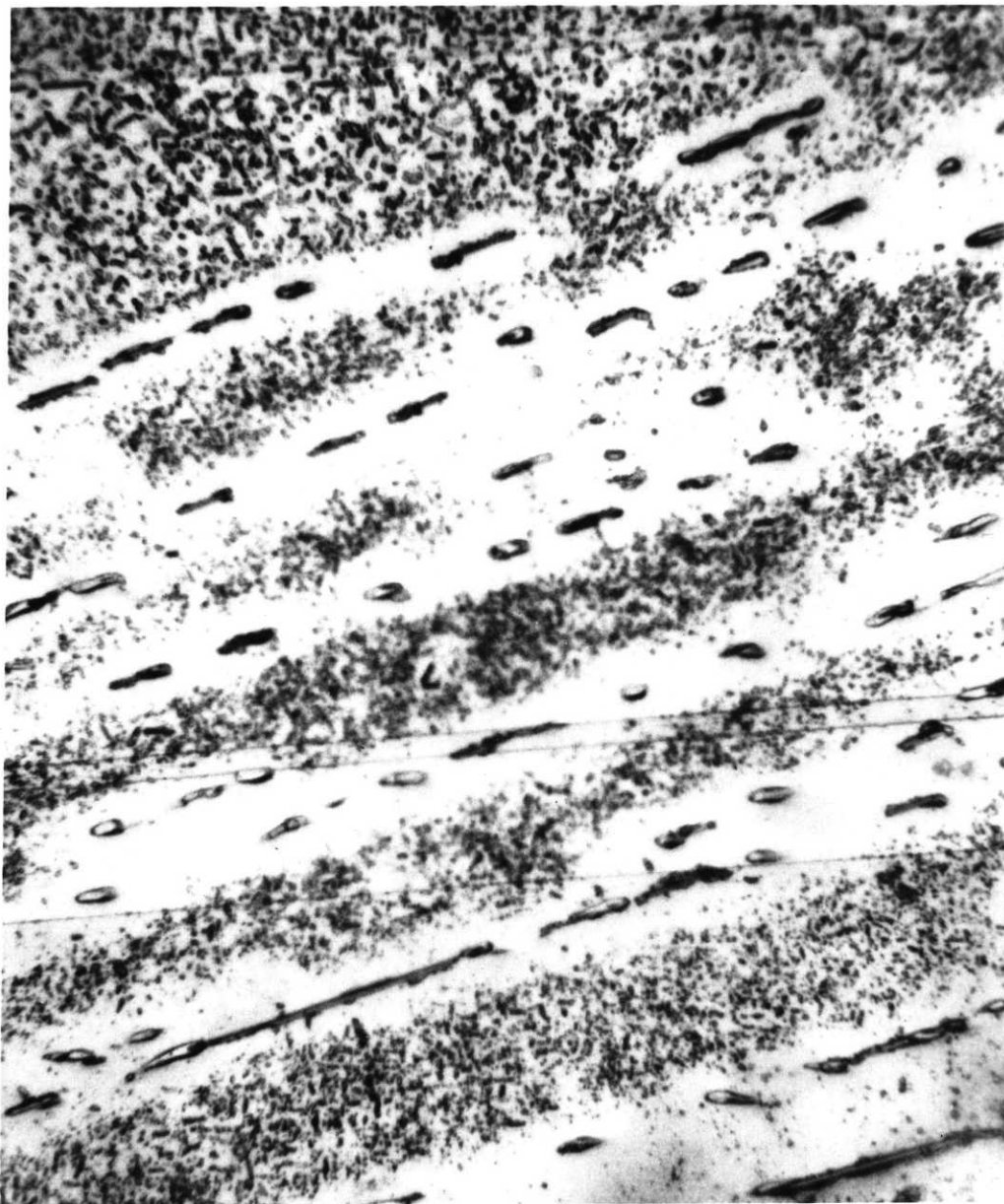


Figure 4 - A polished and etched longitudinal cross-section showing Zr rich inclusions and etch pits. Also visible are three horizontal twin boundaries. Zone movement was to the right. Mag. X470.



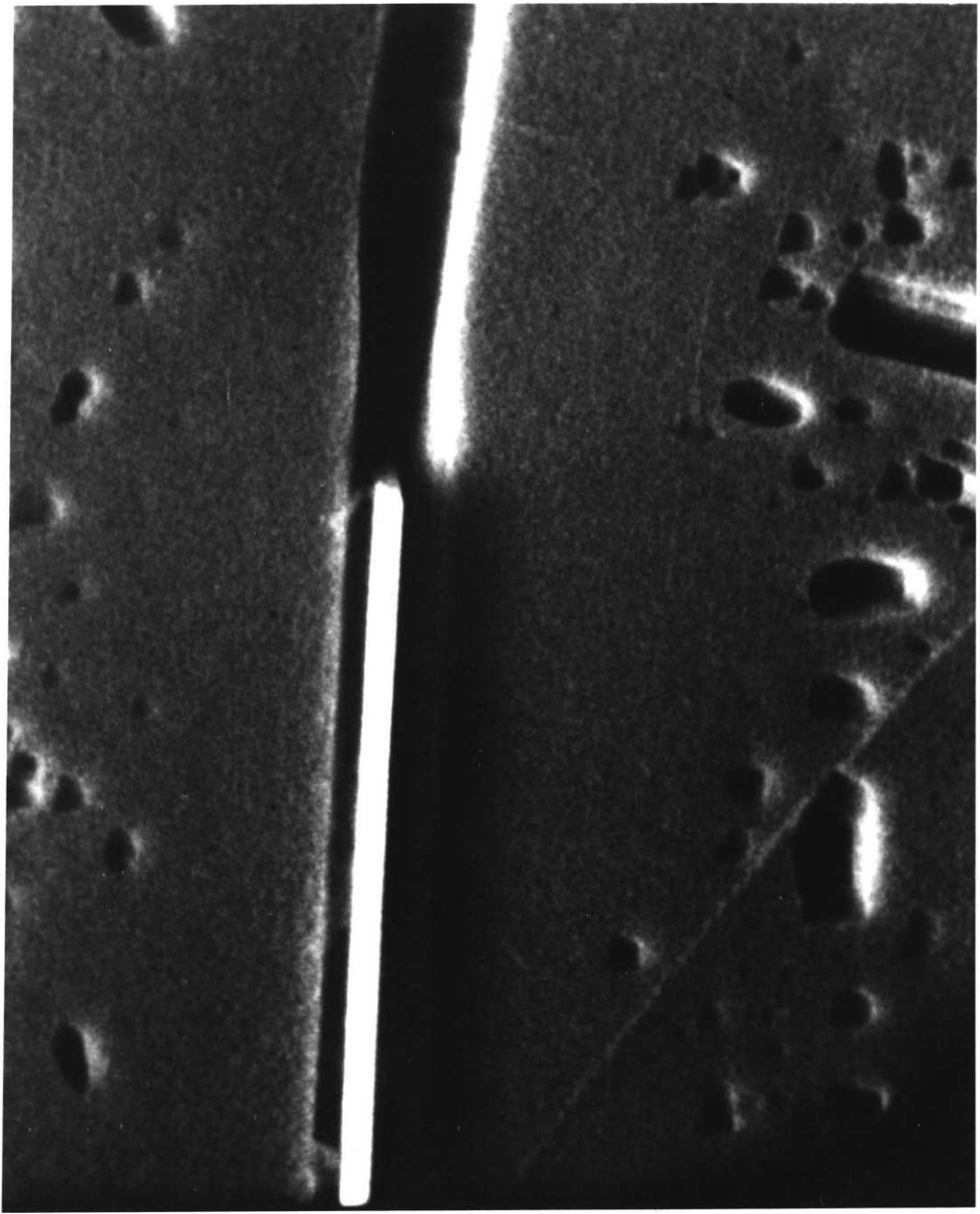


Figure 5 - A scanning electron micrograph of a Zr rich inclusion in a polished and etched surface. Zone movement was upwards.

Mag. X5,800.

The slowest speed available with the crystal growth apparatus was 0.5 mm/hr. Material grown at that rate had fewer inclusions, but they were not eliminated. An attempt was made to increase the temperature gradient at the growth interface by increasing the accelerating potential between the filament and crystal, thus narrowing the focus of the electron beam. But at voltages in excess of 1.1 kV., the effect was to produce heating of the exterior of the zone at the expense of the interior, resulting in a zone of butterfly shaped longitudinal cross-section. In any case, the constitutional supercooling inclusions were not substantially reduced by this procedure.

Thus it was apparent that an apparatus was needed which included provisions for very slow growth rates and for cooling the ends of the sample rod to increase the temperature gradient. In addition it was realized that the apparatus must be very stable with respect to power input to the zone, and to zone movement. Fluctuations of either of these parameters would result in variations of the microscopic rate of growth-front advance, yielding momentary rates greater than that of the zone as a whole. Therefore, the crystal growth equipment was modified and a new power supply constructed to overcome these problems. The apparatus is described in Section D.

It was found that constitutional supercooling was eliminated at growth rates of 5mm/day or less with the temperature gradient achieved in this equipment of about 300°C/cm. This dependence on growth rate is demonstrated in Fig. 6 where the speed of the zone, moving right to left,

was suddenly increased from 5mm/day to 12.5 mm/day. The especially large amount of Zr rich phase produced on the left is presumably due to an overall zone composition quite close to the eutectic point. In fact, sometimes regions of samples grown at the slower rate exhibited super-cooling inclusions when the zone strayed too close to the Zr rich limit. Therefore, all samples were examined metallographically, and any such regions were cut away from the clean material.

There were two additional problems which bear mentioning. First, because no seed crystals existed, it was necessary to wait for one grain of the polycrystalline material formed initially to grow at the expense of the others and finally encompass the entire cross-section of the rod, thereafter growing as a single crystal. Although the grains did tend to coarsen, as shown in Fig. 3, in the usual run of 2-3 cm. in length, no one grain dominated. Thus in the last 12 growth runs only two single crystals were obtained. This problem could of course be avoided by the use of a seed crystal.

Second, the material demonstrated a proclivity for twin formation. These can be seen in Fig. 7, and were also found in the larger of the two single crystals obtained, as discussed in Chapter III and shown in Fig. 8. Again, this problem could most likely be eliminated by the use of a good seed crystal.

To use a seeded growth method one would need to have a zone of the correct composition at the start of the run. This condition could be arranged by cutting the crystal away from the zone remaining at the end

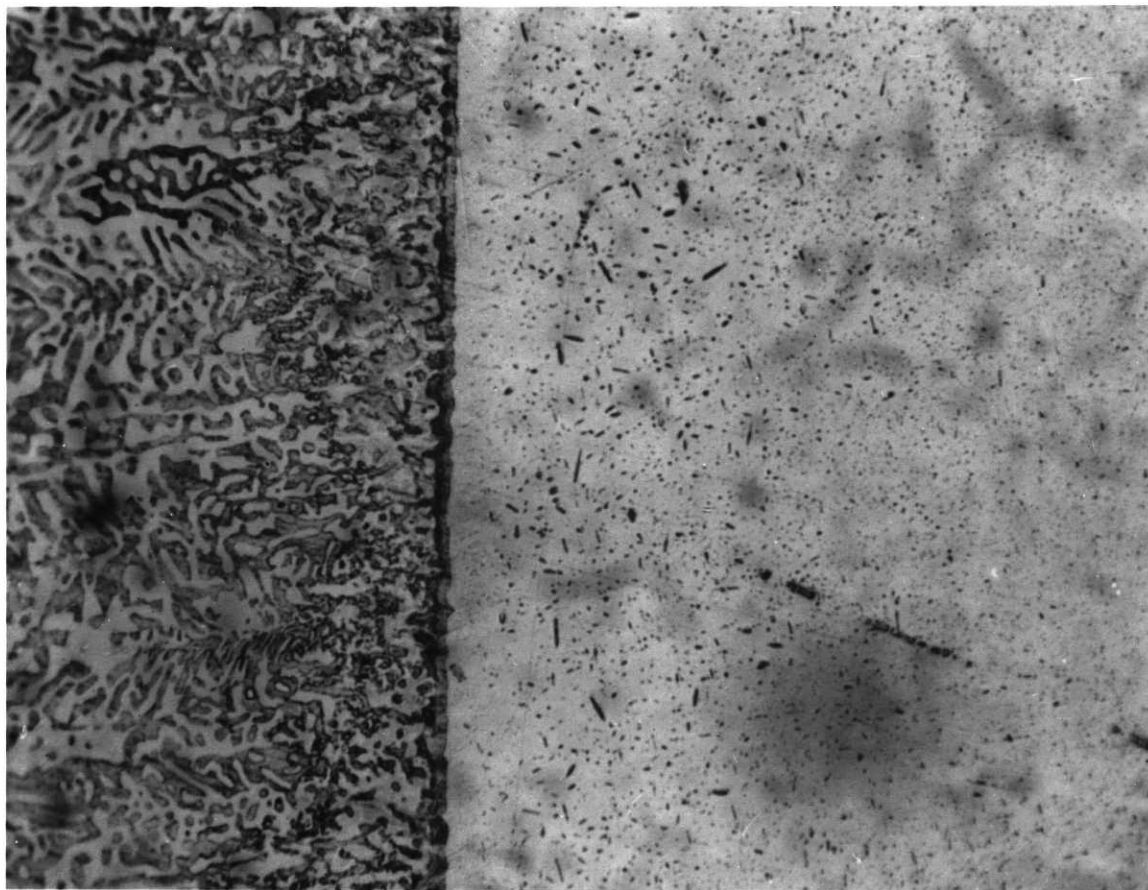


Figure 6 - A metallographic section showing the formation of Zr rich phase as the rate of zone movement (from right to left) was suddenly increased from 5mm/day to 12.5 mm/day. Mag. X250.

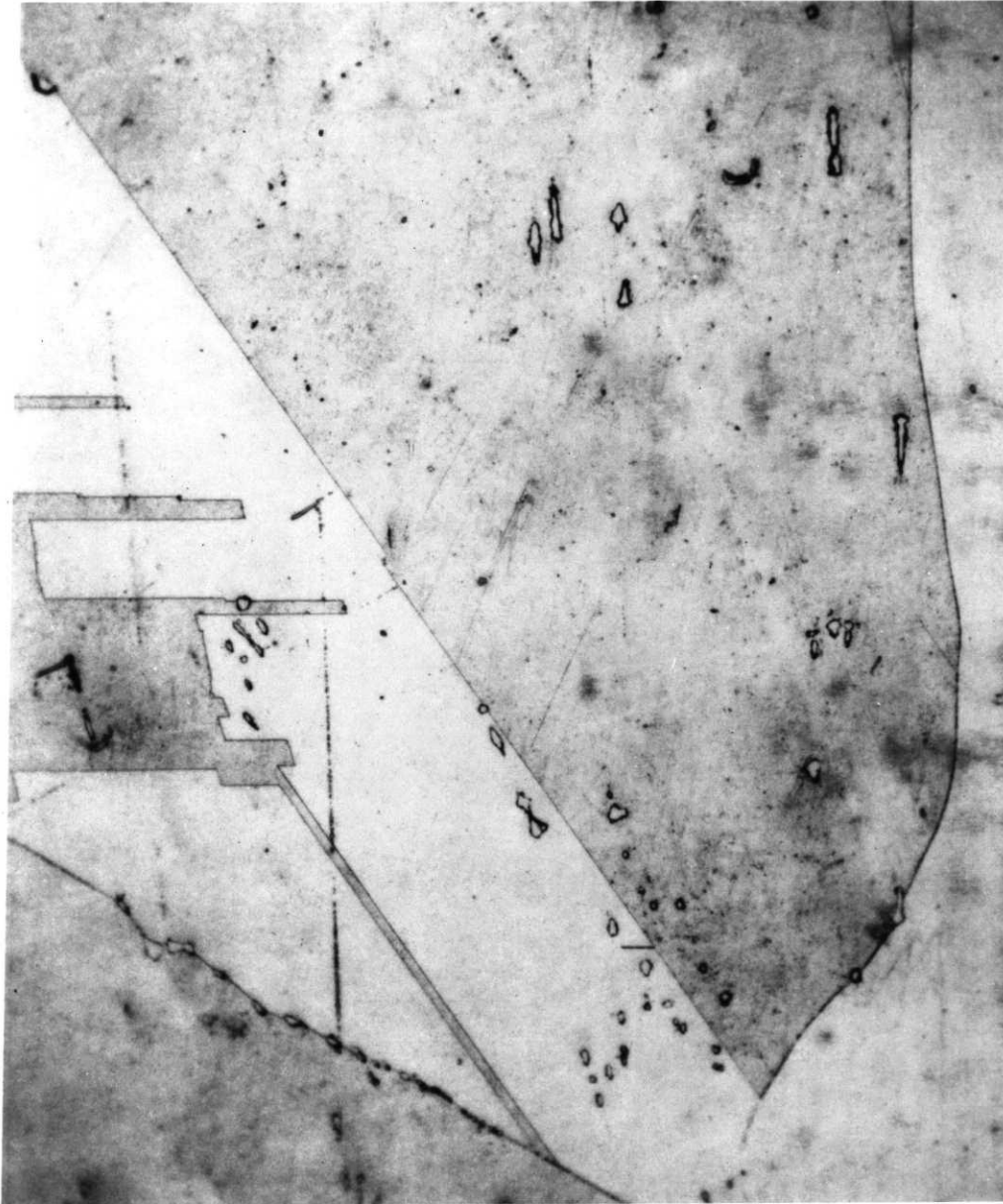


Figure 7 - A metallographic section showing twins and grain boundaries, as well as some Zr rich inclusions. Mag. X155.

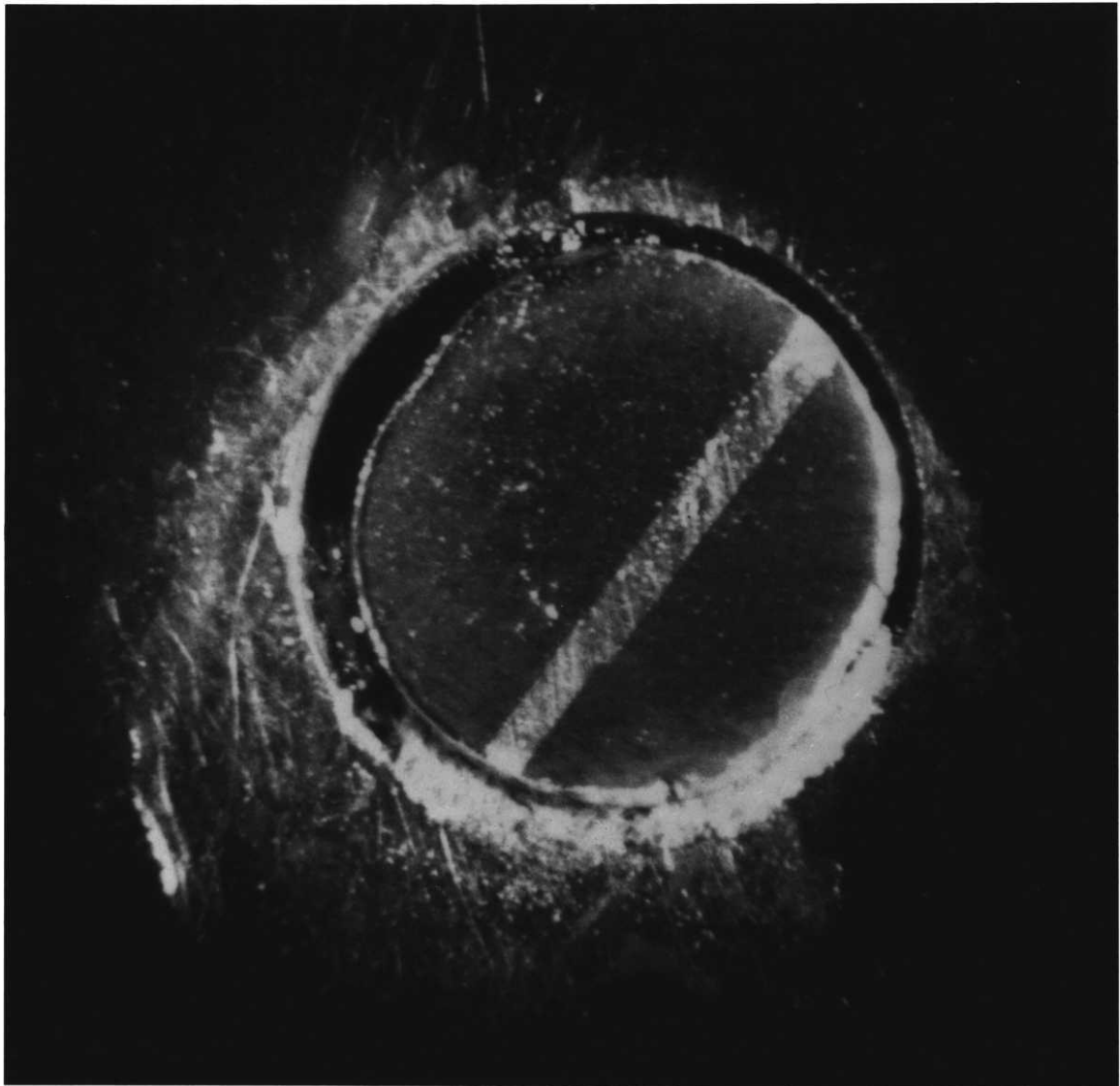


Figure 8 - A polished and etched cross-section of the twinned single crystal showing the band of twin planes. Mag. X21.

of the previous run and, leaving that zone attached to the remainder of the composite, positioning it opposite the seed in the crystal grower. The only problem would be to fix the seed in a holder which would insure the maximum thermal conductivity away from the crystal. This procedure would allow the growth of crystals with the same orientation as that of the seed. However, producing crystals with differing orientations would be more difficult because it would require that the zone remain stable while wetting the oriented face of the seed crystal.

#### D. Apparatus

The major modifications to the crystal growth apparatus consisted of a new drive system, designed to provide very slow and steady zone motion, and the addition of a water cooled specimen holder. The presence of water lines required that the specimen be at ground potential, which necessitated the construction of a power supply system capable of operating the electron gun filament at a negative potential with respect to the ground.

The apparatus is diagrammed in Fig. 9. The tungsten electron gun filament surrounds the specimen rod, and the thermally emitted electrons are accelerated onto the rod by a positive potential of 1 kV. The metal plates above and below the filament serve to focus the electron beam to form a short molten zone in the specimen rod. The ends of the rod are held by weighted levers in the solid copper endpieces of the crystal holder. The contact points are coated with silver paint to insure the maximum heat conduction from the rod. The endpieces are cooled by water introduced from outside the vacuum system by means of a feedthrough connection and flexible stainless steel tubes.

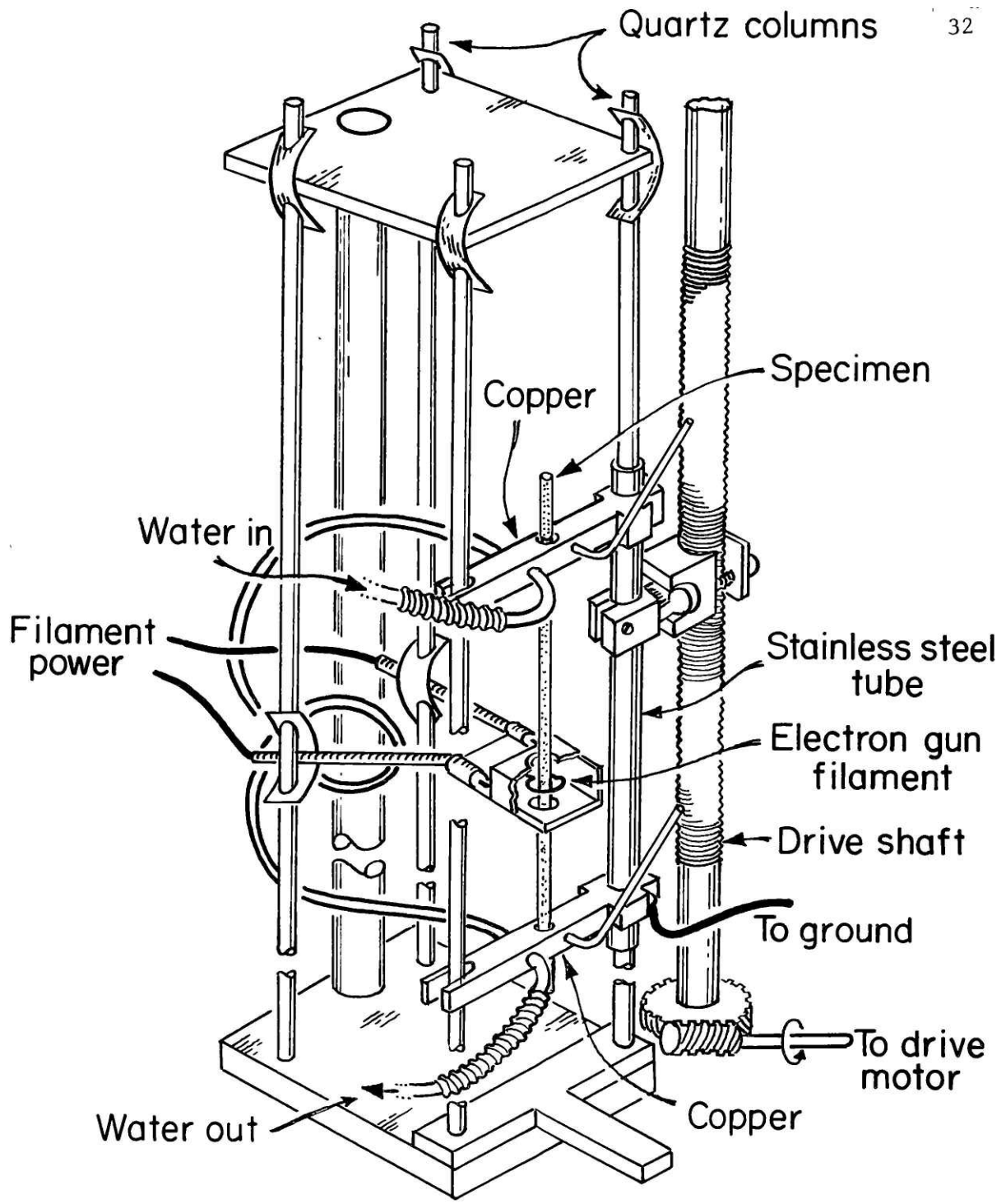


Figure 9 - The electron beam floating zone apparatus.



The water cooling produced a temperature gradient estimated to be in excess of  $300^{\circ}\text{C}/\text{cm}$ . at the liquid-solid interface. This value was inferred by optical pyrometry of the specimen rod below the zone. An accurate measurement of the gradient would be extremely difficult because the liquid cannot be contacted with any sensing device, and temperature measurement techniques using radiation (such as pyrometry) would be upset by the radiation from the filament as well as by the glass in the vacuum system bell jar.

The crystal holder moves along two quartz rods and is supported by its attachment to the drive shaft. This attachment consists of a threaded half-cylinder held against the threads of the drive shaft by a pressure plate. This arrangement insures a smooth backlash-free motion of the holder. The drive shaft is in turn driven by a synchronous electric motor located outside the vacuum system. A gearing mechanism on the motor allows a range of speeds at the crystal holder of from  $0.4\text{ mm/day}$  to  $25\text{ mm/day}$ . The normal speeds used were  $5\text{ mm/day}$  and  $2.5\text{ mm/day}$ . Faster motion resulted in constitutional supercooling, and at slower speeds too much time was required.

A mechanism is incorporated into the base of the apparatus allowing a small amount of lateral movement of the quartz rods on which the specimen holder travels. This allows a fine adjustment of the position of the specimen rod and zone within the electron gun filament. This adjustment may be made from outside the vacuum system during a growth run by means of a lever. It is important to maintain the position of the specimen rod

centered within the filament to give even heating and a uniform zone. Otherwise, with two non-parallel liquid-solid interfaces, it is apparently difficult for one grain to outgrow the others, and a rather fine grained material is the result.

The apparatus is situated in an ion-pumped vacuum system, which uses titanium pumping elements, thus avoiding the possibility of hydrocarbon contamination of the material by diffusion pump oil. The initial pressure of less than  $10^{-7}$  torr rose to about  $10^{-6}$  torr as the power was first applied, but decreased within a few hours to about  $10^{-7}$  torr where it remained for the balance of the run.

The power supply is diagrammed in Fig. 10. It consists of a well regulated high voltage DC supply ( $\pm .01\%/hr$ ) and an AC filament supply which is capable of holding the emission current to within about 1% of the set value. A constant voltage and emission current results in a constant power input to the molten zone.

Control of the filament supply is achieved by a feedback voltage from the emission circuit between the filament and specimen. This voltage is compared with a reference which is generated by a set of mercury batteries and set to the desired level with a ten-turn potentiometer. The resulting signal is fed to a unijunction transistor which controls the firing point of an SCR in the filament supply circuit. The buffer amplifier and transformer are necessary to allow the filament to be operated at a negative potential with respect to ground.

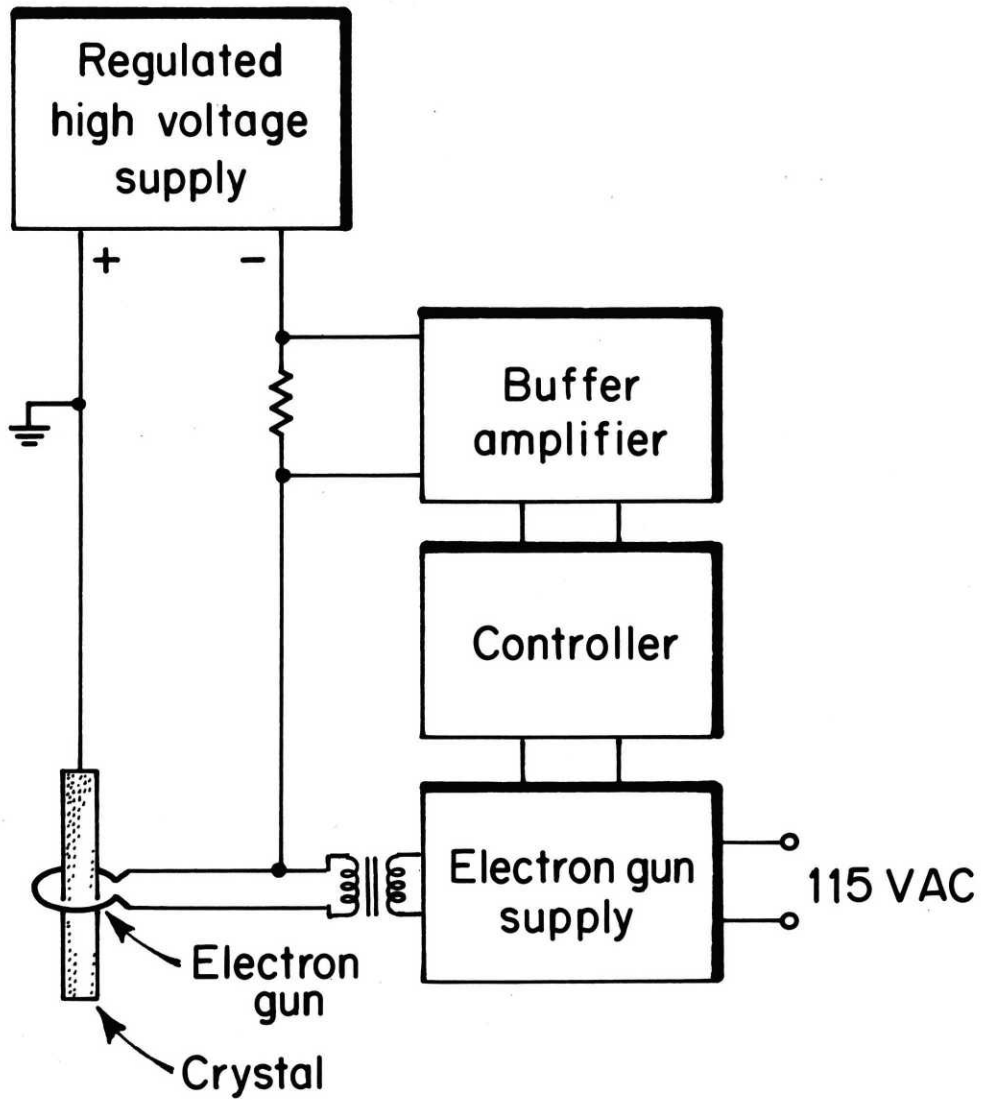


Figure 10 - A diagram of the electron gun power supply and feedback system.

### III. CHARACTERIZATION

#### A. Introduction

The material obtained from the crystal growth process was characterized as to its crystal structure and microstructure. This material included two single crystals, one 2 mm long and 3.6 mm in diameter, and a larger one 6 mm long and the same diameter. The latter is shown in Fig. 11. At the left end is a portion of the zone remaining when growth was halted and which was removed before any measurements were made. The long triangular reflection is due to a (111) facet plane. This crystal also contains a band of five parallel twin planes which are parallel to the facet. The band is visible in the polished and etched cross-section shown in Fig. 8. Neutron diffraction measurements confirmed that these are (111) planes and that the bulk of the material on either side of the band has an orientation which is twinned relative to the other.

In addition to the single crystals, a large amount of polycrystalline material was obtained. This included both homogeneous material and Zr inclusion filled material ( $\sim 1$  vol.%) which was produced before the effects of constitutional supercooling were eliminated. This latter material proved useful for study in that its properties differed significantly from those of the clean material. A typical polycrystal piece is shown in Fig. 12. Grain boundaries are visible on the as-grown surface.

#### B. Crystal Structure Characterization

A portion of single phase  $ZrV_2$  was crushed under an Ar atmosphere and examined at room temperature in an X-ray diffractometer. The resulting

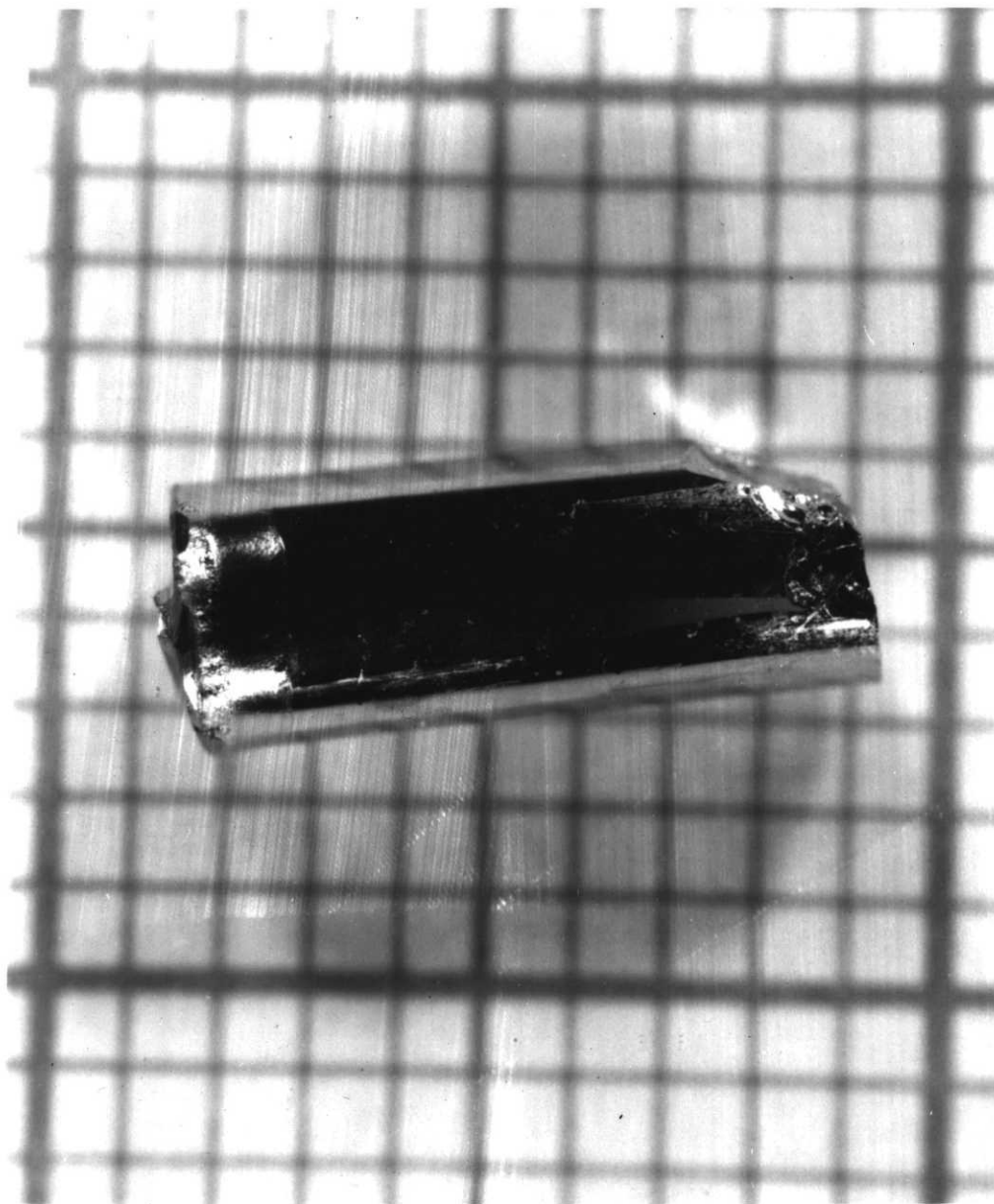


Figure 11 - A  $ZrV_2$  single crystal with a portion of solidified zone remaining on the left. The long triangular reflection is from a (111) facet. Grid divisions = 1.27 mm.

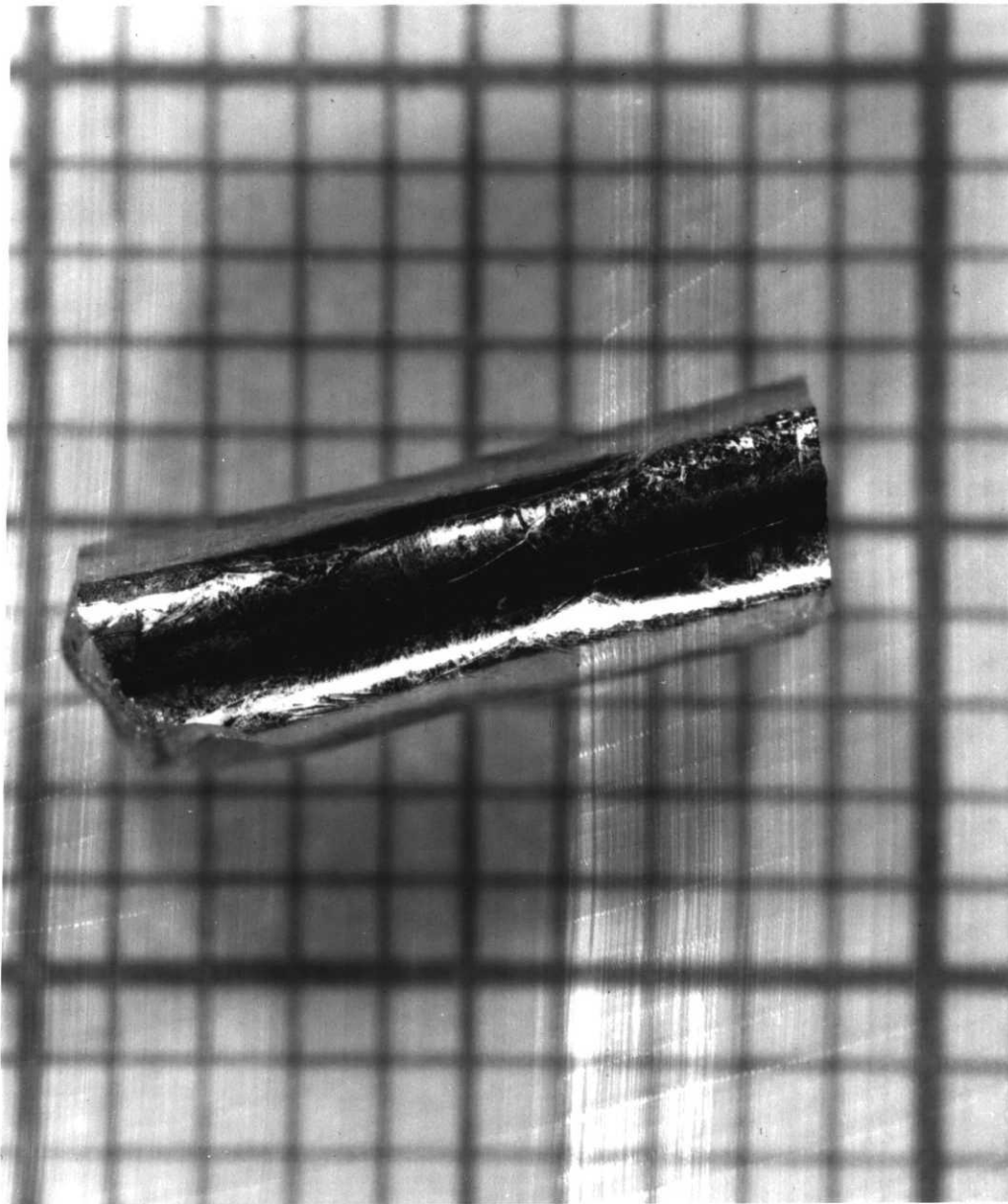


Figure 12 - A section of polycrystal with grain boundaries visible on the surface. Grid divisions = 1.27 mm.

peaks were consistent with the C-15 structure. The data was analyzed by standard methods<sup>20</sup> and the lattice constant  $a_0$  was determined to be  $7.4458 \pm .0004$  A. This is slightly larger than the value of  $7.4414 \pm .0005$  A. reported by Moncton.<sup>12</sup> Neutron diffraction measurements of peak width have indicated that the mosaic spread of both single crystals are less than  $0.3^\circ$ , which is the limit of resolution of the neutron diffractometer.

A typical Laue back-reflection X-ray photograph, Fig. 13, was taken on the longitudinal growth axis of the 2mm single crystal. Its orientation is  $\langle 211 \rangle$ . The larger twinned single crystal had a growth axis lying between the  $\langle 110 \rangle$  and  $\langle 321 \rangle$  directions at  $13^\circ$  from the former (this is common to both parts of the twin).

### C. Microstructure

Metallographic samples were prepared by sectioning, mounting, polishing, and etching. The only microstructural features observed in the single phase material were grain boundaries, twins, and etch pits like the ones shown in Figs. 4 and 5. Etch pits such as these can have their origin in one of three possible ways. They may be due to the etching away of small second phase particles, they may correspond to dislocations, or they may be an etching artifact due to gas bubbles on the surface or imperfections in a semi-protective film of etchant reaction products.

The first possibility was investigated by taking the sample shown in Fig. 5, which had been etched with a mixture of HF and water, and

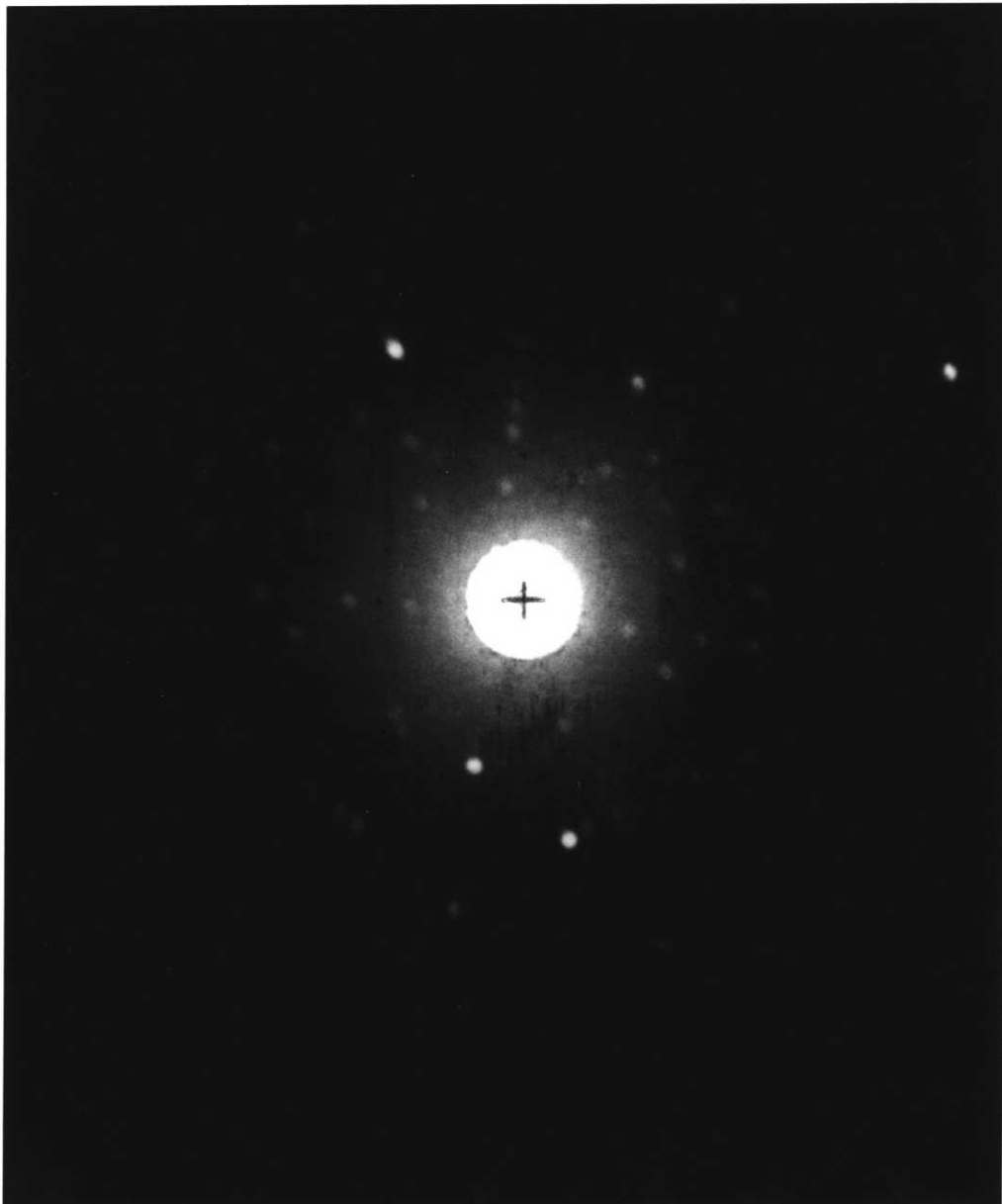


Figure 13 - A Laue back-reflection photograph taken on the longitudinal growth axis of the small single crystal.



repolishing and etching in a solution normally used to reveal grain boundaries, of one part HF, 5 parts  $\text{HNO}_3$ , 5 parts  $\text{H}_2\text{O}_2$ , 5 parts glycerine, and 20 parts water. Another scanning electron micrograph of a similar inclusion is shown in Fig. 14. Here the Zr rich inclusion has been etched away, but the pits do not appear. We may therefore conclude that the pits are not due to a Zr rich phase. A similar comparison with the etching characteristics of V rich regions reveals that the pits are not due to the V rich phase.

In addition, electron beam X-ray analysis in the SEM indicated that all the etch pits and surrounding areas had the same composition as the  $\text{ZrV}_2$  matrix. Furthermore, SEM examination of a fracture surface, shown in Fig. 15, failed to reveal any evidence of inclusions with different fracture properties. Therefore, it may be concluded that the etch pits are not due to a second phase.

To determine whether the pits have their origin in lattice dislocations, a transmission electron microscope study was undertaken. Sample wafers were cut by string saw (a wire passed through an abrasive slurry and then over the sample) and thinned first by grinding on SiC abrasive paper, and then by ion bombardment.

No microstructural features of any kind were observed. A typical region is shown in Fig. 16. The salt and pepper effect on the bend contours is due to the ion bombardment process. It must be noted however, that the ion thinning in this case produced only small thin areas surrounded by thicker material which is opaque to electrons. Because



Figure 14 - A scanning electron micrograph of a Zr stringer in the same sample as in Fig. 5, but which has been etched with a different solution. Mag. X2000.

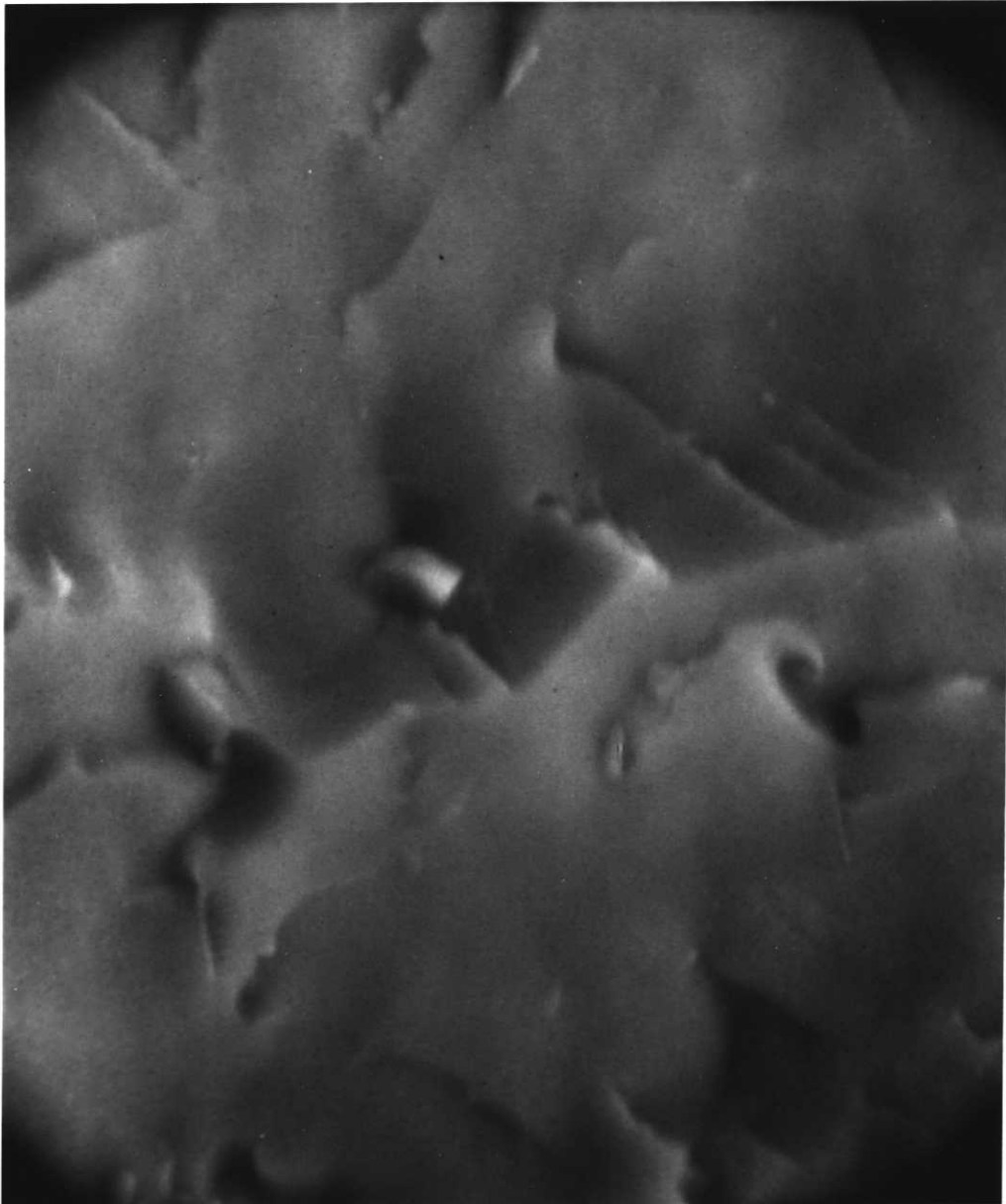


Figure 15 - A scanning electron micrograph of a ZrV<sub>2</sub> fracture surface. Mag. X9,000.



Figure 16 - A transmission electron micrograph of single phase  $ZrV_2$ , showing no structure. Mag. X54,000.

the typical region was only  $10^{-7}$  cm<sup>2</sup> in area, it can only be said with absolute certainty that the dislocation density is less than  $10^7$ /cm<sup>2</sup>. The observed etch pit densities are between  $10^7$  and  $10^8$ /cm<sup>2</sup> and furthermore, the pits are not uniform in size, which implies that their numbers increase with time of etching. Therefore we conclude that the pits are not due to dislocations, but rather are an artifact of the etching process, and furthermore, that the actual dislocation density is something less than  $10^7$ /cm<sup>2</sup>.

#### D. Spark Erosion Damage

Transmission electron microscope specimens were also prepared using a standard spark erosion method to cut 0.5 mm thick wafers of the material before thinning. These specimens differed markedly from those cut by string saw.

A typical region of a spark cut sample is shown in Fig. 17. Second phase particles are visible, as are numerous stacking faults. The particles occupy too small a volume relative to the minimum objective aperture of the microscope to yield an identifiable diffraction pattern; however, it is believed that they consist of ZrH, the hydrogen being introduced by the dissociation of the kerosene in the spark cutter cooling bath.<sup>21</sup>

The stacking faults may have been produced by the spark generated shock waves and provided nucleation sites for the ZrH, or conversely, the ZrH may have induced strains which led to the formation of stacking faults. In any case, these effects are visible at the center of the



Figure 17 - A transmission electron micrograph of a spark-cut sample showing second phase particles and stacking faults.

Mag. X60,000.

wafer, some 250  $\mu\text{m}$  from the spark cut surface. This would indicate a rapid room temperature diffusion of H in  $\text{ZrV}_2$ .

One spark cut wafer was crushed and examined in a Debye-Scherrer X-ray camera. The lattice constant was found to be  $7.472 \pm .001$  A., which is about 0.3% larger than the clean material, thus confirming that the observed particles are a result of the spark erosion.

#### E. Hardness

As a first examination of the mechanical properties of  $\text{ZrV}_2$ , microhardness measurements were made on a clean polycrystalline sample which had been prepared by mounting, sectioning, and polishing. The final polishing step employed .06  $\mu\text{m}$  alumina abrasive powder. Hardness was then measured using a Knoop microhardness testing apparatus. The averages of several measurements at each of four applied loads are shown in Table I, along with the corresponding Knoop and equivalent Rockwell "C" values. It is apparent that the polishing process left a work-hardened layer about 4  $\mu\text{m}$  thick.

The fracture surface shown in Fig. 15, obtained from a sample that was chipped in handling, reveals a completely brittle mode of fracture. Thus it appears that while a small amount of plastic deformation is possible at room temperature, the material is essentially brittle in nature.

Table I

Hardness values and penetration depths for different applied loads on clean polycrystalline material

<u>Load(g)</u>	<u>Indenter Penetration (<math>\mu\text{m}</math>)</u>	<u>H<sub>knoop</sub></u>	<u>R<sub>c</sub></u>
100	2.1	351.7	35
300	3.8	327.8	32
500	5.3	291.9	27.5
1000	7.4	288.6	27



#### IV. LATTICE TRANSFORMATION AND SOFT MODES

##### A. Introduction

One of the most fundamental attributes of a displacive phase transformation is the changes in crystal symmetry which it entails. Thus if a soft mode mechanism is involved in the transformation, its symmetry should have some definite relation to the crystal symmetries. Similarly, a transformation driven by changes in electronic configuration will reflect an alteration of the band structure symmetry.

Inoue and Tachikawa<sup>22</sup> have reported a cubic to orthorhombic distortion in  $ZrV_2$ , but Moncton<sup>12</sup>, using powder neutron diffraction methods, found arc-cast  $ZrV_2$  to undergo a cubic to rhombohedral transformation upon cooling through 117°K. This distortion should consist of a contraction along the body diagonal of the unit cell, and an expansion on two  $\langle 110 \rangle$  directions normal to that diagonal.

The work reported here has involved the examination of three samples by single crystal neutron diffraction methods. These were the small single crystal, the large twinned single crystal, and a large grain inclusion filled polycrystal. All three were examined for evidence of a transformation, and the transformation temperature  $T_m$ . In addition, the rhombohedral nature of the transformation was confirmed, and the data from the large twinned single crystal was used to calculate its magnitude, and to search for a sublattice distortion corresponding to what seemed to be the most likely soft phonon mode consistent with the rhombohedral distortion. This mode was chosen on the basis of a group theoretical analysis of possible

phonon modes as described in Appendix I.

The work was performed with a high resolution triple axis neutron spectrometer. Neutrons have the advantage over X-ray methods of sampling the entire volume of the crystal, rather than just the surface. In addition, the apparatus used was specifically designed for this kind of work.

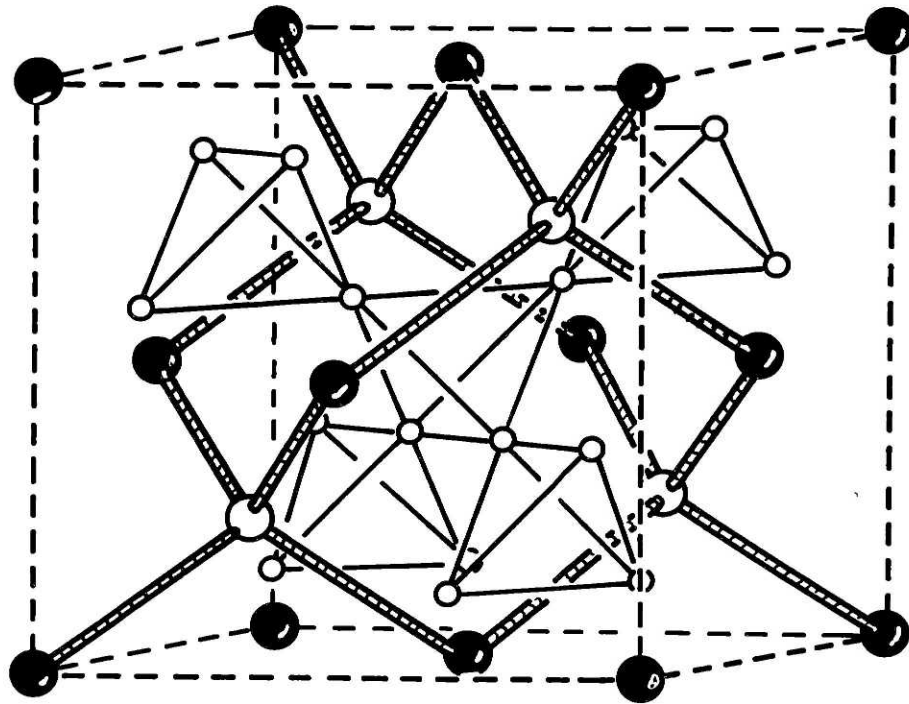
### B. Crystal Structures

The high temperature phase has the C-15 or cubic Laves phase structure with space group  $Fd\bar{3}m (O_h^7)$ . The positions of the eight Zr atoms and sixteen V atoms in the unit cell are shown in Fig. 18. The Zr's lie on two FCC lattices, one with its origin at the point (0,0,0), and one at  $(1/4, 1/4, 1/4)a_0$ , which together form a diamond structure. The V's are arranged in tetrahedra of four atoms each which surround the points of an additional FCC lattice with its origin at  $(3/4, 1/4, 1/4)a_0$ . Their positions are  $(5/8, 5/8, 5/8)a_0$ ,  $(7/8, 7/8, 5/8)a_0$ ,  $(7/8, 5/8, 7/8)a_0$ , and  $(5/8, 7/8, 7/8)a_0$ , and equivalent positions.

To describe the structure in the low temperature phase, it is convenient to use hexagonal lattice vectors where the c axis is along the cubic  $\langle 111 \rangle$  direction, and the a axes along two  $\langle 110 \rangle$  directions normal to the  $\langle 111 \rangle$ . Then the strains may be expressed as simple contractions and expansions of the c and a axes. The new lattice vectors become

$$c = \sqrt{3} a_0 (1 + \epsilon_c) = \sqrt{3} a_0 \delta_c$$

$$a = \frac{\sqrt{2}}{2} a_0 (1 + \epsilon_a) = \frac{\sqrt{2}}{2} a_0 \delta_a$$



- fcc Zr atoms;  $(0,0,0)$  origin
- fcc Zr atoms;  $(\frac{1}{4}, \frac{1}{4}, \frac{1}{4})$  origin  
(tetrahedral diamond lattice sites)
- V atoms

Figure 18 -  $ZrV_2$  atom positions in the C-15 structure.

where  $a_0$  is the cubic lattice parameter just above  $T_m$ , and  $\epsilon_c$  and  $\epsilon_a$  are the lattice strain parameters.

A simple rhombohedral distortion is consistent with space group  $\bar{R}3m (D_{3d}^5)$ . This is also consistent with the optic phonon mode described in Section C. However, data was taken from too few reflections to conclusively demonstrate that this is in fact the low temperature space group.

### C. Soft Mode Analysis

To investigate the possible presence of a soft mode mechanism, it is first helpful to consider the possible phonon modes and their symmetries, and determine which ones are most likely to be present. These would be the ones consistent with the observed lattice distortion. It may be noted that in some systems, for example  $Nb_3Sn$ , a soft mode occurs with a symmetry which is different than the observed lattice strain. However, as a first guess, we look for modes consistent with the overall distortion.

To simplify matters, we may reasonably assume that the phonons in question are of either very long wavelength (Brillouin zone center) or very short wavelength (zone edge). A zone edge phonon requires that the displacements of the atoms one lattice translation apart be exactly out of phase. Therefore, a condensation of this type of mode would result in a change in the translational symmetry, the new lattice vector being twice the length of the old, with a corresponding change in unit cell dimensions. Because Moncton's<sup>12</sup> and the present results do not show a doubling of unit cell volume, the zone edge modes may be ruled out.

We therefore focus our attention on the zone center modes.

The formalism of group theory may be used to calculate the symmetries of the phonon modes of a lattice. Such an analysis has been carried out for the  $\text{ZrV}_2$  zone center modes. The details are described in Appendix I. The results are that, because no symmetry operation interchanges Zr and V positions, the modes of the Zr's and V's may be treated separately. The Zr modes include one threefold degenerate acoustic mode of  $\Gamma_{15}^-$  symmetry, and one threefold degenerate optic mode of  $\Gamma_{25}^+$  symmetry in which the atoms of the sublattice with origin at (0,0,0) move in opposition to those of the sublattice with origin at (1/4,1/4,1/4). In order to be consistent with a rhombohedral distortion, the displacements we are seeking must retain the threefold symmetry of the c axis. The only optic mode that fulfills this condition is polarized along the c axis. Therefore, we would hope to find a sublattice distortion consisting of a change in the distance between Zr atoms on the c axis relative to the positions inherent in a simple rhombohedral strain.

#### D. Experimental Apparatus and Procedures

The neutron diffraction measurements were taken using a triple axis spectrometer at the High Flux Beam Reactor at Brookhaven National Laboratory. A diagram of the beam path is shown in Fig. 19. The main beam channel is set at an angle to the reactor wall to decrease the escape of gamma radiation from the reactor core. The primary monochromating crystal determines the wavelength of the incident neutron

beam. A pyrolytic graphite filter, when used with low energy neutrons (in this case 13.5meV), decreases  $\lambda/2$  contamination by a factor of  $10^5-10^6$  with a primary beam intensity loss of only 50%. The beam passes through the collimator and to the sample mounted in a liquid  $N_2$  or liquid He cryostat on the triple axis stage. Sample temperature is controlled by a small resistance heater, and measured with a platinum resistance thermometer. The diffracted beam passes the second monochromator and the receiving slit and thence to the detector. The second monochromator is, in this case, set to receive the same wavelength as the primary beam, although this may be varied for inelastic scattering studies.

The triple axis stage allows  $360^\circ$  rotation about a vertical axis and  $10^\circ$  from the vertical about the other two mutually perpendicular axes lying in a horizontal plane. The crystal is mounted with an  $\langle hkl \rangle$  direction parallel to the vertical axis, so that the  $(hkl)$  reciprocal lattice plane is in a horizontal attitude. Thus diffraction from reflections in that plane can be obtained by horizontal rotation of the crystal and variation of the  $2\theta$  angle between the incident and diffracted beams. The Ewald sphere construction is shown in Fig. 20. The crystal is located at the origin of the reciprocal lattice with reciprocal lattice vectors  $G$ . Reflection can occur for points which lie on the small circle formed by variation of the angle between the incident and diffracted neutron wavevectors  $k_0$  and  $k$ . Rotation of the crystal sweeps the small circle around the origin, giving access to all points on the plane within the larger circle. In addition, a finite vertical resolution allows detection of reflections corresponding to points slightly above and below

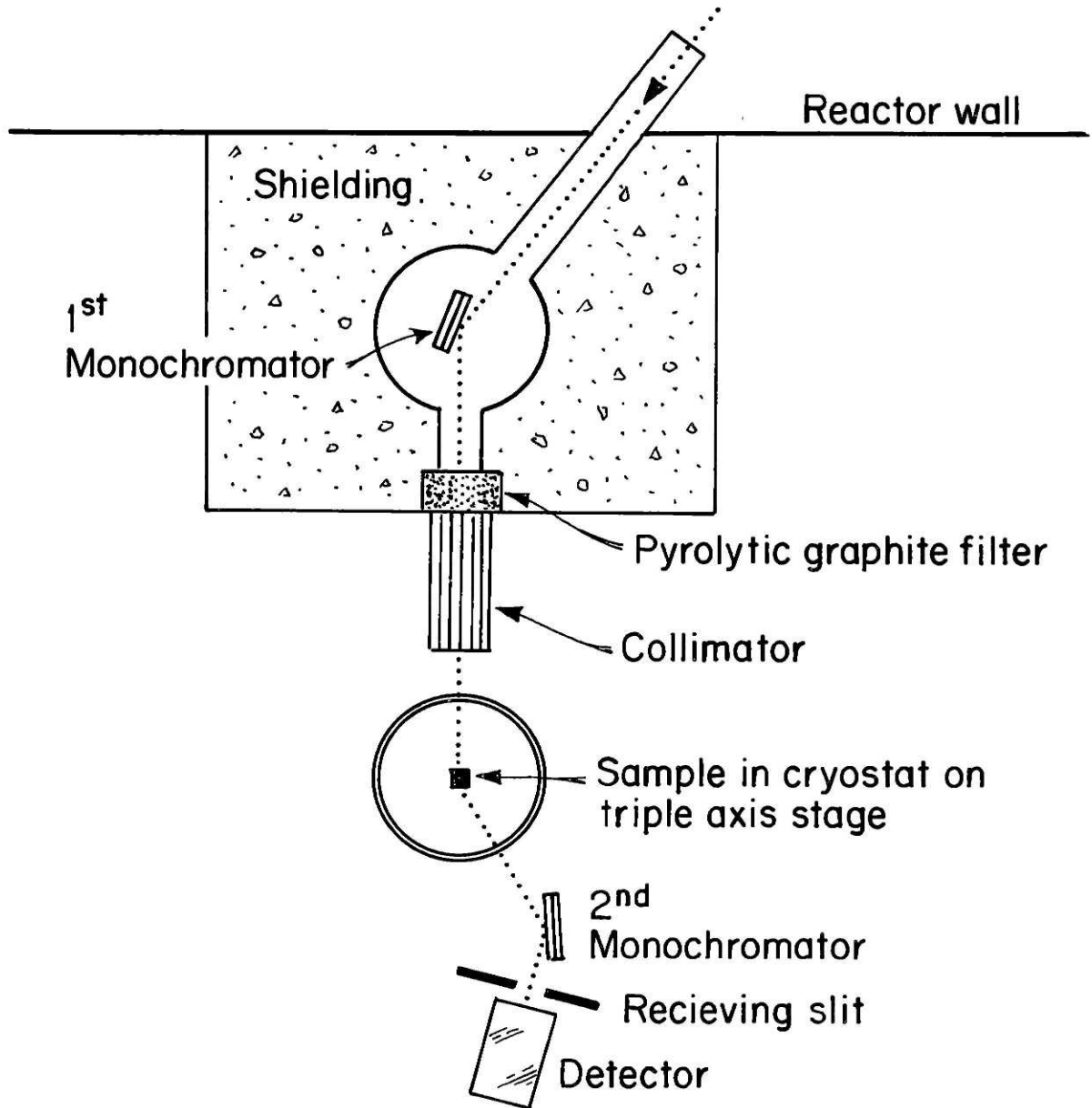


Figure 19 - Diagram of the neutron spectrometer and beam path.

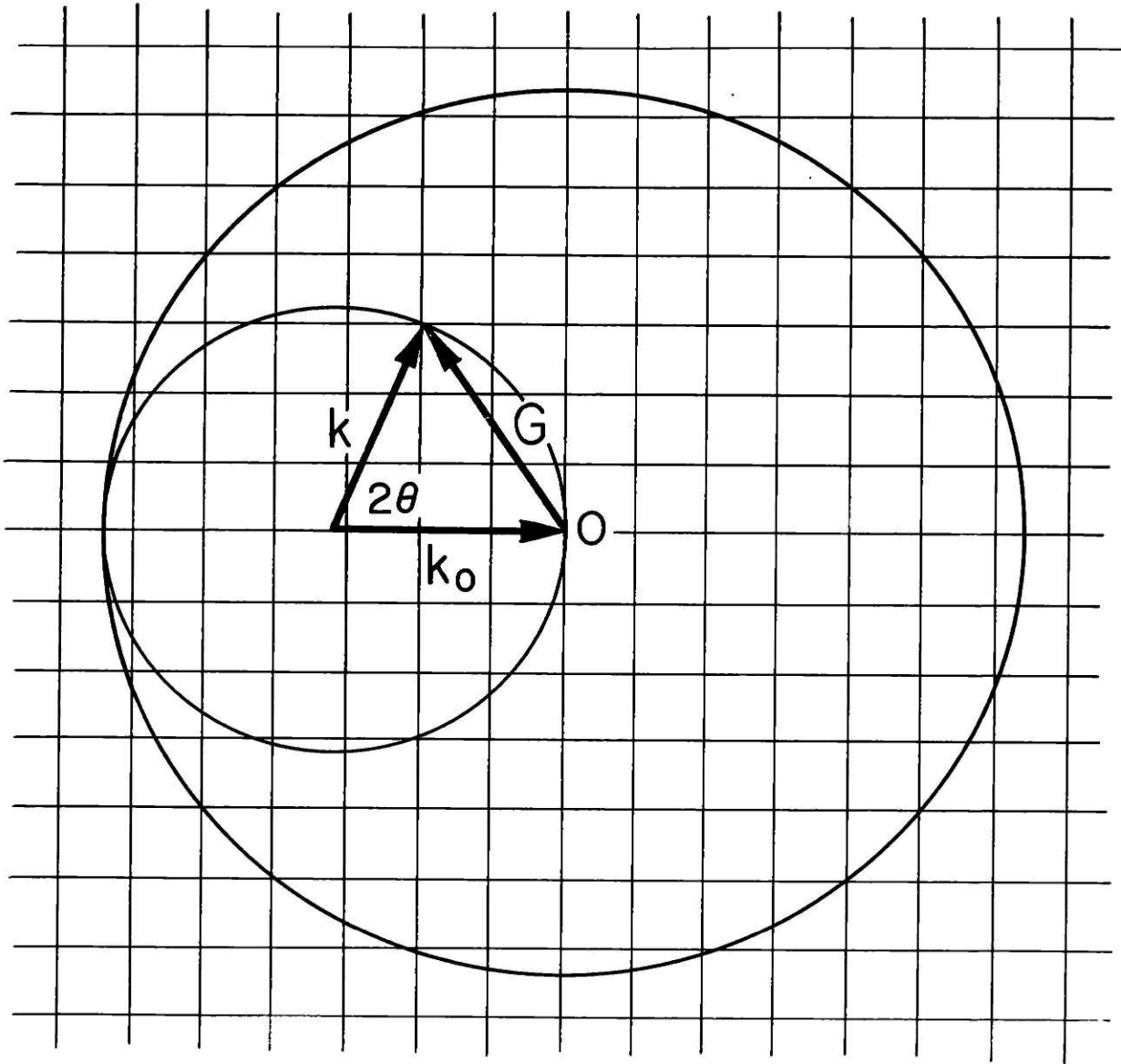


Figure 20 - The Ewald sphere construction for the neutron spectrometer



the plane lying within an angle of  $\pm 1.5^\circ$  from the origin.

A small digital computer was used to control the movements of the spectrometer, and could be programmed to count diffracted neutron intensity at a single point on the reciprocal space plane, along a line of points, or on a grid of points. Data was taken for the twinned single crystal from the (h<sub>1</sub>h<sub>2</sub>k) reciprocal lattice plane. A line of points was used to integrate the intensity of a given peak, and a grid was used to find the shift in peak positions occurring at the phase transition.

Because the primary neutron beam intensity was not constant in time, counting was done at each point until a primary beam monitor attained a predetermined value.

#### E. Results and Data Analysis

Three samples were examined for evidence of a transformation. Of these the small single crystal exhibited no peak splitting or broadening down to 10°K, indicating that no transition occurred. The inclusion filled polycrystal was examined by measuring the diffracted intensity from one grain. This sample showed a pronounced decrease in (111) peak height between 120°K and 115°K, as shown in Fig. 21, thereby indicating the presence of a transformation.

The large twinned crystal also exhibited a transformation. Because of its greater volume, and thus greater diffracted intensities than the polycrystal grain, it was used to determine the low temperature structure and look for the sublattice distortion. The intensity of the (111) is

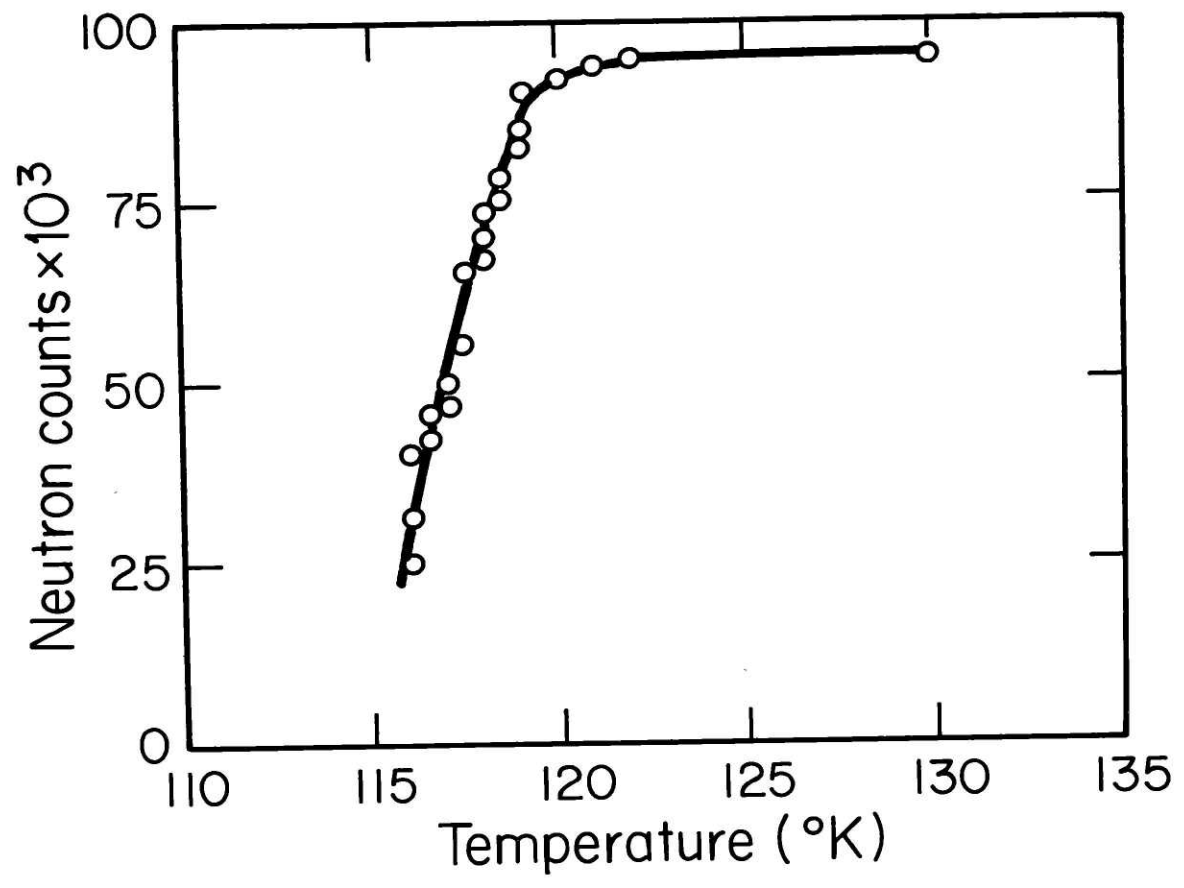


Figure 21 - (111) peak height vs. temperature for one grain of an inclusion filled polycrystal.

shown in Fig. 22. The transition starts at 99°K and the peak intensity grows as domain formation appears, increasing the crystal's mosaic spread and thus diminishing extinction effects. There are four possible domain types, corresponding to distortions along each of the four body diagonals of the cube. As the transformation proceeds, the (111) peak splits into the hexagonal (00.3) and three (10.1) reflections of the rhombohedral phase. The intensity at the (111) reciprocal space position continues to decrease with temperature until, at about 87°K, the rhombohedral peaks have shifted enough to yield no contribution, and a residual (111) reflection remains. Note that the apparent temperature at which this occurs is somewhat dependent on the spectrometer resolution. The residual peak height indicates that about 30% of the volume remains untransformed.

Also shown in Fig. 22, is the intensity vs. temperature measured at the reciprocal space position occupied at 79°K by one hexagonal (11.0) reflection descended from the cubic (220). This intensity decreases with increasing temperature and vanishes at the transition point.

The structure in the low temperature phase may be calculated from the peak positions and a knowledge of the cubic structure. The positions are determined by counting at a grid of reciprocal space points surrounding the cubic peak positions. If one assumes that the low temperature phase is rhombohedral, expressions can be derived which predict the transformed peak positions as a function of rhombohedral strain. This is done by transforming the reciprocal lattice coordinates into hexagonal coordinates.

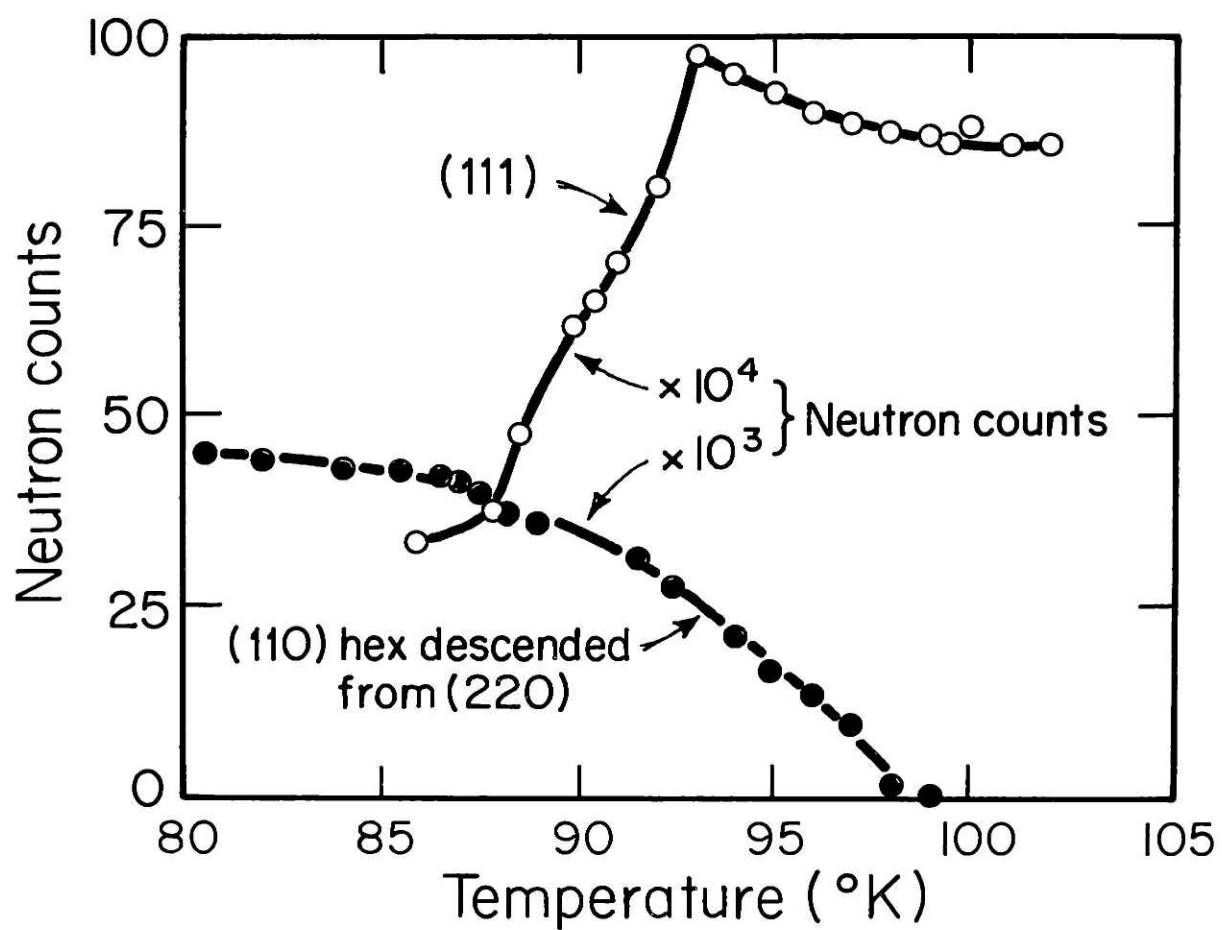


Figure 22 - (111) peak height vs. temperature for the twinned single crystal. Also shown is the height of a (11.0) peak descended from the (220).

If the observed peak positions are consistent with the rhombohedral distortion, then their coordinates may be used to solve for the magnitude of the strain components. These expressions, as well as the data for the peaks descended from the (220) and (004) cubic reflections at 79°K are given in Appendix II.

All peaks were found to be consistent with the rhombohedral distortion. The values of strain calculated using the satellite peaks descended from the (004) are  $\epsilon_a = .0139$  and  $\epsilon_c = -.0256$ , and those from the (220) give  $\epsilon_a = .0127$  and  $\epsilon_c = -.0244$ . The average of the two  $\epsilon_a = .0133$  and  $\epsilon_c = -.0250$  are slightly smaller than the values reported by Moncton<sup>12</sup> of  $\epsilon_a = .0149$  and  $\epsilon_c = -.0297$ . In agreement with those results, within experimental error,  $-\epsilon_c = 2\epsilon_a$ , showing there is no volume change to first order.

To calculate the magnitude of the sublattice distortion expected from the results of Section C, neutron intensity was measured from the  $(1\bar{1}.2)$  reflections descended from the forbidden cubic (002). The structure factor of these reflections is dependent on the magnitude of the sublattice strain. (The structure factors in both coordinate systems are given in Appendix III.) By comparing this intensity with that of a reflection of known structure factor in the high temperature phase, the magnitude of the distortion may be calculated.

For neutron diffraction the integrated intensity of a reflection is given by

$$I = I_o \frac{N^2 \lambda^3 F F^* \exp(-2M)}{\sin 2\theta}$$

where  $I_o$  = primary beam intensity

$N$  = number of unit cells/unit volume

$\lambda$  = neutron wavelength

$F$  = structure factor

$M$  = Debye temperature factor

$2\theta$  = scattering angle

Note that, unlike the expression for X-rays, there is no Lorentz polarization factor here.

To obtain the true intensities of the reflections being compared, it is necessary to consider two effects which, in this case, introduce errors in the measured intensities. The first of these is extinction. In nearly perfect crystals of sufficient volume, and where absorption is low, the diffracted beam may lose intensity by further diffraction. In practice this usually occurs only for strong reflections, and is negligible with weak ones. Fortunately, the present data includes a measure of this effect for the (111) reflection by the increase of intensity shown below  $T_m$  in Fig. 22. If we assume that the weak (222) reflection has no extinction, then we may take the ratio  $F_{(111)}^2 / F_{(222)}^2$  to predict the intensity of the (111). This ratio is 23.02 but the ratio of measured intensities

$$\frac{I_{(111)} \sin 2\theta_{(111)}}{I_{(222)} \sin 2\theta_{(222)}}$$

is only 20.07, so that the predicted intensity is 14.8% more than measured. We may see that this is exactly the increase of (111) intensity shown in Fig. 22. Thus we conclude that the (222) reflection is free from extinction and may be used in the calculation.

The second error is that of double Bragg scattering. This occurs when the sphere of reflection accidentally passes through two reciprocal lattice points, so that the primary beam may be diffracted twice. The resulting intensity will be small, but may contribute significantly to the measured intensity from weak reflections. In order to test for this effect, the crystal is rotated around the scattering vector, thus moving all the reciprocal lattice points from the sphere of reflection but the desired one. The results of Fig. 23 indicate rotation around the scattering vector  $(0,0,1.995)a^*$  corresponding to the two  $(1\bar{1}.2)$  reflections above and below the plane, where  $a^* = \frac{2\pi}{a_0}$ . It is apparent that there is considerable double scattering intensity. Even though the data was taken near the minimum at 0 degrees, some double scattered intensity may still be present, and so the sublattice distortion that is obtained can only be considered as an upper limit.

Taking the ratio of the total intensity from the four  $(1\bar{1}.2)$  reflections and the cubic (222) reflection, and solving for  $F_{(1\bar{1}.2)}^2$  gives

$$F_1^2 = \frac{I_1 \sin 2\theta_1 N_2^2}{I_2 \sin 2\theta_2 N_1^2} F_2^2 \exp[2(M_1 - M_2)]$$

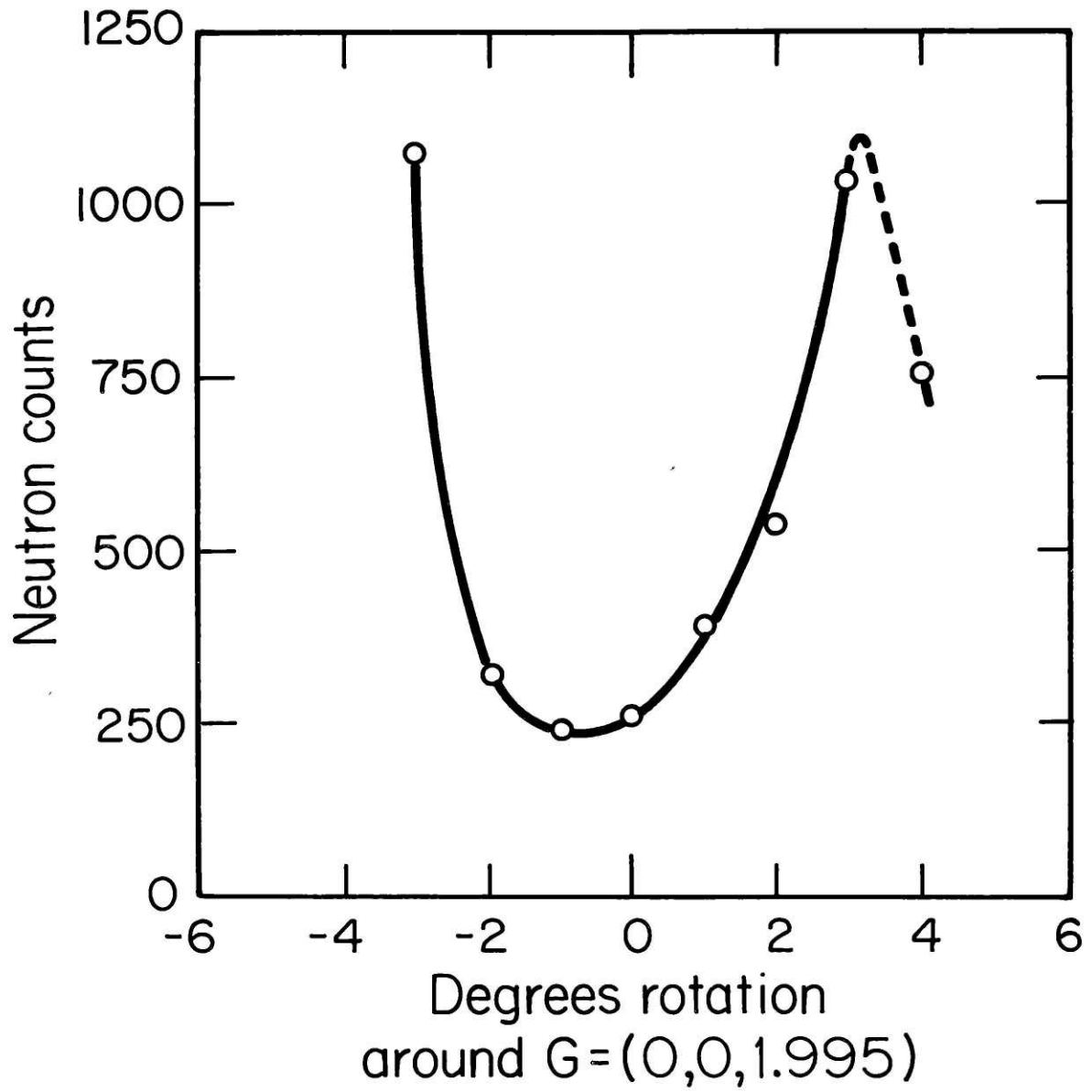


Figure 23 - Double scattered intensity at the reciprocal space position  $(0,0,1.995)$  as a function of rotation around that vector.



where the subscripts 1 and 2 refer to the (1 $\bar{1}$ .2) and (222) reflections, respectively.

In order to minimize the temperature variation between the reflections being compared, data was taken at just below the transition, at 79°K, and just above, at 106°K. Although the Debye approximation is probably not very accurate in the region of the phase transition, it can be used to obtain an approximate correction for the temperature effects, and to show that this correction is small.

The Debye treatment gives the expression for M as

$$M = \frac{6h^2 T}{mk\theta_D^2} \frac{\sin^2 \theta}{2\lambda^2} \left[ \phi(x) + \frac{x}{4} \right]$$

where  $h$  = Plank's constant

$T$  = absolute temperature

$m$  = average atomic mass

$k$  = Boltzman constant

$\theta_D$  = Debye temperature

$\theta$  = Bragg angle

$\lambda$  = neutron wavelength

$$\phi(x) = \frac{1}{x} \int_0^x \frac{\epsilon d\epsilon}{e^\epsilon - 1} \quad \text{where } x = \frac{\theta_D}{T}$$

Using a value of 220°K for  $\theta_D$  derived from specific heat measurements by Rapp and Vieland<sup>8</sup>, and  $\lambda = 2.5505$  A, and

$$\left( \phi(x) + \frac{x}{4} \right) = 1 + \frac{x^2}{36} + \frac{x^4}{3600} + \dots$$

yields the values of  $M_{(1\bar{1}.2)}(79) = .00681$  and  $M_{(222)}(106) = .0230$ . The exponential factor then becomes .9840, which is in fact a small correction.

The structure factors (see Appendix III) for the two reflections are

$$F_{(1\bar{1}.2)} = 36b_{Zr}^2 \cos^2 \frac{\pi}{2} \delta_s$$

$$F_{(222)}^2 = 256b_V^2$$

where  $b_{Zr}$  and  $b_V$  are the Zr and V scattering lengths and  $\delta_s = (1 + \epsilon_s)$  where  $\epsilon_s$  is the sublattice strain. The measured intensity ratio  $I_1 \sin^2 \theta_1 / I_2 \sin^2 \theta_2$  was found to be  $3.94 \times 10^{-3}$  and the ratio of unit cell volumes gives  $N_2/N_1 = 3/4$ .

Substituting these quantities and solving for the structure factor and then  $\delta_s$  gives the upper limit value of  $\epsilon_s = 6.51 \times 10^{-3}$ . It is obvious from the cosine term in the structure factor that the sign of  $\epsilon_s$  cannot be determined from this reflection. This result is of the same order of magnitude as a similar upper limit reported in an X-ray study of arc-cast material by Dobbins.<sup>10</sup>

Because  $\epsilon_s = .26\epsilon_c$ , it appears that the soft mode may in fact be present. However, because of the double scattering contamination, this result is not conclusive. It might be possible to eliminate the double scattering effects in a subsequent measurement by squeezing the crystal along a  $\langle 111 \rangle$  direction. This would tend to induce the transformation of the entire volume in only one domain, thereby substantially reducing the number of reciprocal lattice points, and decreasing the occurrence of

unwanted points on the Ewald sphere.

Of course, the most conclusive test for the existence of this soft mode would be an inelastic neutron scattering study to determine the dispersion curve for this mode as a function of temperature. Any softening would then be immediately obvious.

## V. LOW TEMPERATURE ELECTRONIC PROPERTIES

### A. Introduction

To gain additional insight into the low temperature behavior of  $\text{ZrV}_2$  it is helpful to examine its electronic properties, in this case both the superconducting parameters of critical temperature,  $T_c$ , and resistive critical field,  $H_c$ , and the electrical resistivity as a function of temperature. These properties depend on electron transport and so may be expected to be quite sensitive to factors affecting transport phenomena. Changes in transport properties which may accompany a lattice instability are of two types. First, there is scattering due to electron-phonon interactions, which are dependent on the phonon spectrum. Second is the band structure of the material which determines the number of available conduction electrons and limits the possible scattering processes. Alteration of either the phonon spectrum or the electronic configuration will produce anomalous effects in the electronic properties, although from these measurements it would be difficult to identify which of the factors is responsible. However, a careful examination of these properties will provide a good deal of evidence as to the nature of the lattice instability, and especially how it correlates with the condition of the material as inferred from its microstructure.

Several workers<sup>8, 23</sup> have reported  $T_c$  measurements for arc-cast  $\text{ZrV}_2$ . These samples exhibited broad or double transitions within a range of values. Thus it appeared probable that the superconducting properties of this material would be very sensitive to microstructure.

Therefore, measurements of inductive and resistive  $T_c$ , and resistivity vs. temperature were made on four well characterized samples: the small, non-transforming single crystal, the large twinned single crystal, a clean polycrystal, and an inclusion filled polycrystalline piece. The results could then be correlated with the known microstructures. In addition, resistive  $H_c$  was measured on the latter three samples. Also, the  $T_c$  of the clean polycrystal piece was measured both before and after being removed from the zone and Zr rod which surrounded it when the growth process was halted. There was a marked difference in the two results.

#### B. Apparatus

The inductive  $T_c$  measurements were performed using a mutual inductance apparatus in a liquid He cryostat. This consisted of two coils surrounding the sample and a lock-in amplifier to compare a reference input signal to one coil, with the output signal from the other. As the superconducting transition occurred, the Meissner effect flux expulsion resulted in a changed output signal. The temperature was controlled by a resistance heater surrounding a copper can containing the coils and sample, and was measured with a Ge cryothermometer next to the sample. The copper can was placed in an evacuated pyrex tube which was backfilled with approximately 5 torr of He gas to provide heat exchange with the liquid He bath.

The resistive  $T_c$ ,  $H_c$ , and resistivity vs. temperature measurements were performed using a four point probe apparatus as shown in Fig. 24.

The sample was placed in the polyethylene holder, and nylon screws were used to adjust the tension in small springs holding the copper wire contacts against the specimen. This was necessary because the usual conductive paints would not adhere to the sample surface. A chromel-alumel thermocouple was placed in thermal contact with the sample by the use of a thermally conductive (crycon) grease. A germanium cryothermometer, used to measure temperatures below 30°K, was located on the other side of the holder, opposite the sample. This apparatus was then placed in a copper can with a wire wound resistance heater, and then in an evacuated pyrex tube as described above.

### C. Superconducting Properties

The critical temperature of arc-cast  $ZrV_2$  was first reported by Matthias, et al.<sup>4</sup> as 8.8°K. Subsequently, in inductive measurements on similar material, Smith, et al.,<sup>23</sup> and Rapp and Vieland<sup>8</sup> have observed samples with two distinct transitions, the temperatures ranging from 7.7°K to 8.5°K.

Inductively measured  $T_c$  curves are shown in Fig. 25 for the twinned single crystal, the clean polycrystal, and the inclusion-filled polycrystal. The twinned single crystal shows a sharp transition with onset at 8.75°K, midpoint at 8.72°K, and completion at 8.55°K. The curve for the non-transforming single crystal was almost identical to that of the twinned one, but was slightly sharper, having a width of 0.1°K. The polycrystalline sample shows a double transition consisting of a broad region centered at 8.1°K and a narrower one at 8.6°K. The inclusion

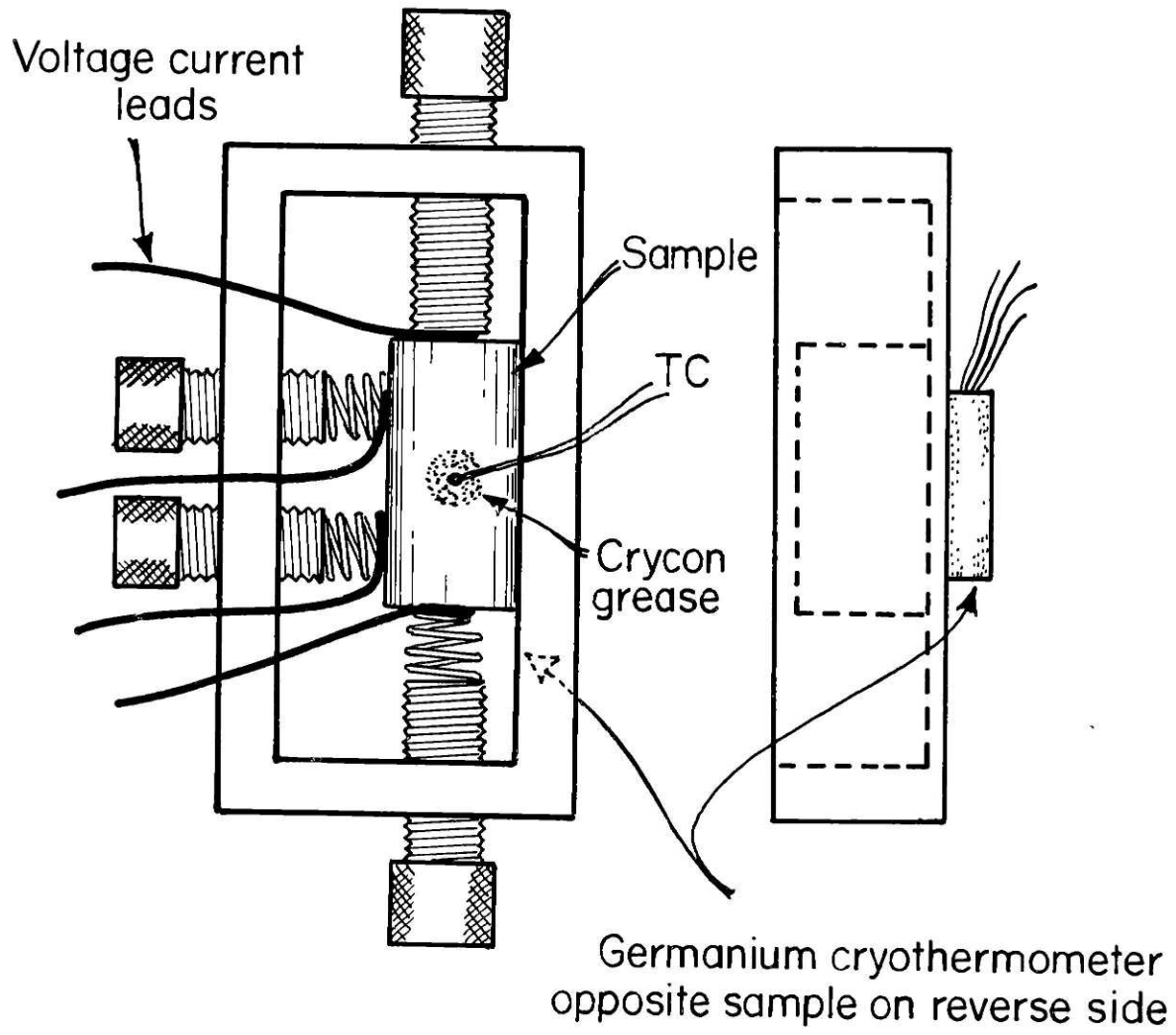


Figure 24 - Four point probe sample holder

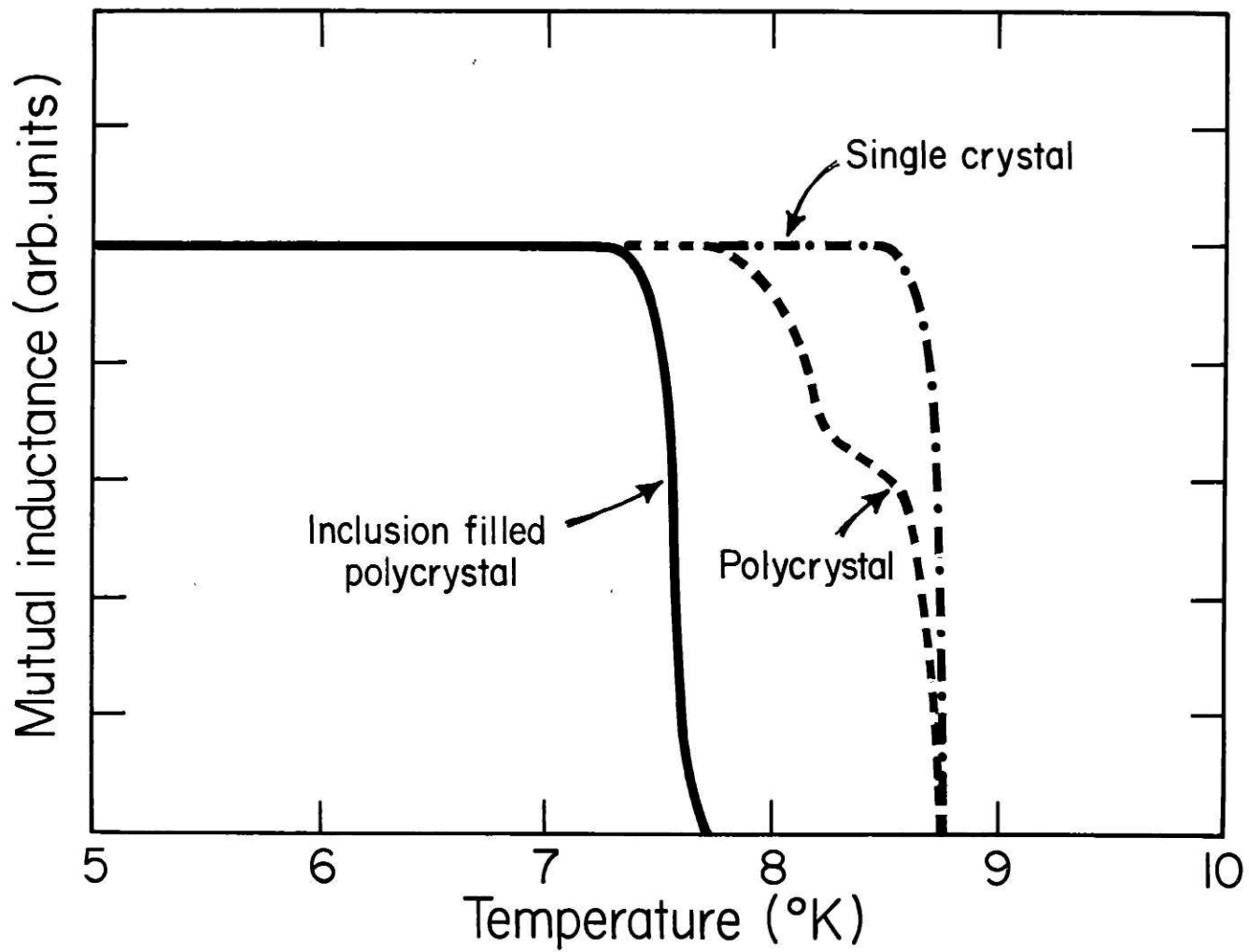


Figure 25 - Inductive  $T_c$  curves for the twinned single crystal, a clean polycrystal, and an inclusion-filled polycrystal



filled sample exhibits a transition with a midpoint of  $7.6^{\circ}\text{K}$  and a width of  $0.4^{\circ}\text{K}$ . It may be noted that one polycrystal yielded identical curves in two measurements taken 15 months apart. This indicates that the material is stable with time, unlike the behavior observed in some arc-cast  $(\text{Hf,Zr})\text{V}_2$  samples.<sup>23</sup> The  $T_c$  of each sample was also measured resistively. In each case, extrapolation to zero current yielded transition midpoints within  $0.1^{\circ}\text{K}$  of those measured inductively.

As mentioned previously, the inductive  $T_c$  of one clean polycrystal was measured before it was removed from the solidified zone and Zr rod left surrounding it when the growth process was stopped, in a configuration similar to that shown in Fig. 3. The transition was observed to occur almost entirely at  $8.0^{\circ}\text{K}$  with a small portion at  $8.6^{\circ}\text{K}$ . With the endpieces removed, the behavior changed to the result described above. The two curves are shown in Fig. 26.

Because the only change between the two measurements was the removal of the endpieces, it is apparent that the  $T_c$  is acutely sensitive to stresses or localized microscopic strains in the crystal. Residual stress would be produced by the rapid solidification of the zone, and by the cooling of the crystal with different coefficients of thermal expansion of the zone,  $\text{ZrV}_2$ , and the Zr rod. Localized strains would, of course, be present at the interfaces between two phases.

The resistive critical field  $H_c$  was measured as a function of temperature for the twinned single crystal, clean polycrystal, and inclusion-filled polycrystal, using the four point probe apparatus

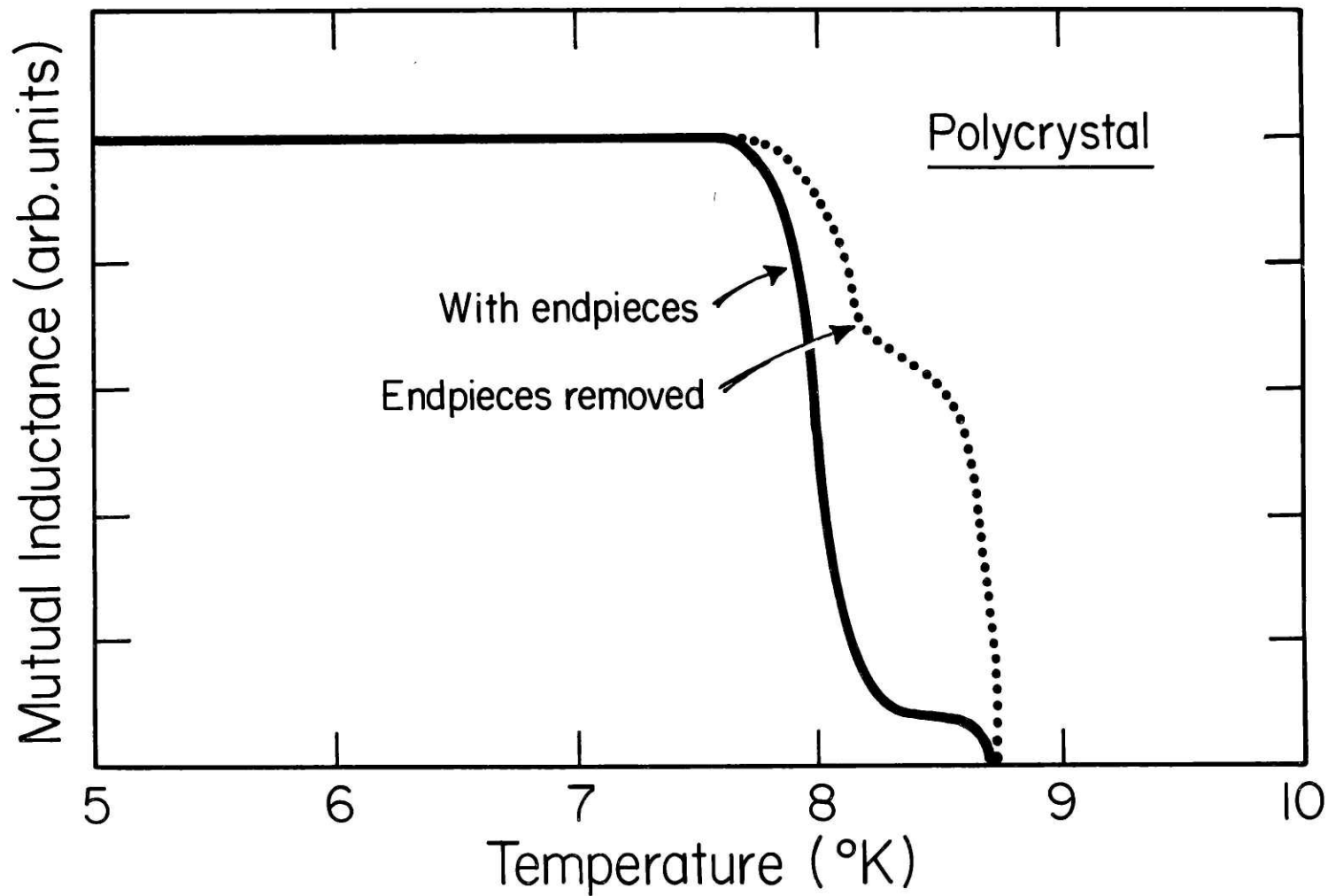


Figure 26 - Inductive  $T_c$  measured before and after removal of endpieces from a clean polycrystal

previously described and a liquid He cryostat in a 150 kG conventional DC magnet at the National Magnet Laboratory. For each data point, the field was varied at a constant temperature.

The observed values of  $H_c$  at 4.2°K were 99 kOe for the inclusion-filled sample, 127 kOe for the twinned single crystal, and 139 kOe for the clean polycrystal. Inoue, *et al.*<sup>24</sup> have previously reported a value of 110 kOe at 4.2°K for arc-melted material.

The complete results are shown in Fig. 27. The error bars indicate the onset and completion of the transitions. The curves are seen to extrapolate nicely to the zero field  $T_c$ 's. It can also be seen that extrapolation of the clean polycrystal curve indicates a possible 0°K field of more than 160 kOe. It is possible that the lower  $H_c$  values of the twinned single crystal compared to the clean polycrystal may be due to the effects of anisotropy, and presumably a different orientation of the crystal would yield similar or greater values than those of the latter.

#### D. Resistivity

The resistivity as a function of temperature was measured from 300°K to 4.2°K using the four point probe apparatus previously described. The temperature was controlled by raising and lowering the sample holder in the cryostat, and measured with the chromel-alumel thermocouple referenced to an ice bath and supplemented by the Ge cryothermometer below 30°K. There is apparently a large thermoelectric potential between Cu and  $ZrV_2$  which gave rise to thermal voltages which were a

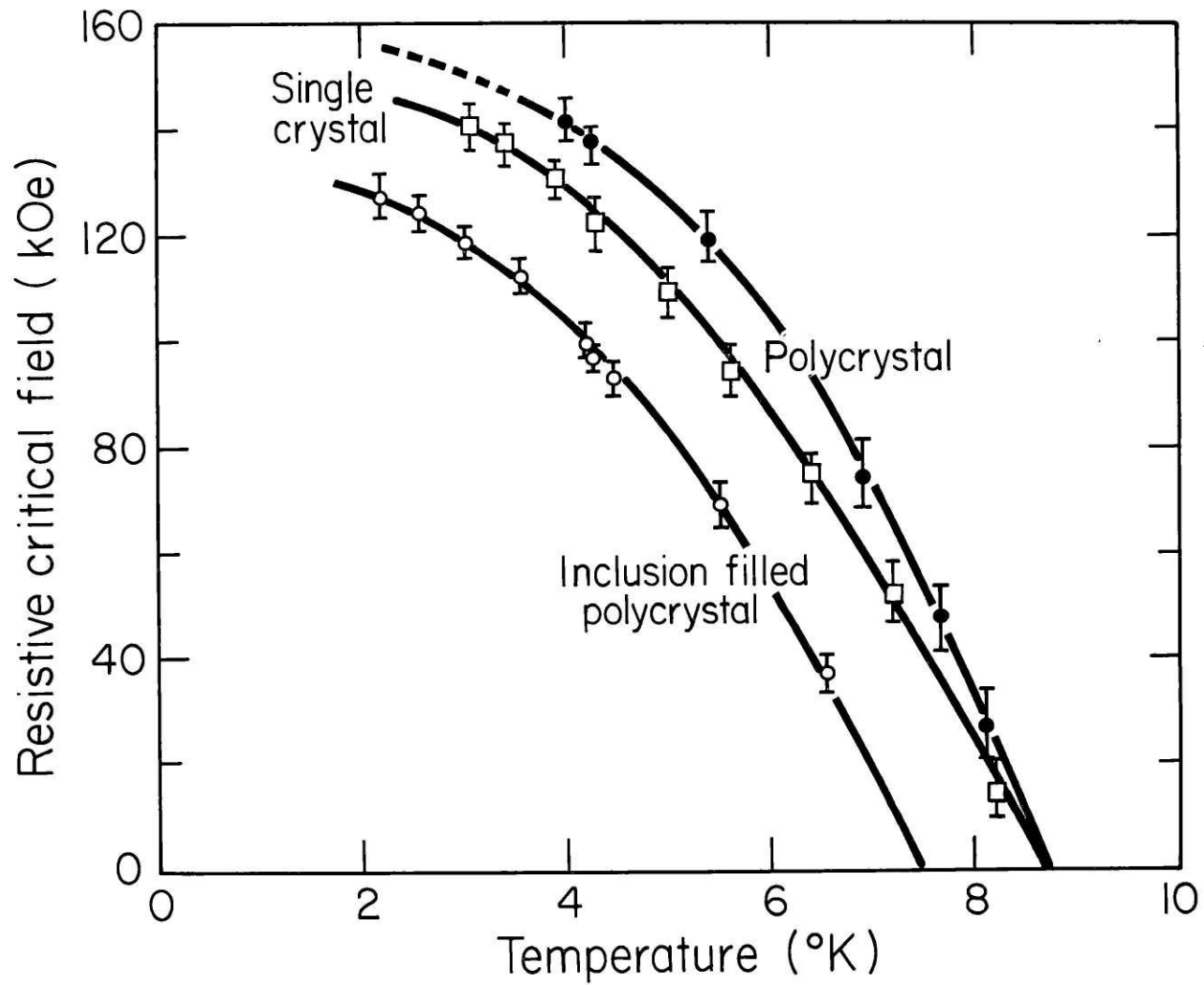


Figure 27 - Resistive  $H_c$  for the twinned single crystal, clean polycrystal, and inclusion-filled polycrystal

significant fraction of the sample signal. This problem was overcome by periodically switching off the current to determine the zero point voltage.

Data was obtained for the twinned single crystal, clean polycrystal, and inclusion-filled polycrystalline samples. The results are shown in Figs. 28, 29 and 30. It may be seen that all the curves are linear with the same slope above 150°K. Below that temperature the slope goes to zero, and all three samples exhibit a hysteretic increase in resistivity, showing that the transformation is thermodynamically first order. The magnitude of the change, the degree of hysteresis, and the onset temperature are all greater for the inclusion-filled material than the twinned crystal, with the clean polycrystal falling in between. A more detailed plot, based on this data between 70°K and 140°K for the three samples is shown in Fig. 31.

A measurement was also made of the resistance of the non-transforming single crystal, but because its cross-section was large compared to the distance between voltage probes, the measured signal was very weak and the data contained a good deal of scatter. The results are shown in Fig. 32. It appears that the overall shape of the curve is very similar to that of the others, flattening and then increasing below about 110°K. This behavior would indicate that whatever factors are responsible for the anomalous transport properties are present even in the absence of the structural transformation.

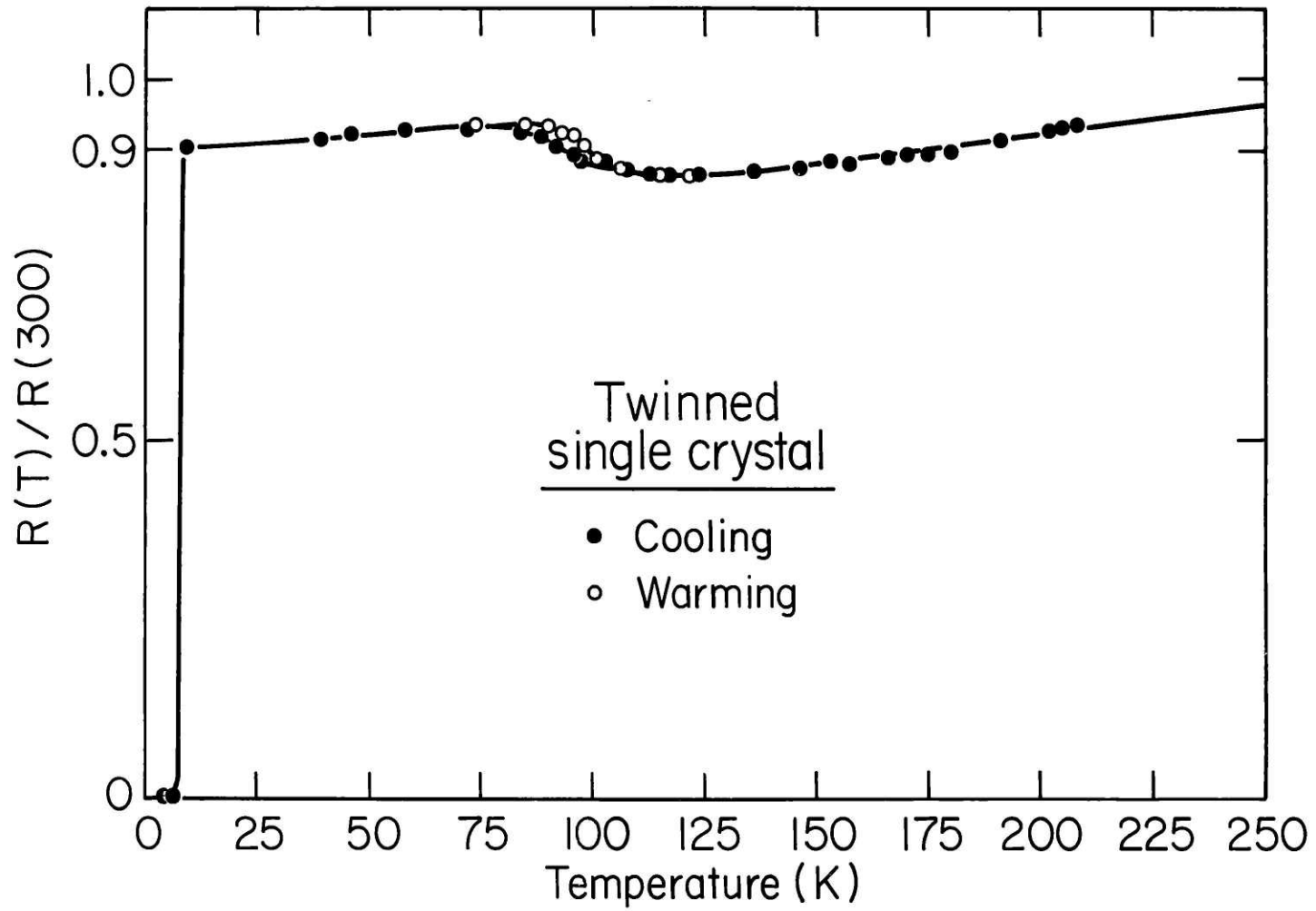


Figure 28 - Resistance vs. temperature for the twinned single crystal

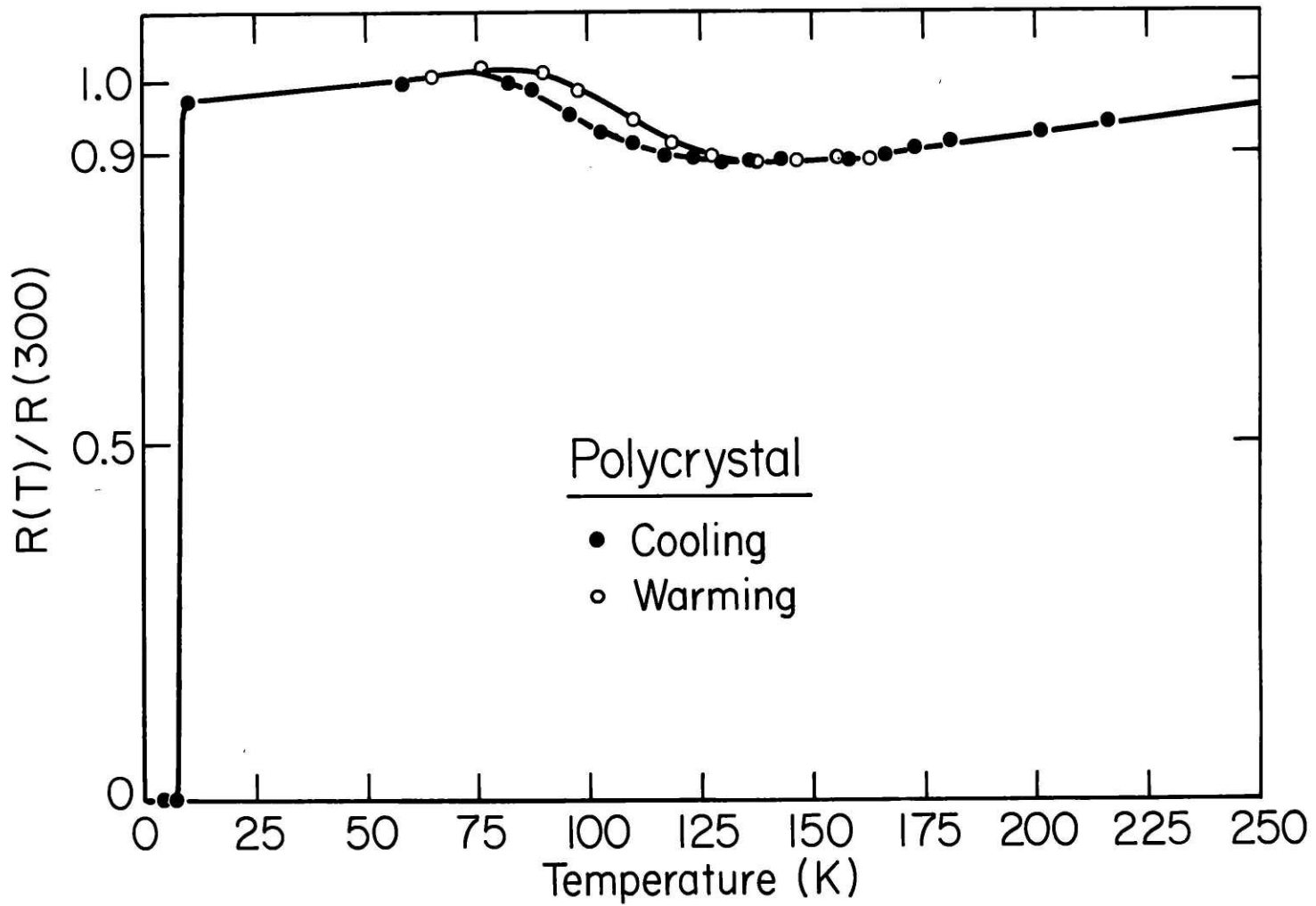


Figure 29 - Resistance vs. temperature for a clean polycrystalline sample

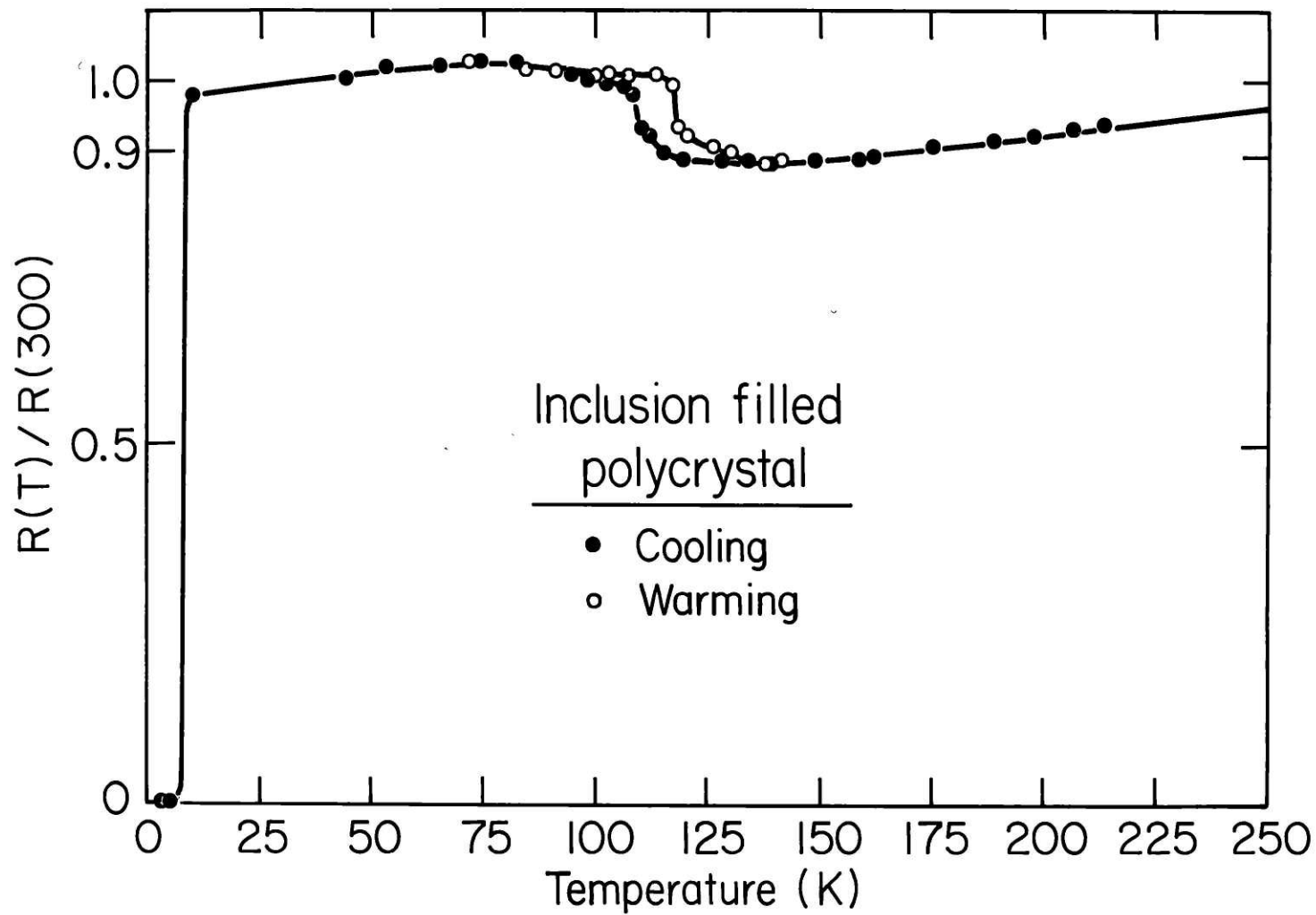


Figure 30 - Resistance vs. temperature for an inclusion-filled polycrystal-line sample



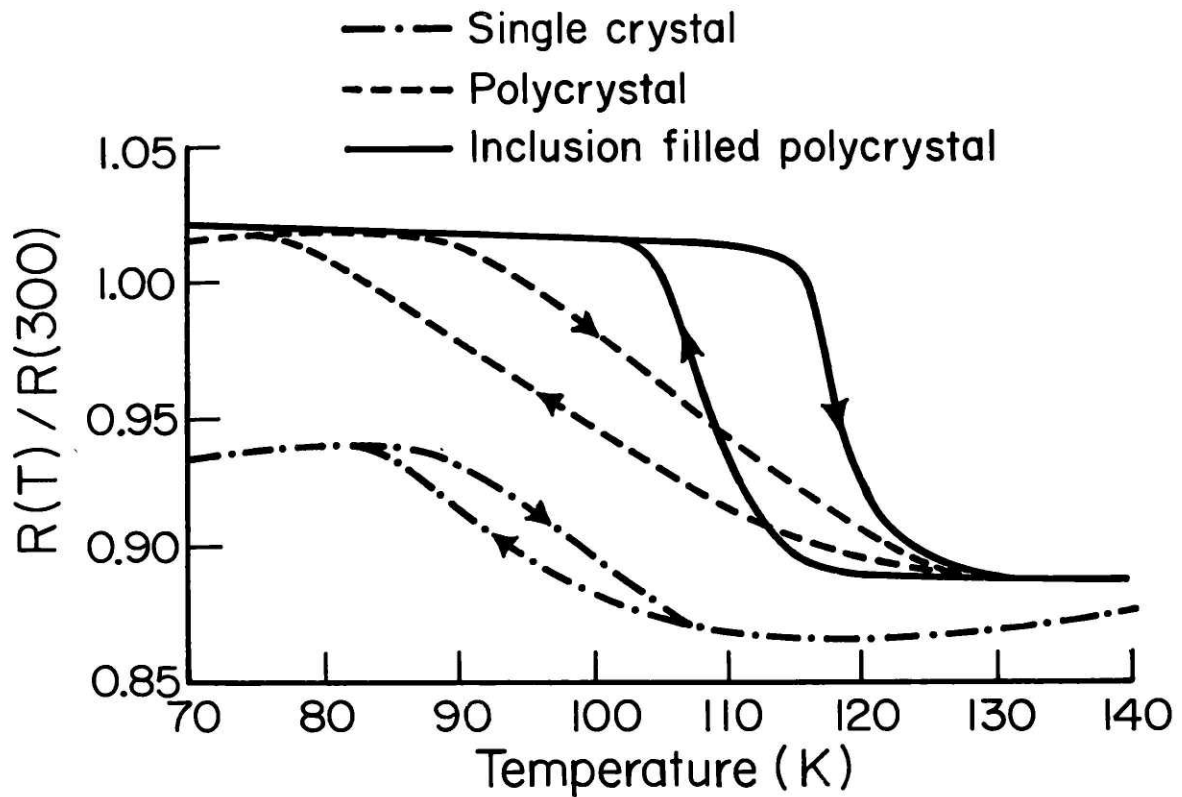


Figure 31 - A more detailed plot of the range 70° to 140°K based on the data in Figs. 28, 29, and 30

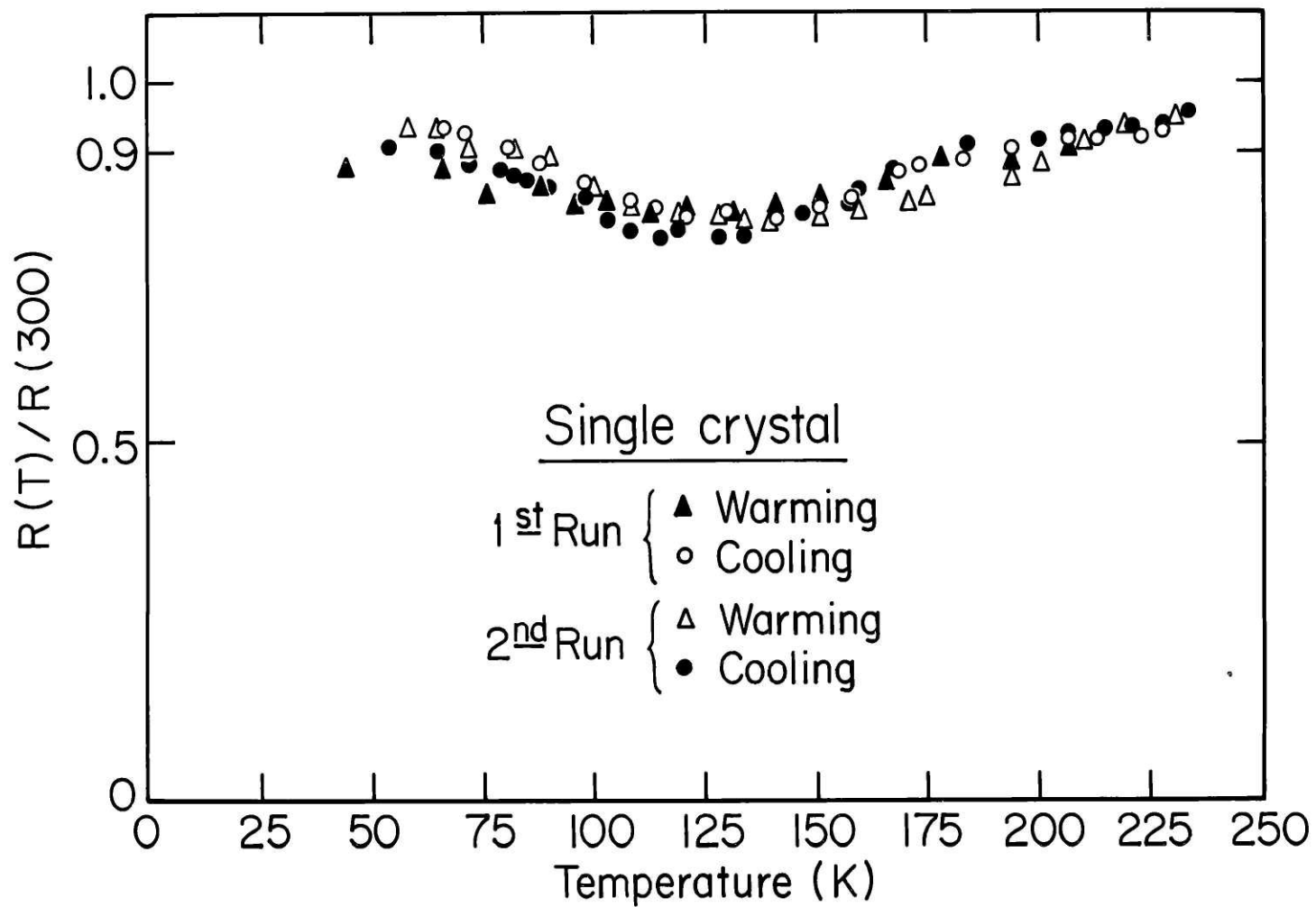


Figure 32 - Resistivity vs. temperature for the small, non-transforming single crystal

Resistivity vs. temperature for arc-cast  $ZrV_2$  has previously been reported by Lawson.<sup>7</sup> That data is shown to follow a curve with a hysteretic anomaly similar in magnitude and temperature to the one shown for the inclusion-filled sample in Fig. 30, but the overall slope of the curve is much greater. However, Fig. 30 appears almost identical to the curve reported in the same paper for the resistivity of  $HfV_2$ . Once again, this points to the importance of the microstructural state on the apparent behavior of these properties.

In comparing the resistivity results with the neutron diffraction data, it is seen that the transport anomalies that give rise to the hysteresis in the resistivity occur over a wider range of temperature than does the lattice transformation. For the twinned crystal, the phase change takes place between about 88°K and 99°K, whereas the hysteresis occurs between 84°K and 105°K. In the same way, the inclusion-filled polycrystal transforms between 115°K and 121°K while the hysteresis is evident between 104°K and 127°K.

To measure the actual value of resistivity at 300°K, a longitudinal section was cut by string saw from a polycrystalline  $ZrV_2$  section, giving a cross-section of .09 cm x .35 cm. A four point probe arrangement was used with a distance between voltage probes of 2.7 cm. It was found that the apparent resistivity changed slightly as a function of applied current. This effect is most likely due to a current "channeling" effect which has been reported in Ga by Gregory, et al.<sup>25</sup> Extrapolation to zero current gives a resistivity of  $120\mu\Omega\text{-cm}$ , which is an order of

magnitude greater than that reported by Inoue, et al.<sup>24</sup> for arc melted material.

## VI. DISCUSSION

### A. Summary

A traveling heater solvent zone technique has been used to produce pure, homogeneous  $ZrV_2$ , including two single crystals. This involved the adaptation of the technique for use in an electron beam floating zone apparatus in high vacuum ( $10^{-7}$  torr). Modifications to the apparatus were required to eliminate several problems including a constitutional supercooling type process which tended to produce Zr rich second phase inclusions in the material. Crystals were grown at a rate of 5 mm/day with a temperature gradient at the liquid-solid interface of more than  $300^\circ\text{C}/\text{cm}$ .

Of the two crystals obtained, one contained a band of five parallel (111) twin planes separating its volume into two roughly equal regions. Both these crystals were used in the ensuing work, along with homogeneous polycrystalline material, and some Zr rich inclusion filled polycrystalline material (approximately 1 vol.%) whose properties differed markedly from those of the clean material, but were similar to those reported in the literature for arc-melted  $ZrV_2$ .

The material had the expected C-15 crystal structure with a lattice parameter of  $7.4458 \pm .0004\text{A}$ . The dislocation density was determined to be less than  $10^7/\text{cm}^2$ , and hardness to be about Rockwell C27.

Neutron diffraction methods were used to investigate the structural phase transformation. The small single crystal exhibited no evidence of a transformation, but the twinned single crystal and an inclusion

filled polycrystalline sample were observed to undergo a rhombohedral distortion below 99°K and 120°K, respectively. The magnitude of the distortion was  $\epsilon_c = -.0250$ , and  $\epsilon_a = .0133$  in agreement with previous work on arc-cast material. A search was made for a sublattice distortion as evidence of a soft phonon mechanism involved in the transformation. An upper limit on this distortion was calculated to be  $\epsilon_s = .0065$ .

The superconducting critical temperature  $T_c$  was found to be 8.75°K for both single crystals, 7.6°K for the inclusion filled material, and the clean polycrystals exhibiting a double transition between the other two. At 4.2°K,  $H_c$  was 99K0e, 127K0e, and 139K0e, for the inclusion-filled material, the twinned single crystal, and a clean polycrystal, respectively.

Resistivity showed anomalous increases below about 127°K for clean and inclusion-filled polycrystals, and below about 105°K for the twinned single crystal. Hysteresis in the resistivity curves indicates that the transformation is thermodynamically first order. The non-transforming single crystal showed a resistivity curve shape similar to the other, transforming samples.

## B. Conclusions

First, as regards the problems with obtaining single crystals, it is clear that this is possible using the solvent zone crystal growth technique which has been described. The major difficulties are the result of the very narrow tolerances allowable for the growth parameters of zone composition and solidification front velocity. These tolerances are

established by the form of the phase diagram (thermodynamic properties) and by the apparently very small diffusion constant of Zr in the liquid. Thus the primary consideration is to maintain adequate precision and control in the crystal growth apparatus.

As stated in Chapter II, the problems with twins and non-single crystal material which limit the percentage yield of single crystals could most likely be solved by the use of seed crystals. Once seed crystals become available, the only additional requirements would be an initial zone of the correct composition, and an adequate means of cooling the end of the seed.

The measurements performed on the various samples show features of their behavior which allow certain conclusions to be drawn. The only significant physical difference between the samples is the presence or absence of twins, grain boundaries, and inclusion particles. Therefore, the differences in their various properties must be due to localized stresses or microscopic strains associated with these defects.

There has been a common speculation in the literature which attributes the double transitions observed in various inductive  $T_c$  measurements, to transformed and non-transformed material. It is apparent that, at least for the  $ZrV_2$  system, this explanation is incorrect. Both the single crystals showed almost identical single, sharp  $T_c$  curves even though the one crystal did not transform, and the twinned single crystal had 70% of its volume transformed. Rather, it appears that  $T_c$  is sensitive to the microstructural perfection of the material, in terms of crystal-

lographic discontinuities and defects. Thus the inclusion-filled material, with a higher defect level (especially considering that the Zr rich phase undergoes a BCC to HCP eutectoid transformation upon cooling through 777°C), has the lower  $T_c$ , while the more perfect single crystals have the higher  $T_c$ .

It may be noted that the difference of defect level implied by the presence or absence of twin planes has no effect on  $T_c$ , while grain boundaries cause pronounced changes. Also, because no  $T_c$  values less than 7.6°K have been reported for arc-cast material, which presumably has numerous defects, it is probable that this value represents a lower limit for  $ZrV_2$ . These two phenomena suggest that there is some kind of activation barrier here, which requires a certain defect level to cause a lower  $T_c$ , but beyond some greater level, there is no additional change.

The transformation temperature  $T_m$  also appears sensitive to lattice perfection.  $T_m$  decreases with increasing perfection and goes to less than 10°K in what we may assume is a very well ordered small single crystal. In addition, all previous work with arc-cast material has shown anomalies in the vicinity of 120°K, and no higher. Here again there would seem to be an activation barrier which must be surmounted before a structural transformation can occur. However, this barrier is somewhat different than the one involved with the  $T_c$  values, because a comparison of the behavior of the two single crystals shows that the twin planes are sufficient to nucleate the transformation, but not to lower  $T_c$ .



A theory which may account for the presence of an activation barrier in the structural transformation has been proposed by Clapp.<sup>27,28</sup> This theory concerns first order displacive transformations which involve localized phonon modes existing in the vicinity of strained or discontinuous regions of the lattice. These modes, by softening, will drive the strained region and surrounding areas into a state of mechanical instability, and thus precipitate the transformation. It is clear that this process will depend on the nature and magnitude of the localized strain fields, and so account for the variation of  $T_m$  with defect level that has been shown in this work.

However, the localized mode softening does not require any change in the normal phonons of the bulk lattice. Thus, if the optic phonon mechanism which has been investigated here does exist, it would cast doubt on the usefulness of Clapp's theory in this case. In addition, the theory predicts a large increase in ultrasonic attenuation near  $T_m$ . The attenuation for the twinned single crystal is shown in Fig. 37, and it appears that no increase occurs. However, it may well be that the absorption takes place over a very narrow temperature range, and may have occurred between the points indicated in the figure. Also, any ultrasonic attenuation may require a very close coincidence of propagation and polarization vectors between the soft modes and ultrasound waves, which may not have been achieved in these measurements. Moreover, Doherty and Gibbons<sup>9</sup> have reported large increases in internal friction near 120°K in arc-cast material, which would indicate an absorption of vibrational energy. Obviously, this question must be investigated in more detail.

The very unusual behavior of the resistivity indicates anomalous effects in either the phonon spectrum or electronic band structure. (Moncton<sup>12</sup> failed to find any evidence of magnetic ordering in  $ZrV_2$ .) Because these effects seem to persist even in the absence of a crystallographic transformation, it appears that a change in electronic configuration provides a driving force for the transformation, which will actually occur only when some nucleation barrier has been overcome. This kind of driving force is again very similar to the one theorized for the A-15 superconductors, although the nature of any electronic changes in the C-15's is unknown. It also remains to be determined if there is some more general relation between changes in band structure and high  $T_c$  superconductivity.

#### C. Suggestions for Further Work

In view of the results discussed above, there are several interesting and useful directions that future research might take.

First, to grow more single crystals, especially with different orientations, which would be useful for ultrasonics work. Second, to use ultrasonics and inelastic neutron scattering to investigate the lattice dynamics as a function of temperature, and more carefully test the applicability of Clapp's theory. Third, to completely determine the behavior of the band structure and fermi surface with temperature, and note the possible appearance of a charge density wave phenomena. And finally, to examine theoretically the possible relation between electronic structure changes and high  $T_c$  superconductivity.

APPENDIX I - PHONON SYMMETRIES

The symmetries of all possible vibrational modes of a solid may be deduced by the application of group theoretical methods. The general method<sup>30</sup> entails consideration of how each symmetry operation of the space group transforms each of three orthogonal displacements of each atom in the unit cell. This information for each operation can be expressed as a matrix  $R$ , such that

$$D_i = \sum_{j=1}^{3n} R_{ij} D_j$$

where  $D_j$  and  $D_i$  represent the initial and final orientations of the  $3n$  possible displacements of the  $n$  atoms/unit cell. Obviously,  $R$  is a  $3n \times 3n$  matrix where each row and column contains one element "1", and the rest are zero.

The set of matrices so obtained will form a representation of the group, and may in general be decomposed into a sum of the irreducible representations of the group. Once the irreducible representations are known, the symmetry properties of the various modes are determined. It is then only necessary to find (usually by inspection) which modes correspond to which representations.

This procedure, when used with all the symmetry elements of the space group, yields the symmetries of the Brillouin zone center modes. The remaining mode symmetries may be determined by decomposition of the full space group irreducible representations into the irreducible representations

of the subgroup corresponding to the symmetry of the propagation vector of each mode.

In this case we are concerned with the zone center modes. To simplify matters, rather than manipulating the whole matrices, the characters (traces) of the matrices may be used according to standard methods. In addition, the process can be separated into two steps: first, the construction of matrices representing only the transformations of the atomic positions and the decomposition of these into irreducible representations. And second, taking account of the mode displacements by forming the direct product of the resulting representations with the irreducible representation which describes the transformation of three orthogonal vectors, corresponding to the three possible displacements of each atom.

It may be seen that the representation matrices for the atom positions will have non-zero diagonal elements only where the symmetry operation either leaves the atomic position unchanged, or results in a position separated by a lattice translation from the original one. Thus the characters for each operation may be simply computed by counting the number of atom positions for which the above condition holds. The character will be equal to this sum. Representations may be constructed separately for the Zr's and V's because no symmetry operation interchanges Zr and V positions.

The C-15 structure has the non-symmorphic space group  $Fd\bar{3}m$ . The space group operations are therefore of the form  $\{R|t\}$  where R is a

point group operation followed by a translation  $t$ . The point group operations included here are all 48 operations of cubic symmetry  $\frac{4-2}{m\ m} (O_h)$  where the 24 of tetrahedral symmetry,  $\bar{4}3m (T_d)$ , require a zero lattice translation, and the remaining 24 are followed by a translation  $t = (1/4, 1/4, 1/4)a_0$ .

Table 2 shows the characters for each of the representations  $\Gamma_{Zr}$  and  $\Gamma_V$  arranged under the appropriate symmetry operations which are grouped by class. The notation is as follows:

- E = identity operation
- $C_2$  = twofold rotation axis on cube edge
- $C'_2$  = diagonal twofold axis
- $C_3$  = threefold axis on body diagonal of cube
- $C_4$  = fourfold axis on cube edge
- i = inversion
- $iC_2$  =  $C_2$  followed by inversion
- $iC_3$  =  $C_3$  followed by inversion
- $iC_4$  =  $C_4$  followed by inversion
- $iC'_2$  =  $C'_2$  followed by inversion

Below each operation is listed the character of the transformation matrix corresponding to that operation on the Zr or V positions. Here a primitive unit cell of two Zr and four V atoms has been used. Thus the character of  $\Gamma_V$  under the identity element is 4 because this operation leaves all four atomic positions unchanged.

Table 2

Characters for the Zr and V atom position transformation.  
The number preceding each operation indicates the number  
of those operations present

Operation	{R 0}					{R t}, t=( $\frac{1}{4}, \frac{1}{4}, \frac{1}{4}$ )a <sub>0</sub>				
	E	8C <sub>3</sub>	3C <sub>2</sub>	6iC <sub>2</sub> '	6C <sub>4</sub>	i	8iC <sub>3</sub>	3iC <sub>2</sub>	6C <sub>2</sub> '	6C <sub>4</sub>
Γ <sub>Zr</sub>	2	2	2	2	2	0	0	0	0	0
Γ <sub>V</sub>	4	1	0	2	0	4	1	0	2	0

The  $\Gamma_{\text{Zr}}$  and  $\Gamma_{\text{V}}$  are then decomposed into the irreducible representations of  $O_h$  using the standard decomposition formula and character table<sup>30</sup>.

The results for the atom positions are

$$\begin{aligned}\Gamma_{\text{Zr}} &= \Gamma_1^+ + \Gamma_2^- \\ \Gamma_{\text{V}} &= \Gamma_1^+ + \Gamma_{25}^+\end{aligned}$$

Next, taking the direct product of each with the representation  $\Gamma_{15}^-$ , which describes the transformation properties of three orthogonal vectors, and again decomposing, we have

$$\begin{aligned}\Gamma_{\text{Zr}} \times \Gamma_{15}^- &= (\Gamma_1^+ + \Gamma_2^-) \times \Gamma_{15}^- = \Gamma_{15}^- + \Gamma_{25}^+ \\ \Gamma_{\text{V}} \times \Gamma_{15}^- &= (\Gamma_1^+ + \Gamma_{25}^+) \times \Gamma_{15}^- = \Gamma_2^+ + \Gamma_{12}^- + 2\Gamma_{15}^- + \Gamma_{25}^-\end{aligned}$$

We see that altogether there are a total of 18 modes including one non-degenerate ( $\Gamma_2^+$ ), one twofold degenerate ( $\Gamma_{12}^-$ ), and five threefold degenerate modes (three  $\Gamma_{15}^-$ ,  $\Gamma_{25}^+$ , and  $\Gamma_{25}^-$ ). This is consistent with the total of six atoms per primitive unit cell.

We are concerned here with the Zr modes, so it is necessary to determine which modes correspond to the two representations  $\Gamma_{15}^-$  and  $\Gamma_{25}^+$ . We may assume that one is acoustic and the other is optic. Inspection of the character table reveals that functions which transform like  $\Gamma_{15}^-$  are odd under inversion (in this case inversion plus translation,  $t$ ). Therefore, this must be the acoustic mode. Similarly,  $\Gamma_{25}^+$  is even under inversion and so must be the optic mode. This mode consists of the two Zr

sublattices with origins at  $(0,0,0)$  and  $(1/4,1/4,1/4)$  moving in opposition to each other. Any mode consistent with the rhombohedral distortion must have the threefold symmetry of the rhombohedral  $c$  axis. The only modes which fulfill this condition are those polarized in the  $\langle 111 \rangle$  directions of the cube. Therefore, the search for the sublattice distortion centers on displacements along the body diagonal of the cube.



APPENDIX II. LATTICE TRANSFORMATION DATA ANALYSIS

In order to calculate the expected positions of reflections in the rhombohedral phase, it is necessary to calculate the shifts in position undergone by the reciprocal lattice points during the transformation. In general there will be four possible shifts corresponding to a distortion along each of the four body diagonals of the cube. All the shifts will be seen experimentally if all four domain types are present in the sample in the low temperature phase.

The calculation proceeds by taking the cubic coordinates of a given reciprocal lattice point and transforming them into hexagonal reciprocal space coordinates. The distortions may then be expressed as simple expansions and contractions of the a and c axes. This is done with all four sets of hexagonal coordinates, one for each body diagonal. Introducing factors to account for the strains will then give four expressions corresponding to the expected shifts. These are then converted back into cubic coordinates and result in the expressions for the (004) and (220) reflections given in Table 3. Here

$$\delta_a = (1 + \epsilon_a)$$

$$\delta_c = (1 + \epsilon_c)$$

where  $\epsilon_a$  and  $\epsilon_c$  are the strains along the a and c axes, and  $a^* = 2\pi/a_0$ . It is seen that the form of the new coordinates for the (004) reflection is  $(\pm x_1, \pm x_1, 4+x_2)$ , for a total of four points. Those for the (220) are  $(2+y_1, 2+y_1, \pm y_2)$ , and  $(2+y_3, 2+y_3, 0)$ , giving only three points because

Table 3

Reciprocal space positions of reflections descended from the (004) and (220) as a function of lattice strains  $\delta_a$  and  $\delta_c$

<u>Reflection</u>	<u>Compression along</u>	<u>New coordinates</u>
004	111	$\frac{4}{3} a^* [(\frac{1}{\delta_c} - \frac{1}{\delta_a}), (\frac{1}{\delta_c} - \frac{1}{\delta_a}), (\frac{2}{\delta_a} + \frac{1}{\delta_c})]$
	$\bar{1}\bar{1}1$	$\frac{4}{3} a^* [(\frac{1}{\delta_c} - \frac{1}{\delta_a}), (-\frac{1}{\delta_c} + \frac{1}{\delta_a}), (\frac{2}{\delta_a} + \frac{1}{\delta_c})]$
	$1\bar{1}\bar{1}$	$\frac{4}{3} a^* [(-\frac{1}{\delta_c} + \frac{1}{\delta_a}), (\frac{1}{\delta_c} - \frac{1}{\delta_a}), (\frac{2}{\delta_a} + \frac{1}{\delta_c})]$
	$\bar{1}1\bar{1}$	$\frac{4}{3} a^* [(-\frac{1}{\delta_c} + \frac{1}{\delta_a}), (-\frac{1}{\delta_c} + \frac{1}{\delta_a}), (\frac{2}{\delta_a} + \frac{1}{\delta_c})]$
220	111	$\frac{2}{3} a^* [(\frac{2}{\delta_c} + \frac{1}{\delta_a}), (\frac{2}{\delta_c} + \frac{1}{\delta_a}), (\frac{2}{\delta_c} - \frac{2}{\delta_a})]$
	$\bar{1}\bar{1}1$	$\frac{2}{3} a^* [(\frac{2}{\delta_c} + \frac{1}{\delta_a}), (\frac{2}{\delta_c} + \frac{1}{\delta_a}), (-\frac{2}{\delta_c} + \frac{2}{\delta_a})]$
	$1\bar{1}\bar{1}$	$a^* [\frac{2}{\delta_a}, \frac{2}{\delta_a}, 0]$
	$\bar{1}1\bar{1}$	$a^* [\frac{2}{\delta_a}, \frac{2}{\delta_a}, 0]$

the latter term represents two coincident shifts. The positions of these new points in reciprocal space are shown in Fig. 33, along with the (hkh) plane in which the neutron data was taken. It is seen that two of the reflections descended from the (004) lie in the (hkh) plane and that the other two lie above and below on a line normal to the plane. Both these last two points were well within the vertical resolution limit of the neutron diffractometer, and the full intensity from these reflections appears in the data at the point of projection on the plane. All three points descended from the (220) lie in the (hkh) plane.

The measured neutron intensity from the twinned single crystal at 79°K is given for the reflections descended from the (004) and (220) in Tables 4 and 5 respectively. The grid spacing is rather coarse, so it is necessary to estimate the actual peak positions which may lie between the indicated points.

The positions of the two satellite (004) peaks give values of  $x_1 = .050$  and  $x_2 = -.005$ . Solving for  $\delta_a$  and  $\delta_c$  yields  $\epsilon_a = .0139$  and  $\epsilon_c = -.0256$ . The positions of the peaks descended from the (220) give  $y_1 = .025$  and  $y_2 = .050$  which result in the values  $\epsilon_a = .0127$  and  $\epsilon_c = -.0244$ . Three additional peaks are indicated in the data at  $(2-y_1, 2-y_1, \pm y_2)$  and  $(2-y_3, 2-y_3, 0)$ . These are due to the twinned volume of crystal.

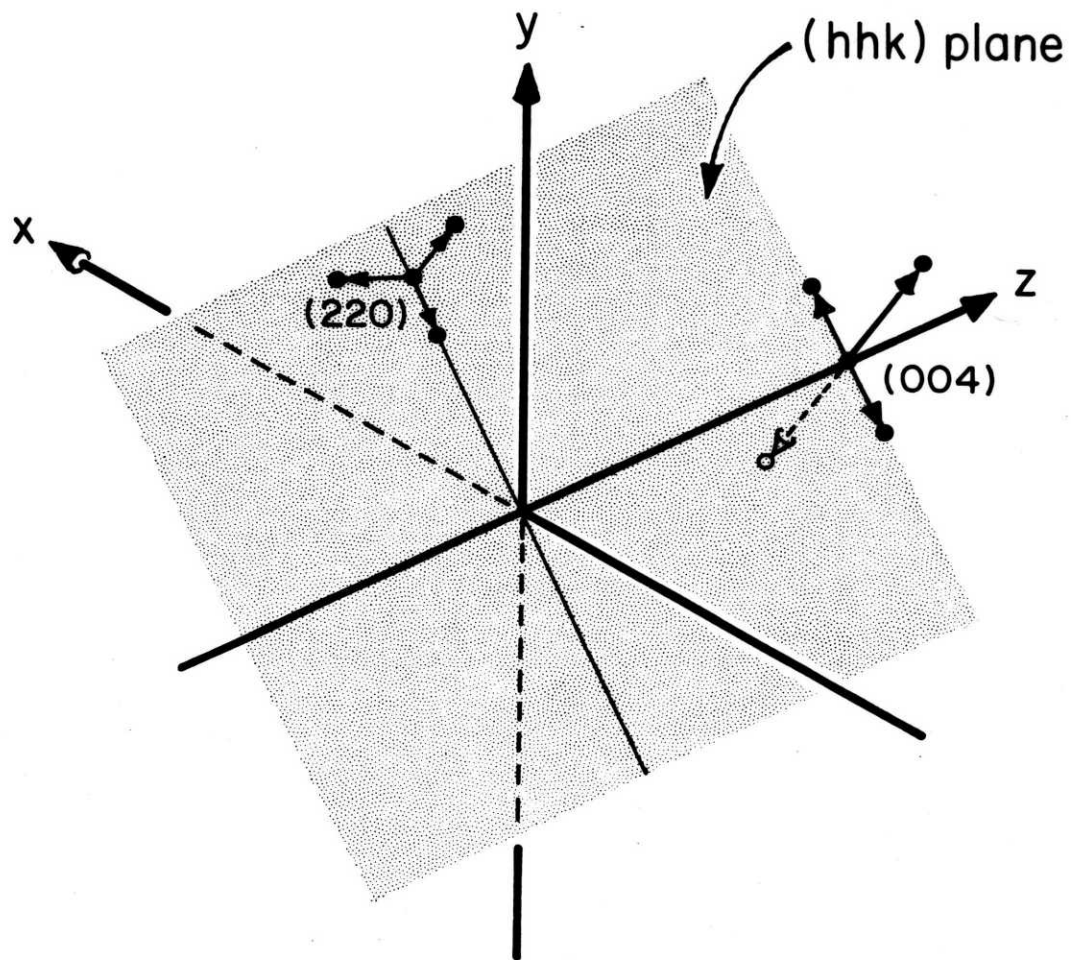


Figure 33 - Shifts in reciprocal lattice positions of the (220) and the (004) reflections occurring with a rhombohedral transformation in relation to the (h k l) reciprocal lattice plane.

Table 4

Neutron intensity at points in the (hkk) reciprocal lattice  
plane surrounding (0,0,4). Temperature = 79°K

k =	3.97	3.98	3.99	4.00	4.01	4.02	4.03
h = -0.06	74.	363.	1035.	1446.	1046.	327.	41.
-0.05	215.	1272.	2422.	2098.	903.	140.	19.
-0.04	124.	416.	619.	478.	179.	79.	36.
-0.03	71.	206.	278.	297.	154.	78.	34.
-0.02	66.	203.	317.	346.	299.	192.	85.
-0.01	155.	837.	2603.	5481.	5367.	2204.	256.
0.00	1562.	9451.	15791.	12460.	4127.	360.	88.
0.01	257.	1230.	1200.	567.	297.	93.	47.
0.02	79.	199.	280.	299.	171.	75.	34.
0.03	85.	179.	330.	390.	294.	126.	46.
0.04	115.	530.	1220.	1698.	1056.	402.	67.
0.05	254.	1322.	2439.	1954.	843.	173.	41.
0.06	102.	344.	429.	322.	147.	58.	17.

Table 5

Neutron intensity at points in the (hkk) reciprocal lattice  
plane surrounding (2,2,0). Temperature = 79°K

k=	-0.07	-0.06	-0.05	-0.04	-0.03	-0.02	-0.01	-0.00	0.01
h= 1.93	7.	3.	3.	3.	4.	2.	6.	5.	9.
1.94	2.	4.	4.	4.	4.	6.	7.	19.	11.
1.95	14.	27.	29.	14.	14.	18.	22.	80.	19.
1.96	67.	248.	290.	58.	47.	103.	474.	1537.	233.
1.97	99.	933.	2070.	526.	120.	275.	2067.	12576.	2133.
1.98	45.	443.	1659.	957.	337.	383.	2161.	10981.	2829.
1.99	32.	132.	391.	399.	280.	307.	1033.	5924.	709.
2.00	81.	153.	339.	216.	172.	208.	2183.	10256.	1595.
2.01	158.	288.	721.	419.	204.	185.	606.	2683.	588.
2.02	246.	845.	2269.	1061.	231.	182.	1690.	7941.	817.
2.03	188.	742.	1545.	571.	100.	97.	1075.	5657.	1210.
2.04	53.	131.	160.	90.	30.	29.	77.	332.	174.
2.05	17.	13.	18.	8.	12.	5.	16.	34.	19.
2.06	5.	4.	9.	5.	6.	2.	5.	11.	10.
2.07	0.	5.	3.	5.	2.	4.	3.	0.	3.

Table 5 (cont'd.)

k=	0.02	0.03	0.04	0.05	0.06	0.07
h= 1.93	2.	2.	3.	3.	5.	3.
1.94	9.	7.	6.	7.	4.	4.
1.95	20.	16.	24.	35.	14.	5.
1.96	64.	49.	128.	358.	165.	52.
1.97	243.	147.	769.	1882.	704.	99.
1.98	408.	308.	957.	1728.	587.	64.
1.99	336.	304.	338.	447.	160.	23.
2.00	187.	142.	250.	388.	150.	67.
2.01	200.	255.	512.	602.	189.	161.
2.02	114.	254.	1233.	2159.	652.	198.
2.03	105.	99.	491.	1714.	800.	197.
2.04	31.	22.	55.	173.	161.	55.
2.05	6.	13.	15.	22.	17.	14.
2.06	3.	3.	6.	6.	4.	9.
2.07	1.	6.	3.	7.	5.	0.

APPENDIX III. STRUCTURE FACTORS

The neutron diffraction structure factor for a reflection (hkl) is given by

$$F_{hkl} = \sum_n b_n e^{2\pi i(hx_n + ky_n + lz_n)}$$

where  $x_n$ ,  $y_n$ , and  $z_n$  are the coordinates of, and  $b_n$  is the neutron scattering length for, the  $n$ th atom in the unit cell. Note that  $b_n$  has a constant value for each atomic isotope and, unlike X-ray form factors, does not vary as a function of  $\sin\theta/\lambda$ .

The C-15 structure has space group Fd3m.  $ZrV_2$  has four Zr atoms at special positions (0,0,0) and face-centered equivalents, four V's at (1/4,1/4,1/4) and face-centered equivalents, and 16 V's at positions (5/8,5/8,5/8), (5/8,7/8,7/8), (7/8,5/8,7/8), and (7/8,7/8,5/8) and face-centered equivalents. Substituting these positions into the above equation and taking the product  $FF^*$  gives

$$\begin{aligned} FF^* = & 32b_v^2 [2 + \cos \frac{\pi}{2}(h+k) + \cos \frac{\pi}{2}(k+l) + \cos \frac{\pi}{2}(h+l) + \\ & \cos \frac{\pi}{2}(h-k) + \cos \frac{\pi}{2}(k-l) + \cos \frac{\pi}{2}(h-l)] + 32b_{zr}^2 [1 + \\ & \cos \frac{\pi}{2}(h+k+l)] + 64b_v b_{zr} \cos \frac{5\pi}{4}(h+k+l) [1 + \cos \frac{\pi}{2}(h+k) + \\ & \cos \frac{\pi}{2}(k+l) + \cos \frac{\pi}{2}(h+l)] \end{aligned}$$

where  $b_{zr} = 0.62 \times 10^{-12}$  cm and  $b_v = -0.051 \times 10^{-12}$  cm.

A simple rhombohedral distortion of a cubic structure of space group Fd3m gives one with space group  $R\bar{3}m$ . The sublattice distortion



theorized for  $ZrV_2$  is also consistent with this space group. The special positions in hexagonal coordinates, with the origin at the point  $(1/8, 1/8, 1/8)$  of the cubic unit cell, are for the Zr  $(0,0,z)$  and  $(0,0,-z)$ , and for the V  $(0,0,1/2)$ ,  $(1/3,1/6,2/3)$ ,  $(-1/6,1/6,2/3)$ , and  $(-1/6,-1/3,2/3)$ , and positions obtained by the addition of lattice vectors  $(1/3,2/3,2/3)$ , and  $(2/3,1/3,1/3)$ , for a total of six Zr's and twelve V's per unit cell. Thus the volume of the cubic and hexagonal cells differ by a factor of  $3/4$ .

Assuming that the Zr positions are defined by a sublattice distortion  $\epsilon_s$  relative to their non-distorted positions, then  $z = \delta_s/8$  where  $\delta_s = (1 + \epsilon_s)$ . The structure factor for the hexagonal indices  $(hk.l)$  then becomes

$$\begin{aligned}
 FF^* = & 4b_{Zr}^2 \cos^2 \frac{\pi}{4} \delta_s l [3 + 2\cos \frac{2\pi}{3}(h+2k+2l) + 2\cos \frac{2\pi}{3}(2h+k+l) + \\
 & 2\cos \frac{2\pi}{3}(h-k-l)] + \\
 & 2b_V^2 [3 + 2\cos \frac{2\pi}{3}(h+2k+l) + 2\cos \frac{2\pi}{3}(2h+k+l) + \\
 & 2\cos \frac{2\pi}{3}(h-k-l)] [2 + \cos \pi(h+k) + \cos \pi h + \cos \pi k + \\
 & \cos \frac{\pi}{3}(h+2k-l) + \cos \frac{\pi}{3}(-h+k+l) + \cos \frac{\pi}{3}(2h+k+l)] + \\
 & 4b_{Zr} b_V \cos \frac{\pi}{4} \delta_s l [3 + 2\cos \frac{2\pi}{3}(h+2k+2l) + \\
 & 2\cos \frac{2\pi}{3}(-h+k+l) + 2\cos \frac{2\pi}{3}(h-k-l)] [\cos \pi l + \cos \frac{\pi}{3}(2h+k+4l) + \\
 & \cos \frac{\pi}{3}(h+2k-4l) + \cos \frac{\pi}{3}(-h+k+4l)]
 \end{aligned}$$

APPENDIX IV. ULTRASONIC MEASUREMENTS

Measurements of the temperature dependent ultrasound propagation behavior were carried out by Mr. Ralph Bergh<sup>26</sup> on the large twinned single crystal, a clean polycrystal, and an inclusion-filled polycrystal-line sample. The samples were prepared by grinding and polishing flat, parallel surfaces on opposite ends of the cylindrical pieces. Quartz transducers were glued to these faces on each sample to be tested, which was then mounted in the sample holder. This in turn was placed inside an evacuated copper can, which was submerged in liquid N<sub>2</sub>. The sample temperature was controlled by an electrical resistance heater, and measured with a Cu-constantan thermocouple. Measurements of propagation velocity were made by noting the transit time of 1.5μsec pulses of 10.8 MHz ultrasound excitations. Attenuation was measured by the amplitude decrease of the transmitted waves.

The resulting curves of propagation velocity vs. temperature are shown for the twinned single crystal, a clean polycrystal, and an inclusion-filled polycrystal in Figs. 34, 35, and 36 respectively. Sharp increases in velocity are evident below the transformation temperatures, T<sub>m</sub>, which are in good agreement with those of the neutron data for the single crystal and inclusion-filled samples.

The velocity of sound in a solid is related to the elastic constants by

$$C = \rho v^2$$

where C is the elastic constant in the crystallographic direction and

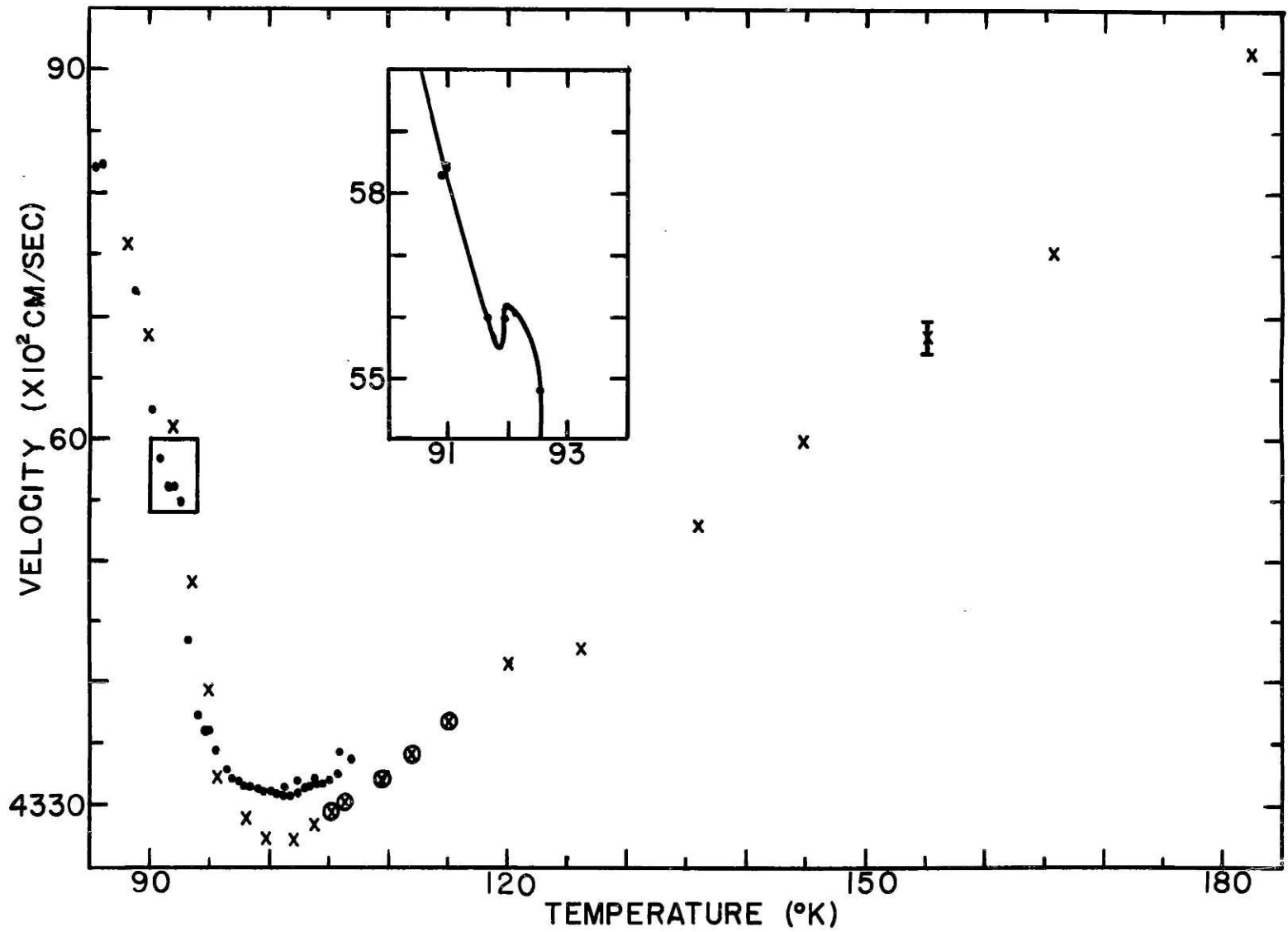


Figure 34 - Velocity of sound vs. temperature for the twinned single crystal

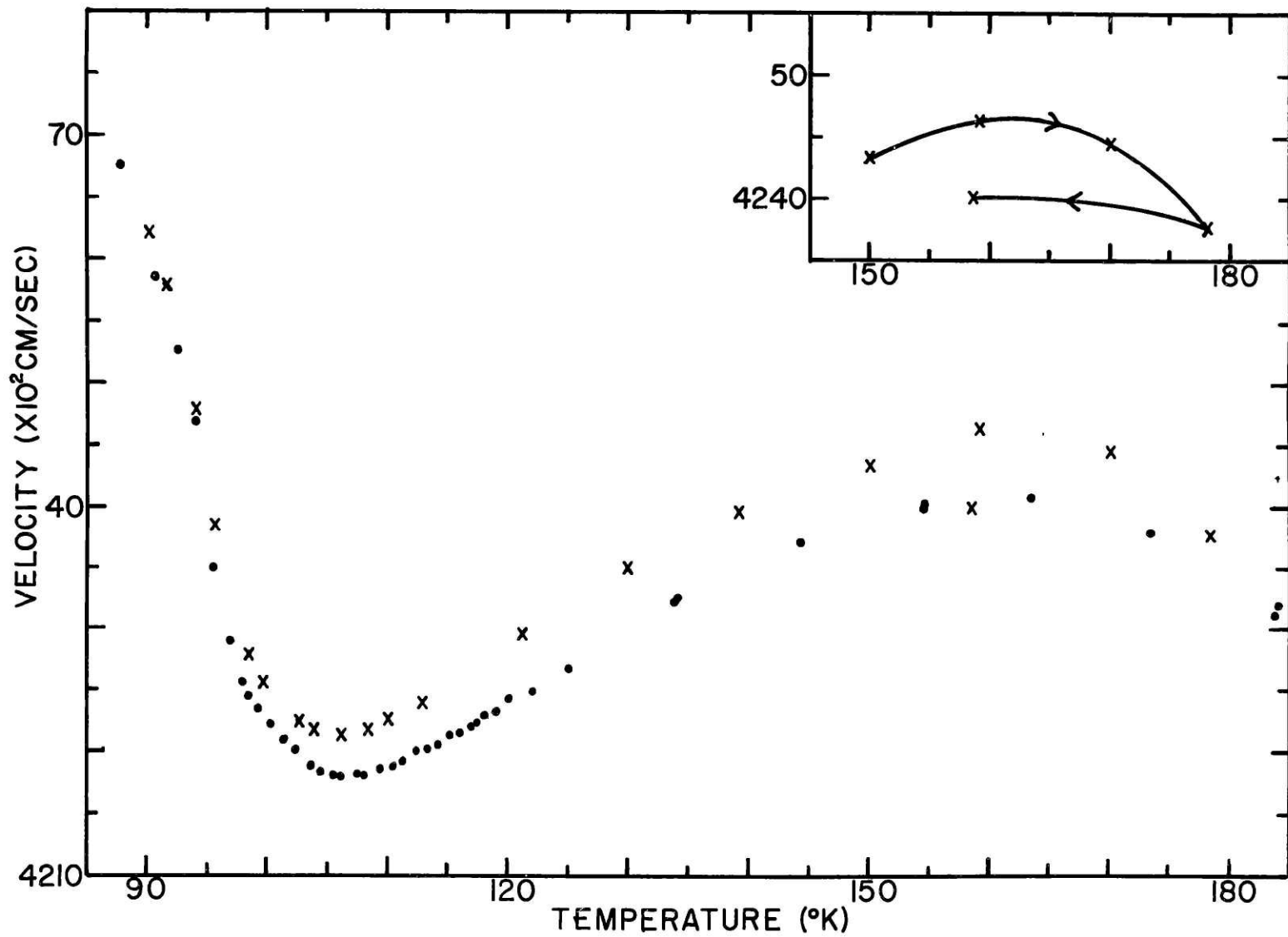


Figure 35 - Velocity of sound vs. temperature for a clean polycrystal

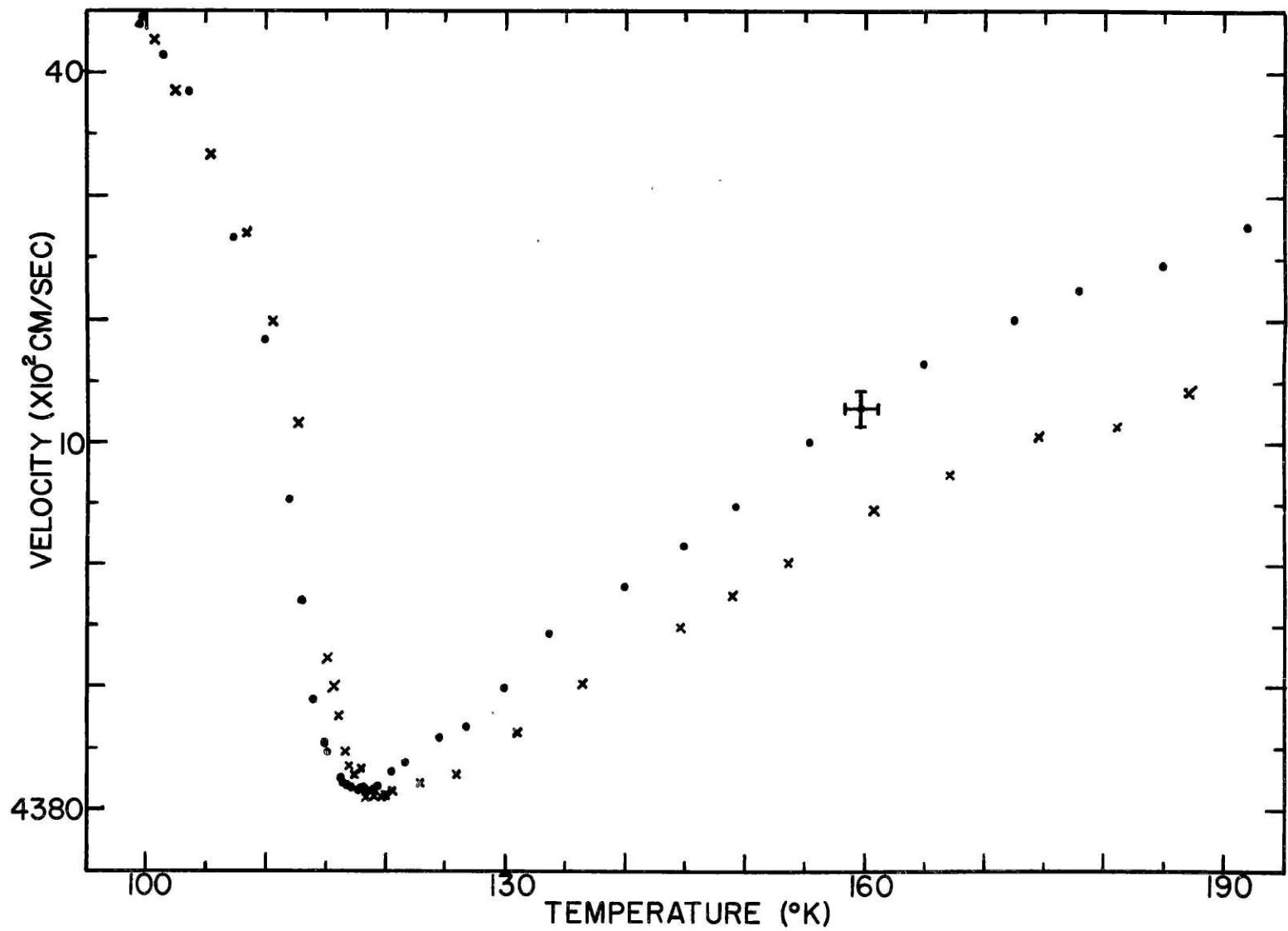


Figure 3b - Velocity of sound vs. temperature for an inclusion-filled polycrystal

polarization of the wave with velocity  $v$ , and  $\rho$  is the mass density. Thus there appears to be an increase in elastic stiffness in the low temperature phase. In addition, there is a pronounced hysteresis in the velocity between heating and cooling in the polycrystalline samples, but not in the single crystal, except in the immediate vicinity of  $T_m$ . The reproducibility of this phenomenon is shown for the clean polycrystal in the inset of Fig. 35. Also shown in Fig. 35 is an anomalous reversal in the slope of the velocity curve at around 160°K, which does not appear for the other two samples. The reasons for these last two effects are unclear.

The attenuation of the transmitted sound wave for the twinned single crystal is shown as a function of temperature in Fig. 37. It appears that any increase in attenuation is negligible near  $T_m$ . Similar results for both the polycrystals would seem to rule out the presence of either a soft acoustic phonon, or localized modes as proposed by Clapp.<sup>27, 28</sup> However, it is possible that the coupling of the ultrasound to these modes is highly direction dependent and was, by chance, not observed in the polycrystals. It is also possible that some attenuation occurred over a narrow temperature range which lay between two of the points indicated in Fig. 37. Further work would be required to conclusively resolve this question. The overall attenuation behavior would also imply the absence of high dislocation densities in the two samples.<sup>29</sup>

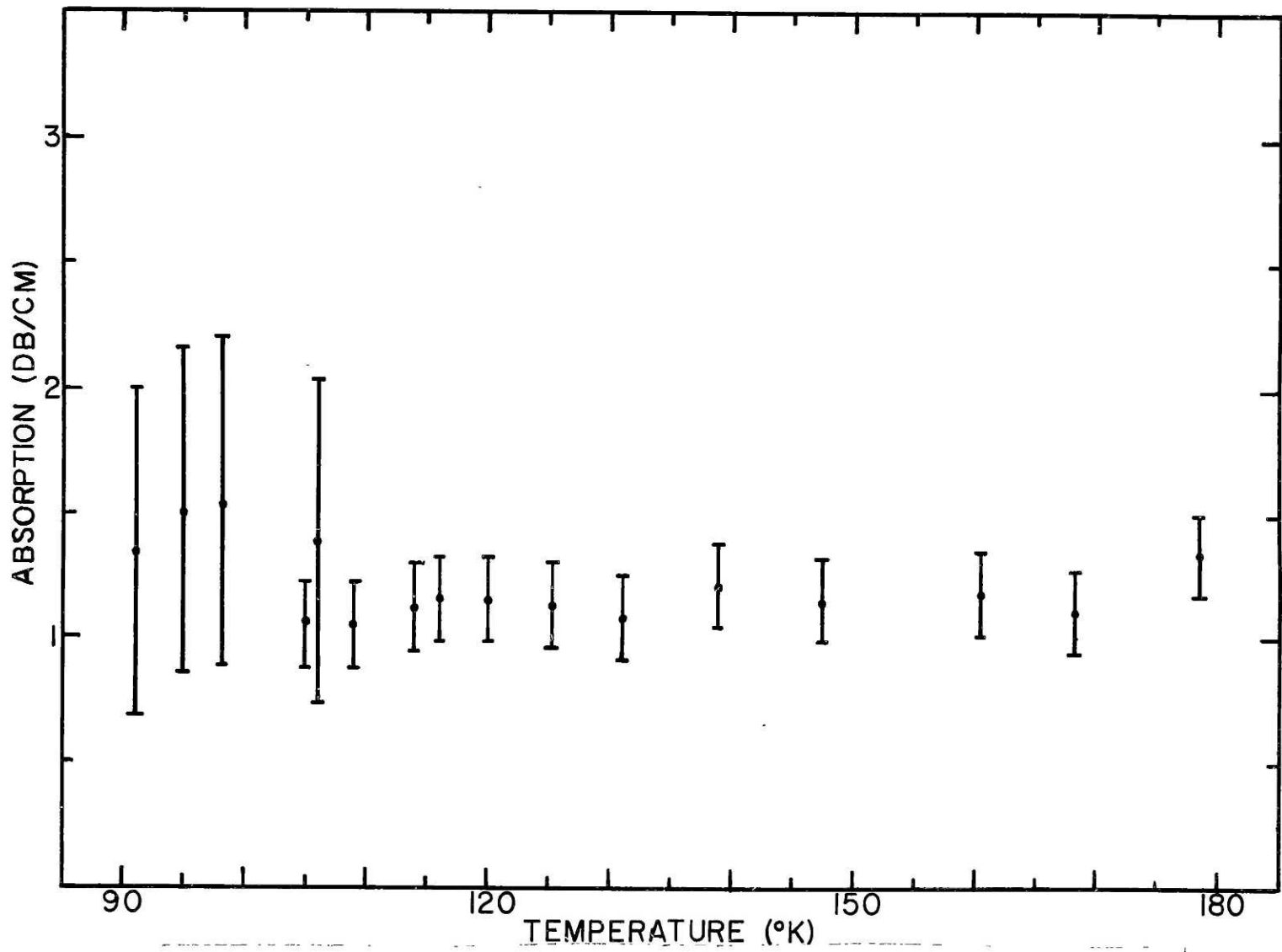


Figure 37 - Ultrasonic attenuation vs. temperature for the twinned single crystal

REFERENCES

1. B. W. Batterman and C. S. Barrett, Phys. Rev. Lett. 13, 390 (1964).
2. R. Mailfert and B. W. Batterman, Phys. Lett. 24A, 315 (1967).
3. J. Labbé and J. Friedel, J. Phys. (Paris) 27, 153 (1966); 27, 303 (1966); 27, 708 (1966); see also R. W. Cohen, et al., Phys. Rev. Lett. 19, 840 (1967) and E. Pytte, *ibid.*, 25, 1176 (1970).
4. B. T. Matthias, V. B. Compton, and E. Corenzwit, J. Phys. Chem. Sol. 19, 130 (1961).
5. V. Sadogapan, E. Pollard, and H. C. Gatos, Sol. State Comm. 3, 97 (1965).
6. K. Inoue, K. Tachikawa, and Y. Iwasa, Appl. Phys. Lett. 18, 235 (1971).
7. A. C. Lawson, Phys. Lett. 36A, 8 (1971).
8. O. Rapp and L. J. Vieland, Phys. Lett. 36A, 369 (1971).
9. J. E. Doherty and D. F. Gibbons, Phys. Stat. Sol. (b) 44, K5 (1971).
10. W. R. Dobbins, S.B. Thesis, M.I.T., June 1974.
11. T. Takashima and H. Hayashi, Phys. Lett. 47A, 209 (1974).
12. D. E. Moncton, Sol. State. Comm. 13, 1779 (1973).
13. L. D. Landau and E. M. Lifshitz, Statistical Physics, Addison-Wesley, Reading, Mass. (1956).
14. See for example: G. B. Olson and M. Cohen, Met. Trans. A, 6A, 791 (1975); 7A, 1879 (1976).
15. J. F. Scott, Rev. Mod. Phys. 46, 83 (1974).
16. W. G. Pfann, J. Metals, 7, 961 (1955).
17. G. A. Wolff and A.I. Mlavsky, Colloques Internationaux du CNRS, No. 152 (1965).



18. A. I. Mlavsky and M. Weinstein, J. Apply. Phys. 34, 2885 (1963);  
35, 1892 (1964).
19. L. B. Griffiths and A.I. Mlavsky, J. Electrochem. Soc., 111, 805 (1964).
20. See for example: B.D. Cullity, Elements of X-ray Diffraction,  
Addison-Wesley, Reading, Mass. (1956), Chp. 11.
21. Dr. J. Vander Sande, private communication.
22. K. Inoue and R. Tachikawa, Japan, J. Appl. Phys. 12, 161 (1973).
23. T. F. Smith, R.N. Shelton, and A.C. Lawson, J. Phys. F, 3, 2157 (1973).
24. K. Inoue, K. Tachikawa, and Y. Iwasa, Appl. Phys. Lett. 18, 235 (1971).
25. W. D. Gregory, et al., AEC Report ORO-3665-12.
26. R. Bergh, S.B. Thesis, M.I.T., September, 1977.
27. P.C. Clapp, Phys. Stat. Sol. (b) 57, 561 (1973).
28. P.C. Clapp (to be published), J. Physique (1977).
29. R. Truell, C. Elbaum, and B. Chick, Ultrasonic Methods in Solid State  
Physics, Academic Press, New York (1969).
30. See for example: Tinkham, Group Theory and Quantum Mechanics,  
McGraw-Hill, New York (1964).
31. M. Hansen, Constitution of Binary Alloys, McGraw-Hill, New York  
(1958), p. 1253.

BIOGRAPHICAL NOTE

The author was born August 13, 1950 in Cleveland, Ohio, and attended public schools in Mount Vernon and New Rochelle, N.Y. He entered M.I.T. in September, 1968 and received the degree of Bachelor of Science in Metallurgy and Materials Science in February, 1972. He entered graduate school in September 1972, serving as a Teaching Assistant for two years, and then a Research Assistant. His immediate plans include postdoctoral work in the Department of Organic Chemistry at the University of Geneva.